細胞内微視領域での時間分解蛍光分光を目指した低温顕微鏡システムの展開

博　士　論　文

Development of Multifunctional Cryo-Optical Microscope System for Time-Wavelength 2D Image within Intracellular Subdomain

(細胞内微視領域での時間分解蛍光分光を目指した低温顕微鏡システムの展開)

藤　田　祐　輝

２０２１年

Abstract

Oxygenic photosynthesis is performed by the two photoactive units, photosystem I (PSI) and photosystem II (PSII), that utilize light energy to generate the electron flow from water to NADPH. Photosynthetic organisms have developed mechanisms called state transitions to regulate the excitation balance between the two units, since the balance is constantly disturbed by fluctuation in light quality. The traditional state transitions model assumes shuttling of a light-harvesting complex called LHCII between the two PSs. In addition, some previous studies have suggested the appearance of the isolated LHCII bound to neither PSs, in parallel with the shuttling of LHCII. This isolated or free LHCII down-regulates the energy flow to PSs. These functions have a significant effect on the efficiency of photosynthesis, which is a potential key to improve a crop production. However, there has been no direct observation of the intracellular rearrangements and the excitation energy transfer kinetics of LHCII upon state transitions. Recently, the establishment of cryo-electron microscopy and cryo-electron tomography methods has facilitated our understandings of the molecular structures and intracellular distributions of the photosynthetic proteins. On the other hand, changes in protein-protein interactions in response to the external stimulation, such as the state transitions, are reproduced only under the physiological environment within the chloroplast. My doctoral research has focused on the development of novel cryogenic optical microscope systems that is the first in the world to provide fluorescence spectrum and fluorescence lifetime simultaneously at every pixel position on an image of a cryo-treated specimen. This was achieved by combining the cryo-microscope system with either the time-correlated single photon counting setup or the streak camera. Here, I demonstrate that this system is an innovative imaging method to realize more comprehensive investigation on the dynamic changes in excitation energy transfer kinetics based on the rearrangement of protein supercomplexes in living cells. I have succeeded for the first time in the world in spatially resolving the intracellular PSII-rich and PSI-rich regions by operating the developed system for imaging of a unicellular green alga *Chlamydomonas reinhardtii* at 80 K. A time-resolved fluorescence spectrum measurement within the identified local regions have revealed the change in the excitation energy transfer kinetics from LHCII to PSs upon the state transitions. Moreover, the simultaneous acquisitions of the spectrum and fluorescence decay kinetics enabled to specify the presence of the highly quenched and red-shifted (to 690-695 nm) LHCII which colocalized in

the PSI-rich region upon the state2 induction. The observed red shift of the peak wavelength suggested the formation of LHCII aggregates. In addition, I have challenged to develop a STED microscope system that operates at low temperatures to more clearly resolve segregations of intracellular PSII-rich and PSI-rich regions. Although I have confirmed the advantages of the low-temperature environment for efficient stimulated emission, I could not succeed in improving the spatial resolution probably due to the problem in the quality of the donut-shaped STED beam at the focal plane. In parallel with the development of the cryogenic optical microscope system, I also began collaborative research on the development of a novel model sample with thylakoid membrane arranged on the substrate for easy microscopic observation. I devoted my doctoral research to establish a novel in-vivo platform to understand the photophysical and biochemical processes in photosynthesis and to inspire the design of genetically modified crops for improvement of crop production.

Table of Content

Chapter III Experiment with the FLIM System

Chapter IV Streak Camera within Microscopic Area

Chapter V Development Cryogenic STED Microscope System

Chapter I General Introduction

1-1 Photosynthesis

Most life on the earth depends on the oxygenic photosynthesis carried out by plants, algae, and cyanobacteria. These organisms capture sunlight energy to convert water and carbon dioxide into organic matter and oxygen molecules as shown in the following chemical equation.

$$6CO_2 + 6H_2O \rightarrow C_6H_{12}O_6 + 6O_2. \qquad \text{(Equation } 1-1\text{)}$$

In eucaryotic photosynthetic organisms, oxygenic photosynthesis is conducted in an organelle called chloroplast. the process of the complicated oxygenic photosynthesis can be broadly divided into two steps, thylakoid reaction and carbon-fixation reaction (Fig. 1-1). This thesis focuses only on the thylakoid reaction. The thylakoid reaction is performed in the thylakoid membrane, which is a lipid bilayer filling the interior of a chloroplast and forms a special 3-D structure [1, 2, 3]. In this reaction, sunlight energy is consumed through a series of processes such as light harvesting, charge separation, electron transport, proton pumping and proton transfer to synthesize the final products, adenosine triphosphate (ATP) and nicotinamide adenine dinucleotide phosphate (NADPH). Carbon fixation reaction is performed in stroma which is an aqueous solution space between the thylakoid membrane and the chloroplast inner envelope. ATP and NADPH are essential for driving the Calvin Benson cycle which is the core reaction scheme of the carbon fixation process. NADPH and ATP are consumed in the Calvin-Benson cycle and eventually converted to $NADP^+$ and adenosine diphosphate (ADP), respectively. The generated carbohydrates form the basis of most energy resource for life on the earth. $NADP^+$ and ADP are reused in the thylakoid reaction for reproduction of ATP and NADPH.

1-2 Thylakoid Reaction

Figure 1-2 (a) shows an illustration of internal structure of chloroplast. The thylakoid membrane is divided into two completely different regions, stacked membrane region called grana and unstacked membrane region called stroma lamella. A chloroplast contains two types of photoactive pigment proteins, photosystem I (PSI) and photosystem II (PSII). These proteins are embedded in the thylakoid membrane, and it is known that PSII is abundant in the grana region, while PSI is abundant in the stroma lamella region. PSII core part is mainly composed of three sub-domains, reaction center (RC: mainly composed of a heterodimer of D1 and D2 subunits),

and the core antenna subunits C43 and CP47, whereas PSI is composed of several subunits surrounding the two main core proteins, PsaA and PsaB (Fig. 1-7).

Chlorophylls (Chls), which mainly play the roles of absorption of photon energy, transmission of excitation energy, and electron transfer are contained in the subunits of PSII and PSI (PSs) (Fig 1-3, Fig. 1-4). In general, PSs core complexes have about 35 Chl-*a* and about 100 Chl-*a*, respectively. The light energy absorbed by an antenna Chl is transferred to the RC where the charge-separation reaction occurs. The primary donor (PD) is located at around the center of PSs. PDs of PSI and PSII are often called P680 and P700, respectively, according to their peak wavelengths observed by the transient absorption measurements. Although PD of both PSI and PSII used to be assigned to the central dimeric Chls called special pair according to the structural similarity to the bacterial RC, later studies [106] have revealed that PD of PSII is more likely to be the neighboring Chl called accessary Chl. Interactions between Chls and the proteins affect the diversity of their excitation energy. There are mainly three interactions: 1) Direct action of the charged amino acid residues, 2) the side chains connected to the chlorin ring (Fig. 1-4) with a single bond are rotated by peripheral amino acids residues and 3) The distortion of the chlorin ring by the coordination of amino acid to the central magnesium ion.

The excitation energy of each Chl tends to be higher at the periphery of the proteins, forming a funnel-like excitation energy landscape to promote efficient energy transfer to PD. Fast energy transfers to the PD ensure the higher charge separation efficiency because this light-harvesting process competes with the spontaneous decay of the pigment excited state due to the fluorescence emission and heat dissipation. The excitation energy on an antenna Chl rapidly migrates among many antenna pigments and finally arrives (is trapped) at the PD where the energy is consumed by the charge-separation reaction. The energy transfer to PD and the subsequent trapping takes within 20 to 300 ps, and the maximal quantum yield of the charge separation is close to 1.0 for PSI and 0.9 for PSII [4, 5].

Schematic illustrations of the linear electron flow and correlation of a redox potential with each step of the flow (Z scheme) are shown in Fig. 1-2 (b) and Fig. 1-5, respectively. Charge separation at the PD generates the cationic and anionic species with higher and lower redox potentials, respectively. In PSII, the charge separation forms the oxidation power to extract electrons from water molecules through an oxygen-evolving complex (OEC) at lumen side. The primary electron acceptor from PD in PSII (P680) is pheophytin (Pheo). Pheo has the same

structure as Chl except for the central metal ion replaced with hydrogen atoms. Two-plastoquinone molecules called Quinone A and B (Q_A and Q_B, respectively) are the subsequent electron acceptors in the electron-flow chain. Doubly reduced Q_B accepts two protons from the stroma region to yield a hydroquinone (Q_BH_2), which dissociates from PSII, diffuses within the thylakoid membrane, and binds to the lumen side of cytochrome b_6f complex, a large multi-subunit protein, to feed electrons to it. This process induces the transmembrane proton transport from the stromal to lumenal side. The cytochrome b_6f then transfers electrons to plastocyanin which reduces oxidized PD in PSI (P700). The anion species generated from the charge separation of P700 feeds electron to three iron-sulfur clusters (F_A, F_B, and F_x) via two electron acceptor molecules (A_0, A_1). Electron is transferred from the ion-sulfur clusters to ferredoxin, then a membrane-associated flavoprotein, ferredoxin-NADP reductase, which reduces $NADP^+$ to NADPH. In short, the two-step charge separations in PSs and a linear electron transfer from PSII and PSI lead to pumping of electrons in water molecule, which is an abundant resource on the earth, to the species NADPH with the higher redox potential.

The ATP synthesis is driven by the chemiosmotic mechanism, which utilizes the difference in the chemical potential of protons between inside (lumen) and outside (stroma) the thylakoid membrane. The proton pumping is mainly provoked by the following two factors. 1) The oxidation reactions of water molecules at OEC of PSII release protons to the lumen side. 2) Electron transfer via quinone pool and cytochrome b_6f involves transmembrane proton transport from the stromal to lumenal sides. Higher concentration of proton in lumenal side facilitates the proton flow back to the stromal side through the ATP synthase, which is an enzyme catalyzing the ATP synthesis reaction by using the proton motive force.

1-3 Light Harvesting Complex (LHC)

The absorption of a photon by a pigment is the first step in photosynthesis. A light harvesting complex (LHC) is a photoactive pigment-apoprotein complex that absorbs the light and transfers its excitation energy to RC to drive the photochemical reaction. While the designs of the organizations of RC are highly conserved over the all species, those of LHCs have a large variability, reflecting the evolutional acclimation to the various living environment. For example, organisms living in water or in a low-light environment have developed a large LHC antenna system, whereas plants seem to have a smaller but more modular system to quickly respond to

the typical changes in light intensity illuminated on land. In the green lineage (green alga and plant), light harvesting complexes II (LHCII) and I (LHCI) are representative LHCs that surround the outside of the PSs and play as antenna to feed the excitation energy [6, 7, 8]. Here, I focus on the LHCs contained in the unicellular green alga *Chlamydomonas reinhardtii*, which is a target organism in this study. *Chlamydomonas* has relatively a larger amount of LHCs associated with each PS in comparison with plants.

LHCII apoproteins encoded by *Lhcb* genes mostly attached to PSII. In *Chlamydomonas*, there are eleven *Lhcb* genes encoding apoproteins of nine LhcbM isoforms which presumably form the trimeric LHCII and two monomeric Lhcb proteins known as CP26 and CP29 [11, 12]. At present, three types of LHCII-trimers, strongly bound LHCII trimers (S-LHCII), moderately bound LHCII trimers (M-LHCII), and naked LHCII trimers (N-LHCII), have been found that are distinguished by their different affinities for PSII [14] (Fig. 1-7 (a)). On the other hand, PSI keeps binding ten LHCI monomers (Lhca1a, Lhca1b, Lhca2-Lhca9) [9, 10, 13] (Fig. 1-7 (b)).

LHC not only feeds energy to the PSs, but also plays several acclimation roles in response to changes in the external light environment. The intensity of sunlight irradiating chloroplasts fluctuates rapidly due to shadows of clouds, other leaves, and so on. In high light conditions, excessive light absorption promotes the generation of triplet Chls, leading to produce singlet oxygen and other reactive oxygen species (ROS), which damage thylakoid components. To avoid this photo-oxidative damage, LHC has a function called non-photochemical quenching (NPQ) that dissipates most of the absorbed energy as heat [97]. In low light conditions, the excitation balance between PSs is sometimes disturbed depending on the habitat of the organism. In particular, green algae, such as *Chlamydomonas*, inhabit underwater where the wavelength of the arriving light varies with the depth, and the fluctuations in the irradiation-light spectrum are thought to cause an unbalanced excitation influx for PSs. The tate transitions have been regarded as responsible functions of LHC for preserving the excitation balance between PSs as descried in detail in the next section.

1-4 History of Study on State Transitions

Since PSs include Chls with the diverse excitation energy levels, they exhibit distinct absorption characteristics [18] (Fig 1-6). In a visible light region, PSI has a broad absorption peak in the far-red region (700 - 710 nm), whereas PSII favors blue light region (460 - 530 nm). An imbalance of energy distribution between PSs tends to occur in natural environments, where light

quality and quantity fluctuate constantly. To ensure optimal photosynthetic efficiency, the state transitions serve as light acclimation mechanism of chloroplast to balance energy distribution between PSs [19, 20].

The state transitions include two distinct states. When an illumination light prefers to excite PSI over PSII, LHCII feed their absorbed energy to PSII (state1). On the contrary, predominant excitation of PSII over PSI induces an increase in the energy supply to PSI. The transition from state1 to state2 has been considered to proceed according to the following steps:

1) Predominant excitation of PSII over PSI leads to an increased redox of the quinone pool.
2) The kinases called stt7 (*Chlamydomonas*) and stn7 (plants) are activated via the binding of the reduced quinone to cytochrome b_6f as the triggering signal [21, 22].
3) The activation of stt7/stn7 induces the phosphorylation of the threonine residues of LHCII, causing its disassociation from PSII [23].
4) Phosphorylated LHCII preferentially attaches to PSI.

In short, the shuttle of LHCII depending on its phosphorylation is presumably the main mechanism of the state transitions.

The phenomenon of the state transitions was discovered half a century ago [25, 26]. Down to the present day, wide variety of techniques have been used to quantify the ratio of LHCII that actually moves upon the state transitions in *Chlamydomonas* which is a model organism for studying the state transitions. Just before entering the 21st century, absorption spectroscopy and photoacoustic technique were used to determine an increase in the antenna size for PSI of 50% in state2 [27]. In the last decades, genetic and biochemical techniques have revealed that a part of LHCII moves to PSI upon state1 to state2 transition [28, 29]. These studies also suggested the existence of isolated LHCII (free-LHCII) which down-regulates the energy flow to PSII. A combination of circular dichroism and absorption spectroscopy was used to quantify the ca. 20% enhancement of PSI antenna size during the state transitions, whereas the decrease in PSII antenna size was estimated at ca. 70%, supporting existence of such free-LHCII [30]. Studies using picosecond time-resolved fluorescence spectroscopy at liquid-nitrogen temperature suggested that the free-LHCII turns into its quenching form to prevent a generation of ROS [31, 32]. This suggestion is consistent with an observation by fluorescence lifetime imaging (FLIM) [33, 34]. On the other hand, Nawrocki et al. revisited the issue by using a plastocyanin-lacking mutant which allows the measurement of the PSI antenna size [38]. They indicated that the reduced

antenna size in PSII was nearly compensated by the increase in PSI, suggesting that a large fraction of LHCII actually shuttles between the two PSs and few LHCII remains isolated from both PSs. Thus, this study explicitly excluded the accumulation of free LHCII.

Recently, our understandings of overall architectures of the LHCII-PSII super complex and LHCII-LHCI-PSI super complex in both state1 and state2 have been facilitated with the near-atomic spatial resolution. These advancement has been accomplished by the establishment of the single-particle cryogenic electron microscope (cryo-EM) method and advances in the purification techniques of intact LHCII-bound super complexes based on adoptions of various mild detergents such as nonionic amphipol [14, 15, 39, 40]. The highly resolved architecture allows us to count the number of LHCII trimers included in each super complex. In addition, the structural studies clarified the locations and orientations of the permanent dipole moments of Chls bound to the super complexes, enabling us to estimate energy transfer pathways from LHCII to PSs cores [41, 42].

1-5 Importance and Purposes of My Research

The higher-resolution structures of the super complexes have served us reliable knowledges related to the state transitions, such as changes in antenna size and its energy transfer pathways to the core complexes. Nonetheless, there is still a gap in the definite understanding of LHCII migration and functional change upon the state transitions, as summarized below.

1) Uncertainty of changes in net LHCII antenna size and its energy transfer in vivo situation probably occurring in a peripheral pool of LHCII which may be lost during purification.
2) No evident for localization and function of free-LHCII.

LHCII binds to super complexes with a relatively week interaction so that it can be flexibly detachable in response to illumination conditions. This may result in loss of the antenna protein during the purification process. Some in vivo studies insisted that the number of LHCII trimers can be far larger than in the purified super complexes [43].

Recently, advance in cryogenic electron tomography (cryo-ET) with sub-nm spatial resolution enabled to observe the distribution of the photosynthetic proteins embedded in the thylakoid membrane in *Chlamydomonas* [44]. Although the method succeeded in visualizing the exact intracellular distributions of the two PSs (PSII is abundant in the grana and PSI is abundant in stroma lamella as mentioned in session 1-2) by utilizing the difference in the length of

protrusions from the membrane, little is known about location of free-LHCII. This is because they are entirely embedded within the highly electron-dense thylakoid membrane and have no significantly protruded domain from the membrane. Even though, affinity mapping atomic force microscopy method have succeeded in visualizing specifically cytochrome b_6f within the membrane [45]. This technique adopted a probe with plastocyanin having a specific affinity to the cytochrome b_6f, which is not applicated to LHCII. In addition, cryo-ET and atomic force microscope (AFM) techniques with the nanometer resolutions have no accessibility to information on the protein function such as energy transfer.

It is necessary to establish a new experimental method that enables in vivo observations of LHCII localizations with the ability of its functional analysis, overcoming above problems. Optical microscope is a strong tool to visualize the sub-micrometer scale structure and the distribution of a protein of interest in an intact cell. This method, if it is combined with advanced spectroscopic techniques, also allows us to know a kinetics of excitation energy transfer within protein complexes of interest with the benefit of using light as an exploration medium [34, 35, 36, 37].

One of bottlenecks in resolving the intracellular distributions of photosynthetic components using optical microscope is the difficulty in the spectroscopic decompositions into the specific components due to severe spectral overlaps among the components at room temperature. A very low fluorescence quantum yield of PSI at room temperature [46] is also problematic for fluorescence microscope observations. To eliminate these problems, fluorescence spectroscopy on intact photosynthetic systems has often been performed at low temperatures where PSII and PSI give well-separated emission bands at around 685 nm and 720 nm, respectively [31, 32, 47, 48, 49]. Moreover, the slowdown of the energy transfer at low temperatures enhances the chance to observe the emission component from LHCII which usually appears at the blue edge of the Chls emission band (Fig. 1-8) Recently, an optical microscope system operative at cryogenic temperatures have been developed in our laboratory. The developed system was designed to set a microscope objective within heat-insulating vacuum chamber. This design realized a drastic reduction of the distance between the sample and the objective lens, enabling the use of a high-numerical aperture (NA) lens. The spatial resolution of our system is about 400 nm, which was shown to be sufficient to distinguish grana in the chloroplast [50 - 56] (Fig. 1-2). Using this system, we succeeded in visualizing the intracellular heterogeneity of the

two PSs of intact *Chlamydomonas* cells [50].

Another bottleneck is the difficulty in determining the fluorescence quantum yield (FQY) which is affected by changes in the state of chromoproteins. In general, the fluorescence intensity of a fluorescent species is proportional to the product of its concentration and FQY. The inhomogeneity of intracellular FQY prevents to map the local concentrations chromoproteins accurately based on the fluorescence intensity. In particular, it is suggested that the FQY of LHCII bound to two PSs is significantly different from that of free-LHCII [57 - 59]. Therefore, in order to determine both the distribution and state of the protein of interest, it is necessary to obtain not only the fluorescence spectrum but also the fluorescence decay time profile.

In my doctoral research, I have improved the cryogenic microscope system in order to acquire both fluorescence spectra and decays emitted from cryogenic cells simultaneously. Fluorescence decay measurement allows the estimation of the FQY independent of the fluorescence intensity. Using this system, it became possible to simultaneously examine the state of LHCII (LHCII bound to two PSs or free-LHCII) in addition to the intracellular distribution of each of the pigment proteins LHCII, PSII, and PSI. The main purpose of my research is to verify, in vivo situation, the changes in net LHCII antenna size and its energy transfer, and the location and function of free-LHCII upon state transitions.

1-6 Introduction of STED Microscope

In parallel with the development of the above system, we also attempted to improve the spatial resolution of the optical microscope to achieve a clearer identification of the heterogeneous distribution of the photosynthetic proteins. The resolution needed to image subcellular architecture and dynamics in an optical microscopy is hindered by the diffraction limit and a structure smaller than 200 nm are lost in a blur. Recently, appearances of super resolution fluorescence microscopy techniques have broken the diffraction limits and allowed us to look at cells with much better clarity [72]. Most famous super resolution fluorescence microscopy techniques are listed below.

1) Stimulated emission depletion microscopy (STED) [63 - 66].
2) Structured illumination microscopy (SIM) [73, 74].
3) Stochastic optical reconstruction microscopy (STORM) [77].
4) Photoactivated localization microscopy (PALM) [75, 76].

STORM and PALM techniques require dye concentrations low enough to distinguish single molecules, making them unsuitable for the measurement of chlorophyll autofluorescence in photosynthetic systems. Although, SIM can acquire consecutive images of changes in living cells at a high speed of less than 1 second/image, it is difficult to be combined with spectroscopic measurements and time-resolved measurements. Since STED only involves the process of laser scanning of a sample, we applied this technique for our microscope.

1-7 Optical Microscope Measurements at Cryogenic Temperature

General advantages of performing imaging of living samples with an optical microscope at low temperatures are summarized below.

1) Increase in the number of fluorescence photons.
2) Immobilizations of macromolecular structures in living cells.

The total amount of fluorescence photons is limited by the probability of a chemical reaction of the excited fluorescent molecule with diffusing oxidizing agents, which finally leads to photobleaching and phototoxicity. This chemical reaction rate is greatly reduced at low temperatures according to the Arrhenius law. In addition, working with cells at low temperature has the inherent advantage of the fixation that effectively stops enzymatic and chemical reactions and structural changes in cell organelles. This allows us to closely observe the structure-function relationship of the target matter. The previous study with cryo-EM has demonstrated that the rapid freezing is superior to the chemical fixation in terms of preserving ultrastructure and minimizing artefacts [84]. These advantages are very compatible with super resolution fluorescence microscopy techniques as described below.

In a localization microscopy such as STORM and PALM methods, one stochastically picks up individual fluorescence signals in a sample and determine the center of the point spread function (PSF) from each emitter. The precision of this approach is dictated by the S/N ratio, which is in turn improved by working under a low temperature, as described above. The low temperature fixation also increases the accuracy of locating target emitters. Weisenburger et al. succussed in determining the distance between two fluorophores attached within a protein with sub-nm accuracy utilizing the naturally occurring stochastic photoblinking, which takes place on the timescale of seconds and minutes at 4.3 K [76]. They used a vacuum-compatible objective lens mounted inside of vacuum chamber, which is similar design to our microscope system. Wang

et al. achieved ca. 10-nm spatial resolution by performing STORM at liquid nitrogen temperature [85]. They applied super-hemispherical solid immersion lenses which has a shape of a truncated sphere made of zirconia with a high refractive index.

In addition, as described in Chapter V, the low temperature operation suppresses the anti-stokes excitation by the STED beam, realizing the efficient STED even with relatively weak excitation beam. The beneficial performances of the STED microscopy at cryogenic temperature have been demonstrated in the recently reported study [83]. In this system, a sample is pasted onto a thermally conductive diamond heat exchanger and cooled by a burst of pressurized liquid nitrogen, resulting in the achievement of a rapid cooling rate (200,000 $K^{-1}s$). This realized the cell fixation without mechanical disruption of cell structure by ice crystals or denaturation of lipid membranes and proteins by ice crystals.

1-8 Impact of the Present Study on Society and Industry

Here, I describe the significance of our research in terms of contributions to society and industry. It is concerned that the crop production will not meet the human demand by 2050 due to population growth, increased consumption of meat [88, 89], climate change [90, 91], and mandates for biofuels (food crisis [86, 87]). Therefore, it is necessary to fundamentally revise the current system of the crop production. In recent years, increasing the efficiency of photosynthesis has been the focus of attention as a new revolution to improve crop production [92]. I introduce several examples below.

As I shown in Fig. 1-6 (a), the two PSs have similar absorption wavelength bands and work to compete with each other for photons. There is one option that Chl-*b* in PSI used by oxygenic organism is replaced with bacteriochlorophyll (BChl)-*b* included in purple photosynthetic bacteria [93]. Although this idea has not been demonstrated experimentally, it is expected that light spectrum utilized for photosynthesis extends up to 1075 nm.

In addition, there is an attempt to increase the efficiency of energy transfer from LHC to PSs. The intensity of sunlight irradiating chloroplasts fluctuates rapidly due to shadows of clouds and other leaves. LHC has a photo dissipation function, represented by NPQ, to avoid deleterious photooxidations under excessive light conditions. The structural changes in the LHC related to NPQ are not rapid enough to catch up with the temporal changes in the solar intensity, resulting in a large amount of energy dissipation even under weak light. Although Kromdijk et al.

have succeeded in improving crop production by almost 20 % by restricting the expression of the enzymes involved in the NPQ-inducing conformational change of the LHC, the molecular mechanism of NPQ has not been completely clarified [96].

The major rate-limiting step in the carbon fixation reaction, represented by the Calvin-Benson cycle, is the reaction of ribulose 1,5-bisphosphate carboxylase/oxygenase (Rubisco) with CO_2. C4 plants (for example, tropical grasses such as sugarcane (*Saccharum officinarum*) and corn (*Zea mays*)) improve this reaction by sequestering Rubisco into compartments where CO_2 is concentrated. Efforts to incorporate this capability into rice, a C3 plant, are being undertaken through the international collaboration [94, 95].

The motivation for my research is to improve the rate of energy transfer from the LHC to PSs. In order to acclimate for the natural environment where the light intensity and wavelength change drastically, the LHC has light-responsive functions such as NPQ and state transitions, and we believe that improvement of these processes is a potential key to increase the efficiency of energy input to PSs. However, the energy transfer and heat dissipation pathways associated with these processes have not been fully elucidated at present. One of the major reasons is that we have not yet established a method for observing the conformational changes of LHC in response to the external stimulations, which can only be performed in intact chloroplasts. I have aimed to establish a new in-vivo method to explore changes in the distribution and function of LHC involved in state transitions. We believe that in future years this method will provide a complete understanding of the process of energy transfer and heat dissipation in the LHC in response to the external stimulation and provide a new platform for evaluating various genetically modified crops for improvement of crop production.

1-9 Outline of this thesis

The research contents of this thesis are summarized in the illustrations in Fig. 1-9. I upgraded our cryogenic system to verify the variation in localization and function of LHCII (Fig. 1-9 (a) - (c)). In addition, I started the collaborated research with Assoc. Prof. Morigaki group in Kobe university to realize establishment of an artificial photosynthetic membrane (Fig. 1-9 (d)).

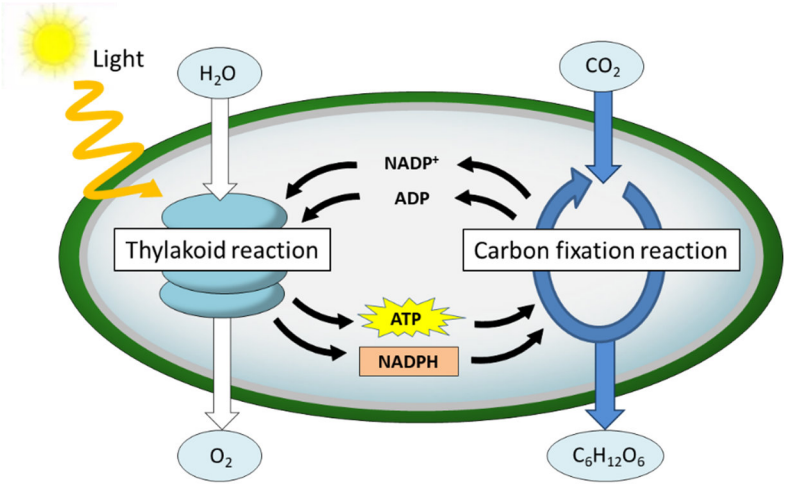

Figure 1-1 A comprehensive illustration representing the thylakoid reaction (left) and the carbon-fixation reaction (right) in the oxygenic photosynthesis.

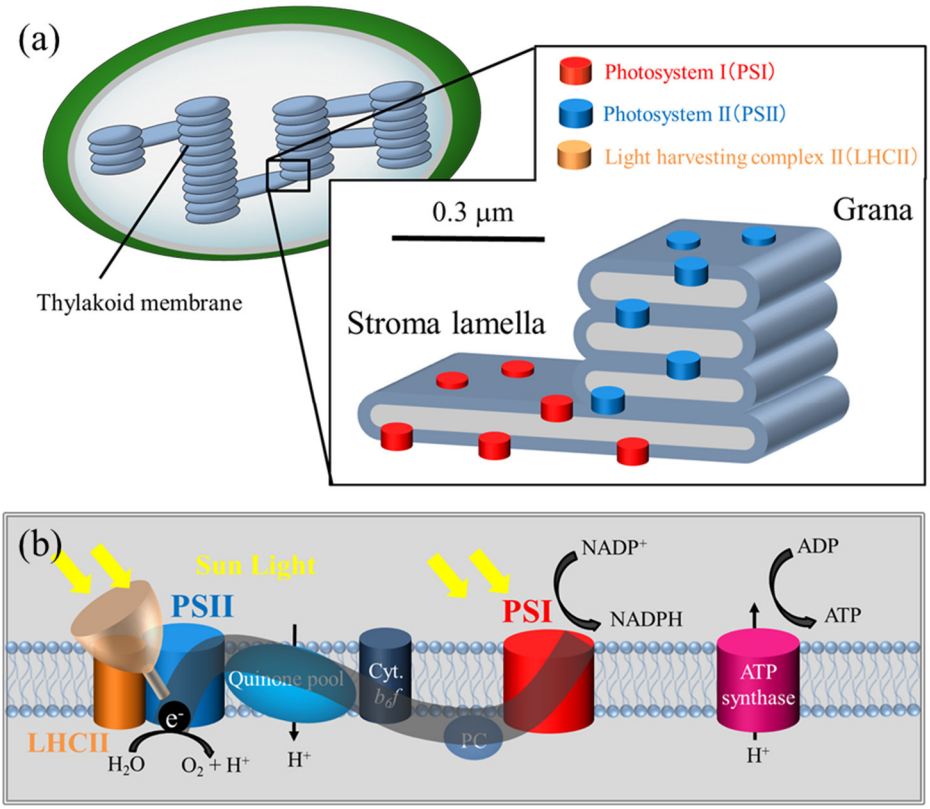

Figure 1-2 Illustrations of internal structure of chloroplast (a) and outline of the thylakoid reaction (b). Pale black thick line in (b) highlights the linear electron transfer from PSII to PSI.

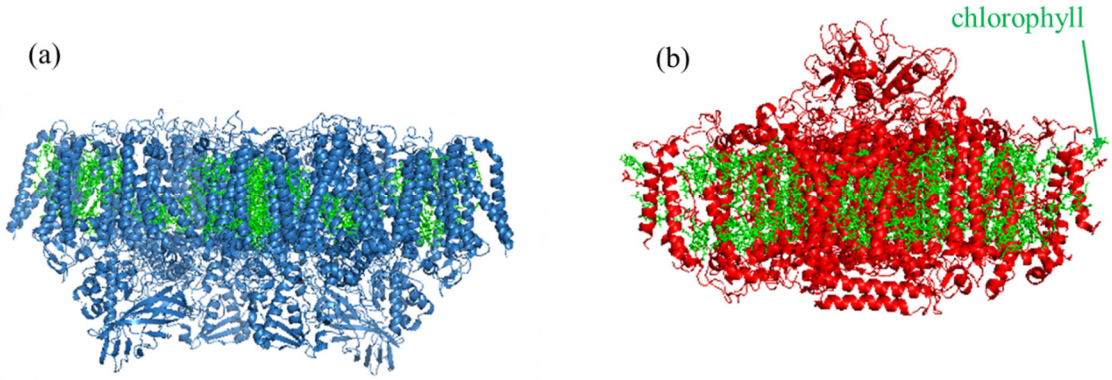

Figure 1-3 Overall structure of PSII (a, pdb code: 6KAF) and PSI (b, pdb code: 7DOJ) viewed from the direction parallel to the membrane. Blue and red cartoons represent polypeptide chains of PSII and PSI, respectively. Chls are shown in green. The images were reconstructed by using a software PyMol.

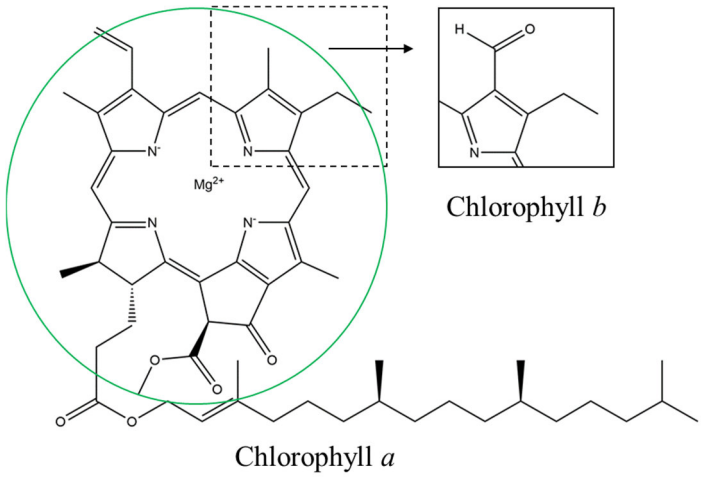

Figure 1-4 Molecular Structure of Chl-*a* and *b*. The chlorin ring containing the π-conjugated system is indicated by green circle. Magnesium ion is coordinated at the center of the ring. Inset highlights difference in the molecular structure between Chl-*a* and *b*.

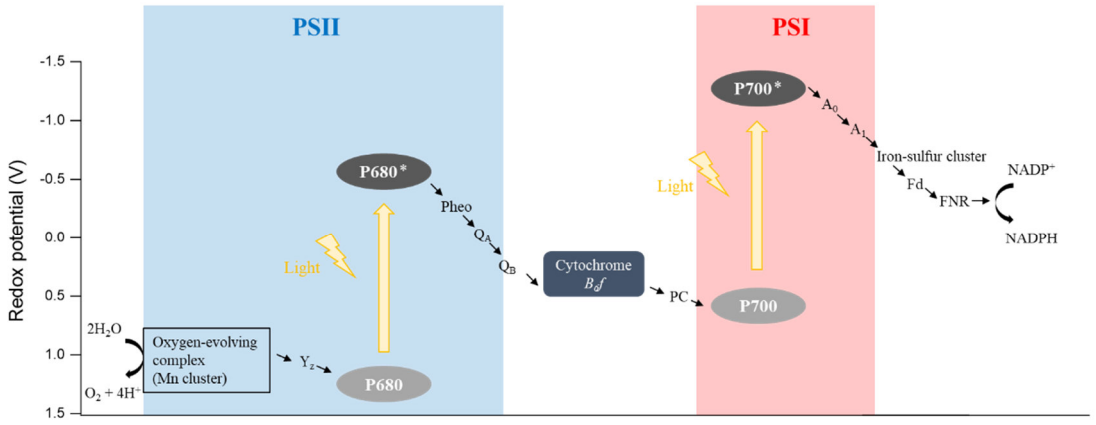

Figure 1-5 Z scheme of oxygenic photosynthesis. It shows the linear electron flow from the water to NADPH through several electron carrier species. The vertical axis indicates the redox potential of the carrier species. P680 and P700 represent the PD of PSII and PSI, respectively. Their excited states are expressed with the asterisk marcs.

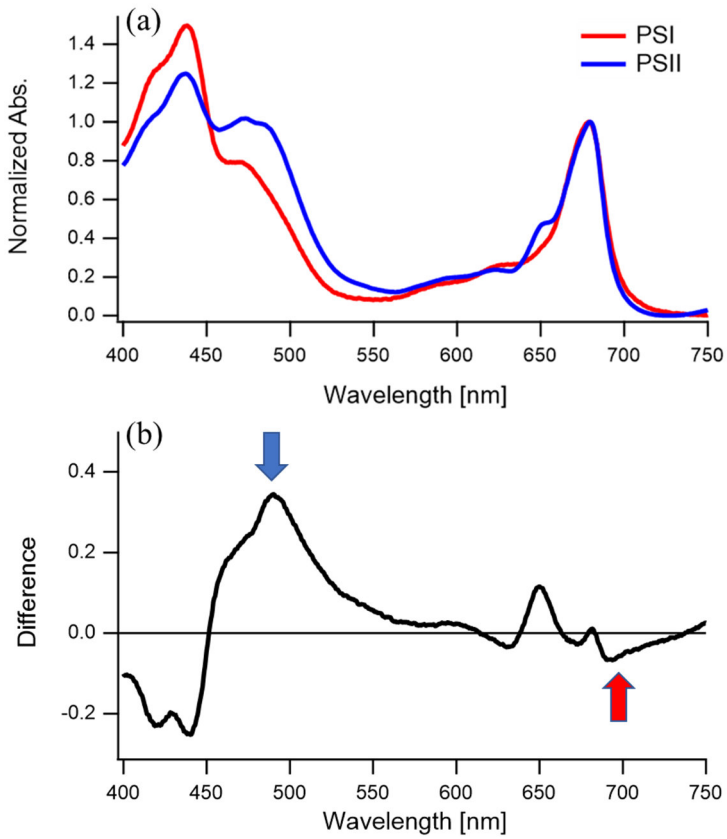

Figure 1-6 (a) Normalized absorbance spectra of PSI (red) and PSII (blue) purified from spinach. (b) Difference spectrum between the two spectra of PSs. Blue and red arrows highlight the wavelengths which preferentially excite PSII and PSI, respectively.

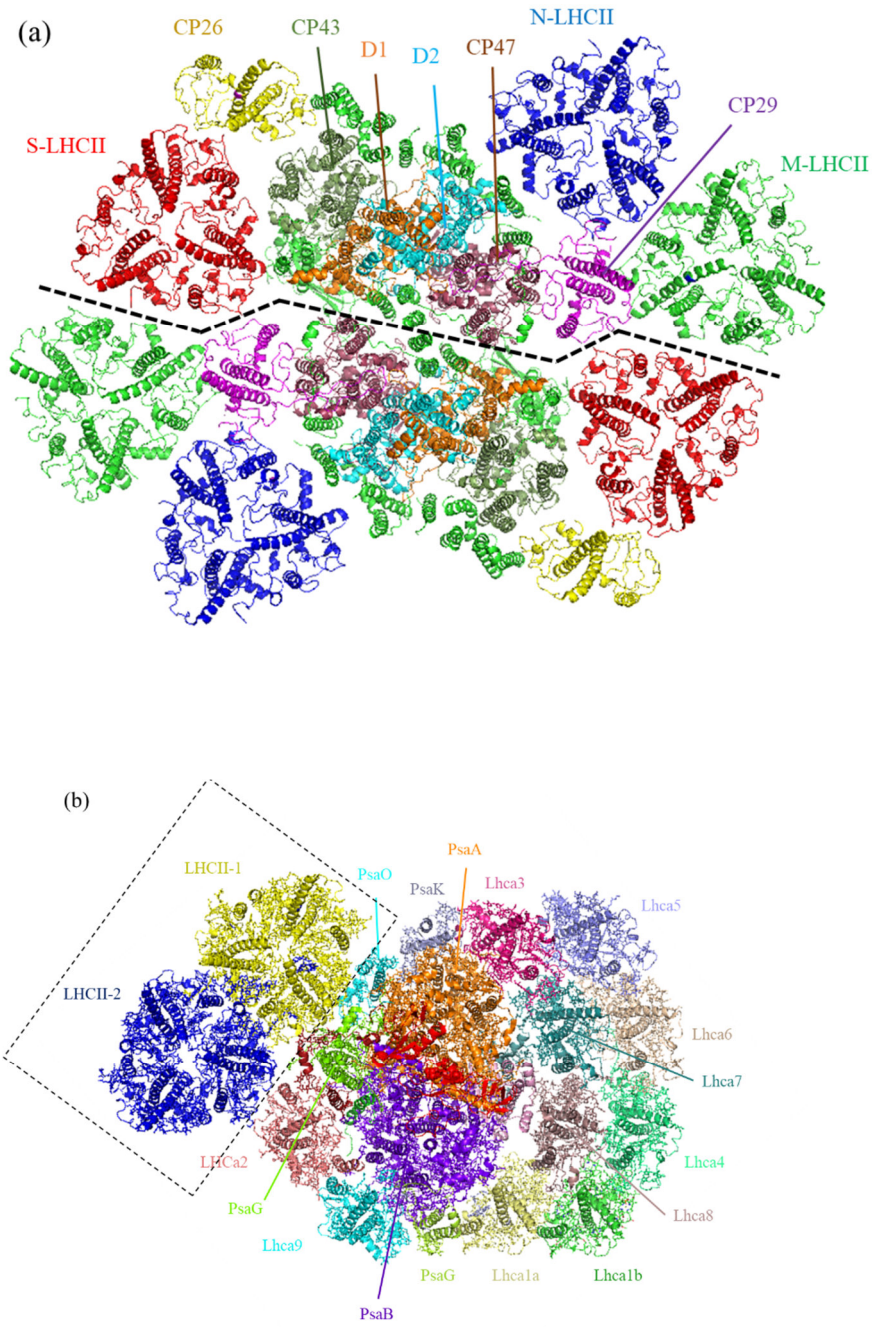

Figure 1-7 Overall architectures of LHCII-PSII super complex (a, pdb code: 6KAF) and LHCII-LHCI-PSI super complex (b, pdb code: 7DOJ) purified from *Chlamydomonas* viewed from the membrane normal. The images were reconstructed by using a software PyMol. Black dotted square highlights the two LHCII trimers which is presumably shuttle between PSII and PSI upon state transitions.

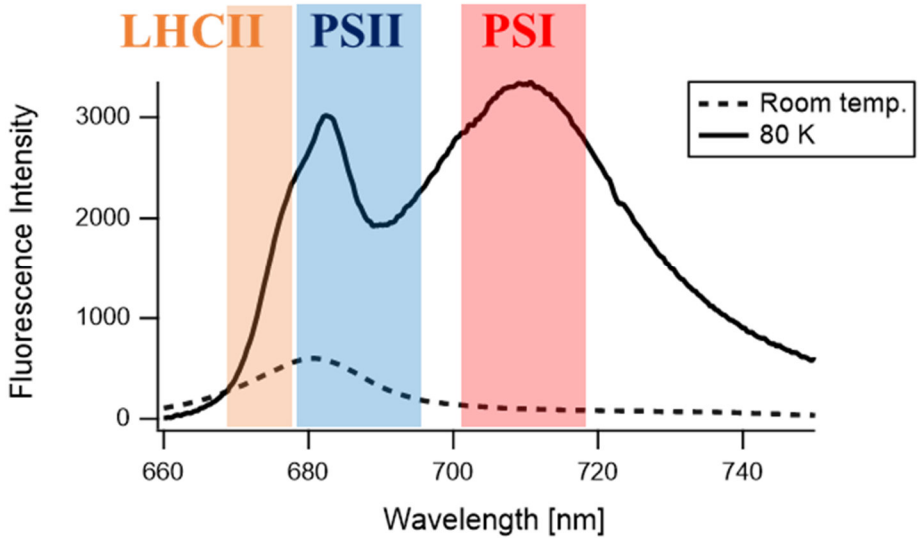

Figure 1-8 Fluorescence spectra at room temperature (dashed line) and 80 K (solid line) obtained from intact *Chlamydomonas* cell suspensions. Colored bands with orange, blue, and red, highlight the contributions from LHCII, PSII, and PSI, respectively.

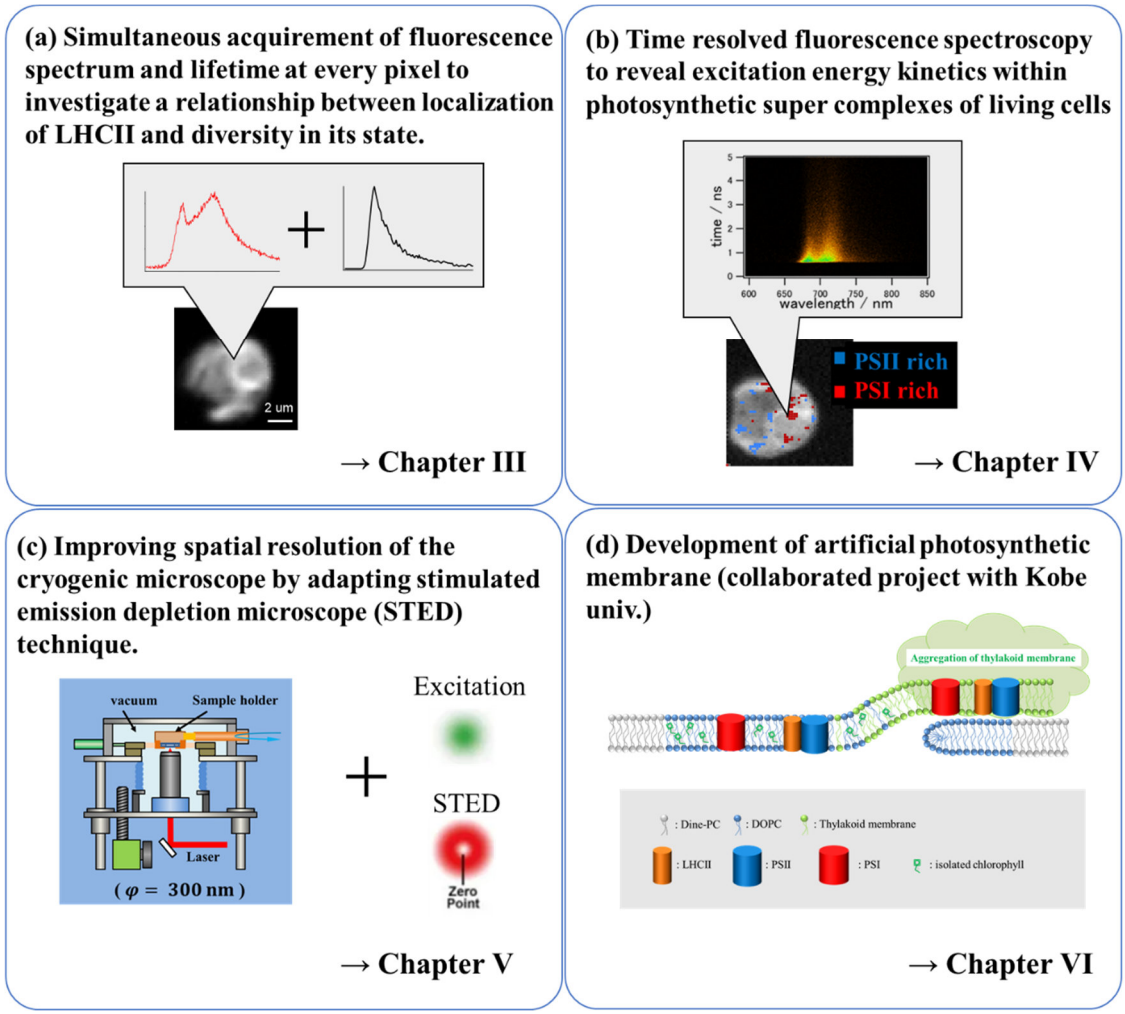

Figure 1-9 Summary of my research in doctoral degree.

Chapter II Materials and Methods

2-1 Growth Conditions of *Chlamydomonas Reinhardtii*

For the investigation of the state transitions, we used unicellular green alga *Chlamydomonas* (strain 139c) and the stt7-mutant which is deficient in the LHCII kinase required to induce state2. They were kindly gifted from Minagawa laboratory in national institute for basic biology. *Chlamydomonas* has characteristic cup-shaped chloroplast that surrounds the nucleus (Fig.2-1). The benefits of this organism as a sample of our research are summarized as follows:

1) The grana-structures where PSII is abundant do not developed well like those of higher plants, offering us a possibility to spatially distinguish the intracellular segregation of two PSs.
2) Easy optical-microscope observations of chloroplast inner structure without purification of it owing to its dominant occupancy within a cell.
3) A robust cell wall protects from the internal damage caused by artificial external forces during a cooling process.
4) Highly viable, and can be cultivated without special treatment or purifications.
5) There are a lot of mutants that are easily available.

Fig. 2-2 shows the cultivation procedure with some photos and images. We used two types of medium, tris-acetate-phosphate (TAP) and high salt (HS), whose compositions are described in Table 2-1 and Table 2-2, respectively. *Chlamydomonas* can grow both heterotrophically and autotrophically. The HSM medium is generally used to restore the function of photosynthesis due to its deficiency of nutrition such as acetic acid, whereas the TAP medium containing acetic acid induces heterotrophical growth of the cells.

Isolated PSII-LHCII and PSI were also kindly gifted from Prof. Minagawa's group. Sucrose-density gradient ultracentrifugation in the presence of amphipol A8-35 was employed during the purification process in order to maintain a stable bond between the core and the peripheral antenna [15].

For the measurement of the cryogenic optical microscope system as described in Chapter III and IV, the cell suspended in the HSM medium was sealed in the hole of a greased Teflon ring spacer (0.5 mm thick, 10 mm outer and 6 mm inner diameters) inserted between two quartz windows (0.3 mm thick, 10 mm diameter) then suspension was set inside the home-built copper holder (Fig. 2-3).

2-2 Induction of the State Transitions

As I mentioned in section 1-4, an imbalance of energy distribution between the two PSs induces a light acclimation mechanism called the state transitions. For the state1 induction, the cell suspension sealed in the holder was incubated in the PSI light (710 nm, ca. 150 μmol photons m^{-2} s^{-1}) for 15 min. [34]. For the induction of state2, glucose (20 mM) and glucose oxidase (50 U ml^{-1}) were added to the sample suspension. Then the suspension was sealed in the holder and incubated in the dark for 15 min to keep anaerobic condition. This treatment keeps the suspension under an oxygen-deficient condition, leading to reduction of the quinone pool [38]. Both the state1 and state2 inductions were conducted with the temperature controlled at 23℃. After these inductions, the cooling process was started. The sample was kept irradiated by the PSI right for state1 or in the dark for state2 until cooled to 80 K. When measuring *STT7*-mutant, the sample was similarly exposed to the state1 or state2 induction condition before measurements.

In general, the state transitions cause a large change in the conventional fluorescence spectrum of chloroplast at 80 K. The fluorescence spectrum of the bulk *Chlamydomonas* suspension were measured by the conventional Fluorimeter (F4500, Hitachi) to concisely assess the inductions of the sufficient state transitions (Fig. 2-4 (a)) [50]. In this case, a 120 W halogen lamp transmitted through a bandpass filter at 710 nm was used as the source of the state1 inducing light. After the induction of the state transitions, the sample was immediately immersed in liquid nitrogen in a Dewar vessel.

2-3 Preparation of Artificial Hybrid Thylakoid Membrane

I started the collaborated research with Assoc. Prof. Morigaki group in Kobe university to realize establishment of artificial photosynthetic membrane. Very recently, Morigaki and co-workers have developed a new type of “hybrid membrane” by incorporating thylakoid components into supported lipid bilayers within an array-patterned template (patterned membrane) [69, 70]. The empty templates were formed by the photopolymerization of diacetylene-phosphocholine (Diyne-PC) lipids with the irradiation of patterned UV light. The templates have exposed lipid bilayer edges, which promote the formation of hybrid membranes consisting of 1,2-dioleoyl-sn-glycero-3-phosphocholine (DOPC) and natural thylakoid membrane. This hybrid membrane is expected to provide a model system to understand photophysical process of photosynthesis.

The patterned membrane with an array of 20×20 μm square shaped empty regions formed on the quartz glass which is used for the cryogenic microscope measurement was kindly given by Morigaki laboratory. The preparation procedure of this is briefly described below.

1) Lipid bilayers of Diyne-PC were deposited onto the quarts substrate by vesicle spreading.
2) The polymerization was conducted by UV irradiation through a photomask.
3) Nonpolymerized Diyne-PC molecules were removed from the substrate surface by rinsing with Milli-Q water extensively.

Incorporation of DOPC + thylakoid membrane was conducted in our laboratory according to the procedure kindly taught by co-worker in Morigaki laboratory. A detail of this procedure is described below.

4) Both the quartz substrate with a pattered membrane and the cell shown in Fig. 2-5 were dried with nitrogen.
5) The substrate was pasted on the cell and immersed with 200 μL thylakoid buffer (10 mM NaCl, 5 mM $MgCl_2$, 50 mM KH_2PO_4, pH 7.0).
6) Sonicate 300 μL of 1 mM DOPC containing 1 mol % NBD-PE (DOPC with its headgroup labeled with nitrobenzoxadiazole) on ice (3W, 30 sec, 4 times, interval 30 sec).
7) Mix 6.54 mL of 0.2415 mg Chl/mL thylakoid membrane and 93.46 mL thylakoid buffer to make 100 mL thylakoid suspension.
8) Add 100 μL DOPC / NBD-PE solution to the above thylakoid suspension to make 200 μL thylakoid / DOPC suspension.
9) Add 120 μL of the above thylakoid / DOPC suspension to the cell where thylakoid buffer is immersed.
10) Incubate for 13 ~ 15 min in the dark.
11) Rinse vigorously by flushing thylakoid buffer onto the substrate.

The thylakoid membrane purified from spinach and the DOPC / NBD-PE solution was kindly gifted from Assoc. Prof. Morigaki's group.

2-4 Home-Built Cryogenic Microscope

We have been developed a novel and hand-made optical microscope system operative at cryogenic temperature [71]. Fig. 2-7 shows an illustration and pictures of the cryostat, which is the core equipment of our cryogenic microscope. The developed cryostat was designed to set a vacuum-compatible objective lens (Plan Apo HR×100 NA=0.9, Mitutoyo) within the heat-

insulating vacuum chamber. This novel design realized the drastic reduction of the distance between the sample and the objective lens, enabling the use of a high-numerical aperture (NA) lens. The sample holder was connected to the cold head of the cryostat (Microstat, Oxford Instrument) and cooled to 80 K by the liquid-nitrogen flow. Temperatures at the sample position were measured with a chromel-AuFe thermocouple. Laser power is reduced by about 90% at the focal plane due to cut-off at the entrance pupil and transmission of the objective lens.

2-5 Introduction of the Standard Cryogenic Optical Microscope System

Fig. 2-8 shows our standard scanning confocal cryogenic optical microscope system. The excitation laser from CW diode laser (Stradus 445, Vortan Laser Technology) at 445 nm was scanned by a pair of galvanic mirrors (VM500 plus, GSI). The objective lens is mounted on a piezo stage (NS7120-C, Nanocontrol), enabling us to move the lens along the optical axis with an accuracy on the order of nm. The fluorescence spectrum at each pixel could be measured with liquid-nitrogen-cooled charge-coupled device (CCD) camera (PyLoN:10BR eXcelon, Princeton Instruments) connected to a polychromator (MS2994i, SOL Instruments). The galvanic mirrors, the piezo stage, and the CCD camera were synchronized by the self-written program of a LabView software (National Instruments), enabling the acquisition of a fluorescence spectrum at every pixel of a 3-D fluorescence image.

Confocal microscopy is an optical imaging technique for improving optical spatial resolution, especially along the optical axis, of a micrograph by means of installing a spatial pinhole to block out-of-focus light in image formation. In our system, the 2-D slit equipped before the polychromator worked as the spatial pinhole conjugated with the focal plane. A fluorescence spot size on the 2-D slit plane ($\Phi_{\mathrm{det.}}$) was estimated by Eq. 2-1,

$$\Phi_{\mathrm{det.}} = [\text{magnification power}] \times \frac{0.61 \times \lambda_{\mathrm{flu}}}{\mathrm{NA}} . \qquad (\text{Equation } 2-1)$$

Here, $[\text{magnification power}]$ was estimated to about 150, and $\Phi_{\mathrm{det.}}$ was calculated to about 72 μm. I typically adopted 50 μm of the 2-D slit size. This system was used for a conventional fluorescence imaging and the main experiment of the collaborated project as described in Chapter VI.

2-6 Introduction of the Cryogenic FLIM System

As I mentioned in section 1-5, a time-resolved fluorescence measurement is a strong

tool for estimation of a concentration of a component which have unknown FQY. The most common and well-established method is that based on the time-correlated single photon counting (TCSPC). The principle of TCPSC is the detection of single photons and the measurement of their arrival times with respect to a reference signal, usually the excitation light (Fig. 2-9). The reference signal is provided by the excitation-laser signals detected by a PIN photodiode (detector 1 in Fig 2-9), whereas single target photons emitted from a sample are detected by a photon-counting avalanche photodiode (detector 2 in Fig. 2-9). The reference pulse and the fluorescence photon signal are input into the start and stop channels of the TCSPC device, respectively. The core part of the TCSPC device is the time to amplitude converter (TAC), which generates an output signal with an amplitude proportional to the time interval between the two input pulses. The TCSPC device memorize the output signals to build a histogram of the signal amplitudes corresponding to the time-profile of the fluorescence decay. TCSPC is a statistical method requiring a high repetitive light source to accumulate a sufficient number of photon events for a required statistical data precision. On the other hand, an accurate fluorescence time profile cannot be obtained when the fluorescence signal is so much that the counting rate of the photons exceeds the repetition rate of the excitation light. Thus, one should choose appropriate signal intensity to realize both high accuracy and sufficient S/N ratio.

Fluorescence lifetime imaging microscopy (FLIM) is an imaging technique, which allows us to view contrast between fluorophores with different lifetimes by means of an acquirement of a fluorescence decay curve at every pixel of the fluorescence image. We applied the FLIM technique to our cryogenic microscope system to investigate a relationship between localization of LHCII and diversity in its state. Fig. 2-10 shows the newly upgraded cryogenic FLIM system. We used a femtosecond titanium sapphire laser (MAITAI, Spectra physics, Mountain View) for the excitation. Pulses at 460 nm generated by a nonlinear optical crystal BBO (β-BaB_2O_4) were used to excite Chl-*b* selectively which is relatively abundant in LHCII than in LHCI and absent in the core part of photosystems. A fluorescence beam was divided by a beam splitter (70% reflection, 30% transmission, BSO22, Thorlabs). The transmitted 30% beam was introduced into the same CCD camera as those used for the fluorescence spectral measurements. The 70% fluorescence reflected by the splitter was focused into an optical fiber bundle connected to an avalanche photodiode (APD) (id100-MMF50, ID Quantique SA), which serves as the detector 2 in Fig. 2-9 and feeds the photon signal to the TCSPC module (SP-130: Becker & Hickl

GmbH). The two detectors (CCD camera, and APD) provide a fluorescence spectrum and a fluorescence decay curve at every pixel of an image at the same time. To the best of my knowledge, it is the first achievement in the world to realize a simultaneous acquisition of both fluorescence spectra and decays in a microscopic area. We put a bandpass filter (MX0680, Asahi Spectra Co., Ltd.) in front of the optical fiber bundle input to selectively detect the LHCII fluorescence at around 680 nm. The fluorescence beam was focused to the confocal pinhole (Φ = 30 μm) before the beam splitter to ensure that both the CCD camera and the APD detected the same sample plane. The fundamental pulse laser was introduced into a PIN photodiode (S9055, Hamamatsu photonics), which serves as the detector 1 in Fig. 2-9 and measures the pulse timing as the trigger signal for the initial point of the time-resolved measurements. The cryogenic FLIM system mainly worked in the experiments described in Chapter III.

2-7 Introduction of the Cryogenic Streak-Camera Optical Microscope System

A streak camera is a time domain photodetector used for picosecond temporal detection from multiple input channels coupled to a polychromator, providing time-wavelength 2D image (streak image). In biological applications, this is a powerful tool for evaluation of protein-protein interactions reflected by such as a kinetics of energy transfer (For detail, see section 2-15). This temporal resolution is achieved by converting the arrival time of photons into their positions on the detector. Figure 2-11 (b) shows a schematic illustration of the streak camera set up. Fluorescence photons dispersed by a polychromator are converted into photoelectrons when entering to the photocathode of the streak camera. A sweeping electrical field orthogonal to the traveling direction is applied to deflect these electrons. The sweeping field varies in time, making the deflected path direction of the photoelectron depends on the original photon arrival time at the photocathode. In our streak camera, the sweeping voltage is linearly risen and synchronized with a repetitive excitation pulse. As a result, in the streak image, the horizontal axis represents fluorescence wavelength and the vertical axis reflecting the deflection distance on the phosphoscreen is proportional to the arrival time of the fluorescence photon.

Recently, I newly upgraded our cryogenic system to realize the detection by the streak camera (Fig. 2-12). The basic contents of the developed system are similar with the cryogenic FLIM system described in a previous section. The 70% fluorescence reflected by the beam splitter was focused to a multi-mode optical fiber with a core diameter of 50 μm (M42L05, Thorlabs) and

delivered to the stage where the streak camera (C10627, Hamamatsu Photonics) is mounted. The fluorescence beam was recollimated by using an objective lens and introduced into the polychromator coupled with the streak camera. This design provides time-resolved fluorescence spectra at microscope scale, which is a first achievement in the world. The cryogenic streak-camera system mainly worked in the experiment described in Chapter IV.

2-8 Introduction of the Cryogenic STED Microscope System

I challenged to apply the STED technique with our cryogenic optical microscope system to view a chloroplast clearly with an improved sub-100 nm spatial resolution. A general principle of the STED technique is described in Fig. 2-13. STED is a point scanning method that uses an excitation laser beam (Ex. beam) focused on the sample to diffraction limited volume. During the scanning, fluorophores within this volume are shifted from electronically ground state to the electronically excited state. A conventional optical microscope allows fluorophores to drop down to the ground state with a release of a stoke shifted emission photon. On the other hand, STED introduces a second laser (STED beam) which has donut-shape and induces stimulated emission from the electronically excited state to vibrationally excited state on the electronically ground state. This process produces a restricted central emission area that is smaller than the diffraction limited spot. Approximating the intensity distribution of the daunt-beam central region is described as,

$$I(r) = I_{\mathrm{D}}\, sin^2\left(\frac{\mathrm{NA}\pi r}{\lambda}\right). \qquad (\text{Equation } 2-2)$$

The spatial resolution in lateral axis is described as,

$$\Phi_{\mathrm{STED}} = \frac{2\lambda}{\pi \mathrm{NA}}\, arc\, sin\frac{1}{\sqrt{2+\frac{I_D}{I_{sat}}}}, \qquad (\text{Equation } 2-3)$$

where NA is a numerical aperture of a microscope objective, I_{D} is the intensity maximum of the donut-beam, and I_{sat} is the saturation intensity. This equation evidence that varying the intensity of the STED beam controls the amount of resolution improvement as this intensity increase does the resolution improvement.

Figure 2-10 shows the optical path of our cryogenic STED microscope system under development. The Ex. and STED beams were generated from the femtosecond titanium sapphire laser at 750 nm. The fundamental laser beam was separated by a polarizing beam splitter, and one

beam was entered into a photonic-crystal fiber (SCG-800; Newport, Irvine, VA) for generation of white excitation beam. A wavelength of the Ex. beam was spectrally selected by a bandpass filter (FLH633-5 Premium Bandpass Filter, Thorlabs), then the beam was introduced to the optical path of our conventional cryogenic system (orange solid line in Fig. 2-14). The remaining fundamental laser beam at 750 nm was used as the STED beam (red solid line in Fig. 2-14) and was passed through a delay stage to vary a total optical-path length of the STED beam, ensuring the adjustment of the arrival times of the two pulses, Ex. beam and STED beam. Finally, the two beams were overlapped at focal plane of the objective lens. A polarization maintaining optical fiber serves to lead the STED beam near the cryostat and extend the pulse width. The two beams were coupled by a dichroic mirror (FF735-Di02-25x36, Semrock) and focused into a sample in the cryostat. A vortex phase plate (VPP) (V-775-10-1, Vortex Photonics) is a diffractive optical element that convert a Gaussian beam profile to a donut-shaped one. As detectors, we used the same CCD camera and the APD as those used for the FLIM system. The second-harmonics pulses of the fundamental laser generated by the nonlinear optical crystal BBO was input to the PIN photo diode as the trigger in the time-resolved measurement (blue solid line in Fig. 2-14). Evaluations of the performances of the cryogenic STED microscope is described in Chapter V.

As samples for the performance evaluation of this system, 10^{-5} M ATTO647N (Sigma-Aldrich) aqueous solution and 1000-fold-diluted aqueous suspension of F8807 fluorescent beads (FluoSpheres™ Carboxylate-Modified Microspheres) containing 1% polyvinyl alcohol (PVA) were spin coated on glass substrates. Figure 2-6 shows normalized fluorescence spectra with the 600-nm excitation wavelength (solid lines) and excitation spectra with the 720-nm monitor wavelength (dotted lines) of ATTO647N aqueous solution (green) and F8807 aqueous suspension (black). Blue and red vertical lines represent the wavelengths of Ex. and STED beams applied with the cryogenic STED microscope system, respectively. The longer-wavelength tail of the fluorescence spectra, which reflects the energy difference between the electronically excited state and vibrationally excited state on the electronically ground state, overlaps with the wavelength of the STED beam, allowing the effective fluorescence depletion by the stimulated emission.

2-9 Calibration of the Pixel Size

The galvanic mirror used in the present setup consists of two mirrors which control the position of the excitation laser focus spot in the X and Y directions. It is controlled by inputting

an integer value ($\mathrm{channel}_x$ and $\mathrm{channel}_y$ for X and Y direction, respectively) corresponding to the angle of each mirror to the LabVIEW software. The XY positions of the laser spot at the focal plane are expressed by the following equations.

$$\mathrm{X} = \mathrm{channel}_x \times d_x + \mathrm{X}_0\,, \qquad (\mathrm{Equation}\ 2-4\ \mathrm{a})$$

$$\mathrm{Y} = \mathrm{channel}_y \times d_y + \mathrm{Y}_0\,, \qquad (\mathrm{Equation}\ 2-4\ \mathrm{b})$$

where d_x and d_y are the effective displacement distances of the laser spot on the focal plane for X axis and Y axis, respectively. X_0 and Y_0 represent the offset. For the estimation of d_x and d_y, an objective micrometer (OB2011, Shibuya Kogaku), which is a plate-glass with an engraved grid-pattern with an interval of 10 μm, was scanned by the excitation laser and a two-dimensional image was obtained by means of a detection of the scattered light signal. The lines are engraved under the cover glass with a thickness of 0.17 mm. The vacuum-compatible objective lens is designed to form an ideal focal spot on a cover glass with a thickness of 0.3 mm. Another cover glass with a thickness of 0.17 mm was taped on the surface of the objective micrometer for an installation of glass medium with an approximately ideal thickness. The titanium sapphire laser at 430 nm was selected as the excitation laser because the scattered light signal effectively passed through the dichroic mirror and was easily detected. Fig 2-15 shows obtained scattering image of the objective micrometer with 100×100 pixels (85 channel per unit pixel). The plot in Fig. 2-15 shows the engraved lines. The results of its liner fittings and the positions of the intersections of the engraved lines are shown as the red lines and red circles, respectively.

Fig. 2-16 shows a schematic diagram of lines obtained by the fittings. Let φ be the angle between the line L and the X axis and let $\Delta\mathrm{A}$ be the distance between the intersections of another fitting lines perpendicular to L and the X axis. $\Delta\mathrm{A}$ is simply calculated by the following equation,

$$\Delta\mathrm{A}\ [\mathrm{um}] = 10 \times \frac{1}{cos\,\varphi}\,. \qquad (\mathrm{Equation}\ 2-5)$$

In addition, let g be the slope of L,

$$g = tan\,\varphi = \frac{sin\,\varphi}{cos\,\varphi},$$

$$cos^2\,\varphi = \frac{1}{g^2+1}\,. \qquad (\mathrm{Equation}\ 2-6)$$

Here, $\Delta\mathrm{A}$ can be calculated from Eq. 2-5 by substituting g obtained by the fitting to Eq. 2-6.

The value of d_x can be estimated by dividing the obtained ΔA by the number of channels required to travel a distance of ΔA. The value of g and the number of channels were calculated by averaging over the values derived from the multiple fitting lines. You can also find the value of d_y in the same way as above and estimated d_x and d_y are shown below, respectively,

$$d_x = 6.494\ [\mathrm{nm}]\,, \qquad \text{(Equation } 2-7\text{ a)}$$

$$d_y = 6.572\ [\mathrm{nm}]\,. \qquad \text{(Equation } 2-7\text{ b)}$$

2-10 Spatial Resolution of the Cryogenic Optical Microscope

Theoretical spatial resolutions of a conventional optical microscope in the lateral and optical axis are represented as,

$$\Phi_{\mathrm{lateral}} = 0.61 \times \frac{\lambda}{\mathrm{NA}}, \qquad \text{(Equation } 2-8\text{ a)}$$

$$\Phi_{\mathrm{optical}} = 1.28 \times \frac{\lambda n}{(\mathrm{NA})^2}, \qquad \text{(Equation } 2-8\text{ b)}$$

where *n* is the refractive index of the sample space. Theoretical spatial resolutions in the lateral and optical axis with 460 nm excitation laser used in our system are estimated to be about 0.3 μm and 1.0 μm, respectively.

In order to confirm the actual spatial resolution in our system, I conducted 3D scanning of a standard fluorescence beads (F8811, FluoSpheres™ Carboxylate-Modified Microspheres) which is yellow-green fluorescent (505/515) with 0.2 μm diameter. Figure 2-17 (a) shows the fluorescence images of a bead measured while scanning the objective lens stepwise in 0.5 μm increments in the optical axis direction. The relative position Z of the objective lens in the optical axis direction is shown in the figure. In this measurement, we used the standard cryogenic optical microscope system previously introduced in section 2-5. Excitation intensity measured before the cryostat was 0.5 μW. Each image has 17×17 pixels, and the pixel size of the image is 65 nm in the X direction and 66 nm in the Y direction. The detector exposure time was 50 ms per pixel. A contrast of the fluorescence image is unified in all the images. As the fluorescent bead approach the focal point of the objective lens, the size of the bright spot in the fluorescence image shrinks and the fluorescence intensity at the center increases. On the other hand, the image of the fluorescent bead at the out-of-focus position was blurred.

All the obtained images were fitted with the 2D Gaussian function expressed below,

$$F(x) = z_0 + A \cdot exp\,[-\frac{1}{2(1-cor^2)}(\left(\frac{x-x_0}{x\text{Width}}\right)^2 + \left(\frac{y-y_0}{y\text{Width}}\right)^2 - \frac{2 \cdot cor \cdot (x-x_0)(y-y_0)}{x\text{Width} \cdot y\text{Width}}.$$

(Equation $2-9$)

Here z_0 is the background signal of the image, xWidth and yWidth are the widths of the obtained fitting function in the X and Y directions (perpendicular to the optical axis), and cor is the correction factor for the tilt of the ellipse from the X axis. Typical result of the 2D Gaussian function fitting is superimposed as contour lines on the image of Z=2.0 [μm] in Fig. 2-17 (a). The estimated two-dimensional widths, xWidth and yWidth, were converted into the one-dimensional full width at half maximum (FWHM) (Γ_{XY}) by the following equation,

$$\Gamma_{\mathrm{XY}} = 2 \cdot \sqrt{2 \cdot \ln 2 \cdot x\text{Width} \cdot y\text{Width} \cdot \sqrt{1-cor^2}}\,. \qquad \text{(Equation } 2-10)$$

The calculated (Γ_{XY}) and Amplitude corresponding to the peak value of each image are plotted against Z (Fig. 2-17 (b)). Γ_{XY} corresponds to the size of the bead image, and the minimum value of Γ_{XY} (0.37 mm) is used as the effective spatial resolution in the lateral axis of our cryogenic optical microscope system. The plot of the amplitude was fitted with a one-dimensional Gaussian function, and the calculated FWHM is used as the effective spatial resolution in the optical axis of the system.

2-11 Wavelength-Calibration for the CCD Camera and the Streak Camera

The wavelength calibration of the CCD camera was performed by measuring the light from standard neon lamp and mercury lamp with the known peak wavelengths of the emission lines. The center wavelength of the spectroscope was set to 650 nm, and the diffraction grating was set to 300 grv / mm. Table 2-3 shows the wavelengths of the emission lines from the neon and mercury lamps (right column) and the peak positions of the corresponding lines detected by the CCD camera (left column). These values were linearly fitted to estimate the wavelengths corresponding to all pixel numbers in the CCD camera.

The wavelength calibration of the streak camera was performed by only measuring the light from the standard neon lamp. The center wavelength of the spectroscope was set to 700 nm, and the diffraction grating was set to 50 grv / mm. Table 2-4 shows the wavelengths of the emission lines from the neon lamp and the peak positions of the corresponding lines detected by the streak camera. In the same way as above, the linear fitting provided the wavelengths corresponding to all pixel numbers in the streak camera.

2-12 Time-Resolution of the TCSPC and the Streak Camera Measurement

Instrument response function (IRF) is defined as the temporal response of a measuring system to an impulsive input and determines the time resolution of the measuring system. It is device-specific and does not depend on a fluorescence matter. We estimated IRFs of the cryogenic FLIM system (see section 2-6) and cryogenic streak-camera optical microscope system (see section 2-7), by measuring a standard dye malachite green (Nacalai tesque) which is known to exhibit a sufficiently shorter fluorescence lifetime (< 1 ps) than the expected IRFs [78,79]. Fig. 2-18 shows fluorescence decay curves of a 10^{-4} M malachite green aqueous solution measured with the cryogenic FLIM system and the cryogenic streak-camera optical microscope system. Both curves were fitted to a single Gaussian function (blue lines in Fig. 2-18) and each fitting curve was interpreted as the effective IRF of each system. FWHMs of IRFs were estimated to be 42.6 ps and 27.0 ps for the cryogenic FLIM system and the cryogenic streak-camera optical microscope system, respectively.

2-13 Correction of a Photon Detection Delay Related to Fluorescence Wavelength

In the cryogenic streak-camera optical microscope system, emitted fluorescence photons pass through the optical fiber before the detection by the streak camera (see section 2-7). An optical fiber is generally designed to allow light to travel within its core by means of a total internal reflection. It causes the chirp of the transmitted light, that is the dispersion of the passing speed of photon depending on its wavelength due to the difference in refractive index. Figure 2-19 (a) shows a streak image of a 10^{-4} M malachite green aqueous solution which exhibits a very fast fluorescence decay measured with the cryogenic streak-camera optical microscope system. The pixel numbers on the vertical and horizontal axes of the streak image linearly correspond to the delay time for the photon arrival and its wavelength, respectively. In this measurement, monitor ranges of the delay time and wavelength are from 0 to 2 ns and from 594 to 840 nm, respectively. A photon with shorter wavelength intrinsically exhibits a higher refractive index and the slower the passing speed of an optical fiber, causing a negative correlation between the delay time and the wavelength in the streak image. The chirp effect due to the optical fiber passage was corrected by using the malachite green data according to the procedure shown below.

1) A limited spectral range of the streak image of the malachite green from 679 nm to 733 nm containing the main band of Chl fluorescence was extracted.

2) Five decay curves were obtained by dividing the extracted image into five along the wavelength axis and integrating them (red solid lines in Fig. 2-19 (b)). Since the fluorescence lifetime of malachite green is much faster than the instrumental response, Gaussian-like decay curves were obtained (see section 2-12).
3) Each of the obtained decay curves was fitted with a single Gaussian function (blue solid line in Fig. 2-19 (b)). The estimated peak positions are superimposed as white crosses in Fig. 2-19 (a).
4) The estimated peak position was plotted vs. the wavelength and fitted to a linear function (red solid line in Fig. 2-19 (a)).
5) The entire original streak image is corrected so that the tilting due to the chirp effect gets horizontal (Fig. 2-19 (c)).

The variation in a refractive index of a photon is not proportional to its wavelength, that is, the delay time caused by the passage of an optical fiber does not exhibit a linear correlation with the wavelength. Even though, we assumed a liner correlation within the interested wavelength region (from 680 nm to 730 nm) to simplify the correction analysis.

The obtained coefficients from the liner fitting in the procedure 4) are represented below. The tilt due to the chirp effect is expressed as,

$$P_y = -0.0891 \times P_x + 175.76\,, \qquad \text{(Equation } 2-11\text{)}$$

where P_y and P_x represent pixel numbers of vertical and horizontal axes which correspond to the delay time and wavelength, respectively. The corrected streak image (Fig. 2-19 (c)) in which the time 0 of a fluorescence decay curve matches within the objective wavelength band was generated by means of shifting each pixel of the original streak image along the vertical axis by calculated P_y.

2-14 Fitting of Fluorescence Lifetime

A measured fluorescence decay curve can be mathematically interpreted as a convolution of the IRF and the fluorescence decay curve which would be obtained with infinitely fast IRF. The latter can be often modeled by the sum of exponential functions as shown below. A measured fluorescence decay curve can be mathematically interpreted as a convolution of the IRF and exponential decay models as shown below.

$$F(t, t_0, \sigma) = A_0 + \mathrm{IRF}(t_0, \sigma) \otimes \sum_{i=1}^{n} A_i \cdot e^{-\frac{t}{\tau_i}} \cdot H(t) \ , \qquad \text{(Equation } 2-12\text{)}$$

where A_0 is the background, t_0 and σ represent the center position and the width of the IRF, respectively. A_i and τ_i are the amplitude and time constant of *i*-th exponential decay model, respectively. H is the Heaviside step function. The fitting of an obtained fluorescence decay curve to the above equation by a software Igor Pro (WaveMetrics) takes a huge time due to the analysis including the convolution. If we assume a Gaussian function for the IRF, Eq. 2-12 can be rewritten,

$$F(t) = A_0 + \int_{-\infty}^{\infty} \frac{1}{\sigma\sqrt{\pi}} \cdot e^{-\left(\frac{t_1 - t_0}{\sigma}\right)^2} \cdot \sum_{i=1}^{3} A_i \cdot e^{--\frac{t-t_1}{\tau_i}} \cdot H(t - t_1)\, dt_1 \ , \quad \text{(Equation } 2-13 \text{ a)}$$

$$= A_0 + \sum_{i=1}^{3} A_i \cdot \frac{1}{\sigma\sqrt{\pi}} \cdot e^{-\frac{t-t_0}{\tau_i}} \cdot e^{\frac{\sigma^2}{4\tau_i^2}} \int_{-\infty}^{t} e^{-\frac{1}{\sigma^2}\left(t_1 - t_0 - \frac{\sigma^2}{2\tau}\right)^2} dt_1 \ . \qquad \text{(Equation } 2-13 \text{ b)}$$

When $k = \frac{t_1 - t_0 - \frac{\sigma^2}{2\tau}}{\sigma}$ is applied,

$$= A_0 + \sum_{i=1}^{3} A_i \cdot \frac{1}{\sqrt{\pi}} \cdot e^{-\frac{t-t_0}{\tau_i}} \cdot e^{\frac{\sigma^2}{4\tau_i^2}} \int_{-\infty}^{\frac{t - t_0 - \frac{\sigma^2}{2\tau_i}}{\sigma}} e^{-k^2} dk \ , \qquad \text{(Equation } 2-13 \text{ c)}$$

$$= A_0 + \sum_{i=1}^{3} \frac{A_i}{2} \cdot e^{-\frac{t-t_0}{\tau_i}} \cdot e^{\frac{\sigma^2}{4\tau_i^2}} \cdot erf\left(\frac{t - t_0 - \frac{\sigma^2}{2\tau_i}}{\sigma}\right) \ , \qquad \text{(Equation } 2-13 \text{ d)}$$

where erf is the error function originally built in as a unique function of Igor Pro with the following definition,

$$erf(x) = \frac{2}{\sqrt{\pi}} \int_0^x e^{-t^2} dt \ . \qquad \text{(Equation } 2-14\text{)}$$

Since Eq. 2-13 d does not include the convolution, it is possible to perform the fitting in a much shorter time.

2-15 DAS Analysis

A streak-camera method provides time-resolved fluorescence spectral data. Here, I introduce a powerful analysis method, decay associated spectra (DAS) analysis expressed by the following equation,

$$F(t,\lambda) = \sum_{i=1}^{n} A_i(\lambda) \cdot e^{-\frac{t}{\tau_i}}, \qquad \text{(Equation } 2-14\text{)}$$

which generates spectra associated with the specific time constants. This allows us to elucidate energy transfer kinetics within a sample.

Figure 2-20 shows a simulation model where the excitation energy on a 680-nm (L_{680}) emitting pigment is fed to a 690-nm emitting one (P_{680}) with a rate constant of k_e. The excitation energy is assumed to dissipate at the same time as fluorescence with a rate constant of k_f. Rate equations of the two components, L_{680} and P_{680} are represented as follows,

$$\frac{d[L_{680}]}{dt} = -(k_e + k_f)[L_{680}], \qquad \text{(Equation } 2-15\text{ a)}$$

$$\frac{d[P_{690}]}{dt} = k_e[L_{680}] - k_f[P_{690}], \qquad \text{(Equation } 2-15\text{ b)}$$

$$[L_{680}] = [L_{680}]_0 e^{-(k_e+k_f)t}, \qquad \text{(Equation } 2-16\text{ a)}$$

$$[P_{690}] = \frac{k_e[L_{680}]_0}{k_e - k_f}(e^{-k_f t} - e^{-k_e t}). \qquad \text{(Equation } 2-16\text{ b)}$$

In the derivation of Eq. 2-16, the general solution of a linear first-order differential equation is applied to Eq. 2-15. In general, the value of k_e is much larger than k_f. Therefore, the Eq. 2-16 can be approximated as follows,

$$[L_{680}] = [L_{680}]_0 e^{-k_e t}, \qquad \text{(Equation } 2-17\text{ a)}$$

$$[P_{690}] = [L_{680}]_0 (e^{-k_f t} - e^{-k_e t}). \qquad \text{(Equation } 2-17\text{ b)}$$

Note that both $[L_{680}]$ and $[P_{690}]$ contain the exponential decay components with the same decay rate k_e. The component in $[L_{680}]$ has a positive amplitude, whereas that in $[P_{690}]$ has a negative amplitude indicating a gradual increase of the population with time.

In our DAS analysis, obtained fluorescence decay curve at each wavelength was globally fitted to the model in Eq. 2-13 d under a constraint that the time constant τ_i was the same for decays at all wavelengths, whereas the amplitude A_i depends on the wavelength. Figure 2-20 (b) shows a schematical graph plotting the estimated A_i against wavelength. Note that black solid line in Fig. 2-20 exhibits a plus peak at around 680 nm and a minus peak at around 690 nm. This represents the amplitude of the exponential decay with the time constant of τ_e corresponding to that of the excitation energy transfer from L_{680} to P_{680}. As I mentioned above, the plus and minus amplitudes reflect contributions from signals emitted from donner and accepter

components of the excitation energy transfer, respectively. Besides, black dotted line in Fig. 2-20 (b) exhibits only a plus peak. This component represents amplitude of the exponential decay with the time constant of τ_f corresponding to that of the spontaneous fluorescence emission. In summary, the DAS analysis allows us to identify donner and accepter states with the excitation energy transfer and states with the spontaneous fluorescence emission and quenching. DAS analysis also enables to determine the rate constants of these processes. We applied this analysis for the experiment described in Chapter IV.

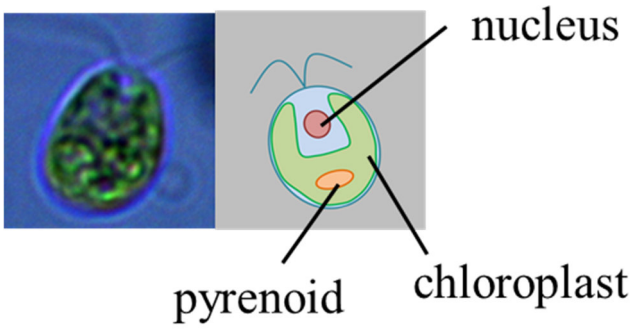

Figure 2-1 (Left image) Transmission image of *C. reinhardtii*. (Right image) An illustration represents the internal structure of the cell.

① Culture on TAP medium with white light irradiation (20~30 µmol photons $m^{-2}s^{-1}$) at 23 °C

② Small amount of cells were harvested by a platinum loop in the clean bench

③ Culture on liquid TAP medium with white light irradiation (50 µmol photons $m^{-2}s^{-1}$) at 23 °C and rotary shaking at 150 rpm for 3 ~ 4 days

④ Cells were harvested and resuspended in liquid HSM medium through centrifugation

⑤ Culture on HSM liquid medium with white light irradiation (60 µmol photons $m^{-2}s^{-1}$) at 23 °C and rotary shaking at 150 rpm for 1 days

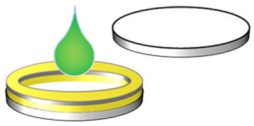

⑥ Sealed with a teflon ring coated with vacuum grease and quartz glass.

Figure 2-2 Cultivation procedure. Composition of TAP and HSM medium are described in table 2-1 and table 2-2.

Figure 2-3 The sample holder for the cryogenic optical microscope system. The sample-holder surface was gold-coated with enhanced reflection to reduce the thermal conductance via the infrared radiation.

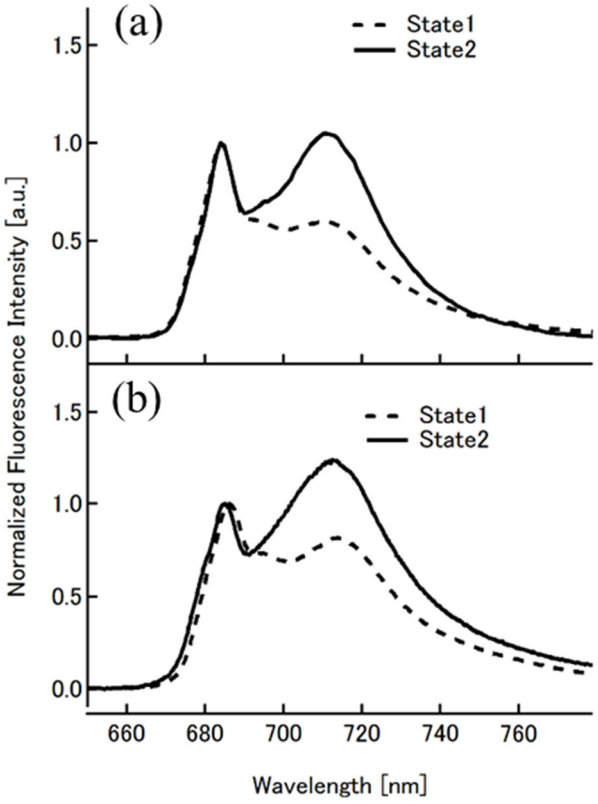

Figure 2-4 77-K fluorescence spectra of *C. reinhardtii* in state1 (dashed lines) and state2 (solid lines). The spectra in panel (a) and (b) were measured using the conventional fluorescence spectrometer and the home-built cryogenic optical microscope, respectively. The excitation wavelength was 445 nm for both cases. For original data, please see ref [50].

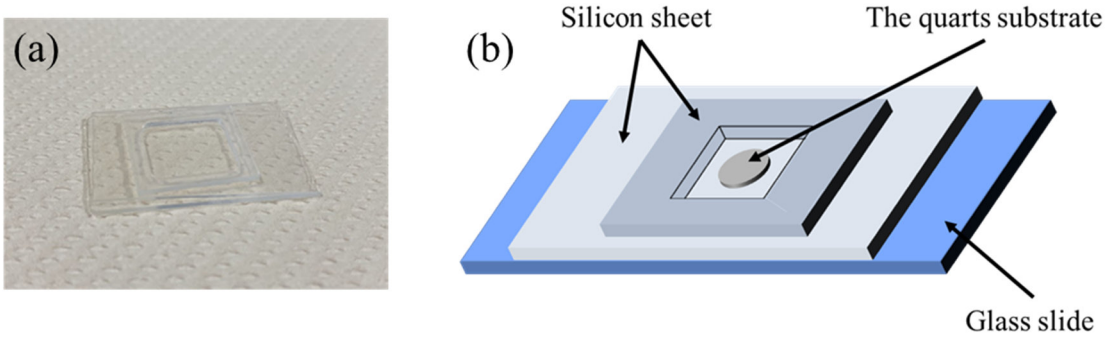

Figure 2-5 (a) A picture of the cell used for the incorporation of DOPC + thylakoid membranes to the patterned membrane. (b) An illustration of the structure of the cell. The upper silicon sheet with a square hole accommodates the suspension. The lower silicon sheet realizes robust sticking of the substrate to the cell and prevents the substrate to escape from the cell during the intense rinse process.

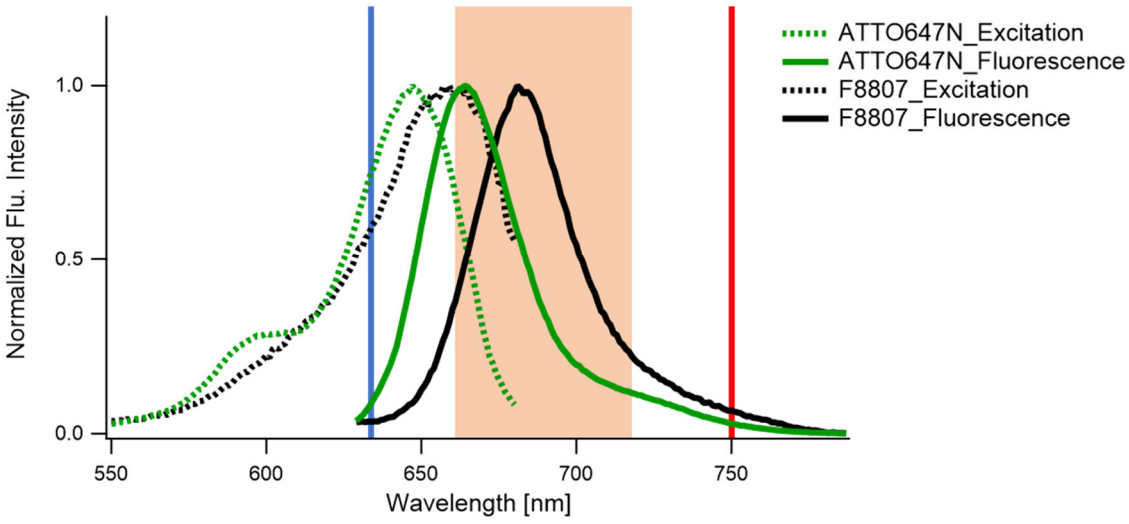

Figure 2-6 Normalized fluorescence (solid curves) and excitation spectra (dashed curves) of ATTO647N (green) and F8807 (black) aqueous solution. Blue and red vertical lines represent the wavelengths of Ex. and STED beams applied with the cryogenic STED microscope system, respectively. Orange fill highlights the detected wavelength through the dichroic mirror used in the present cryo-STED system.

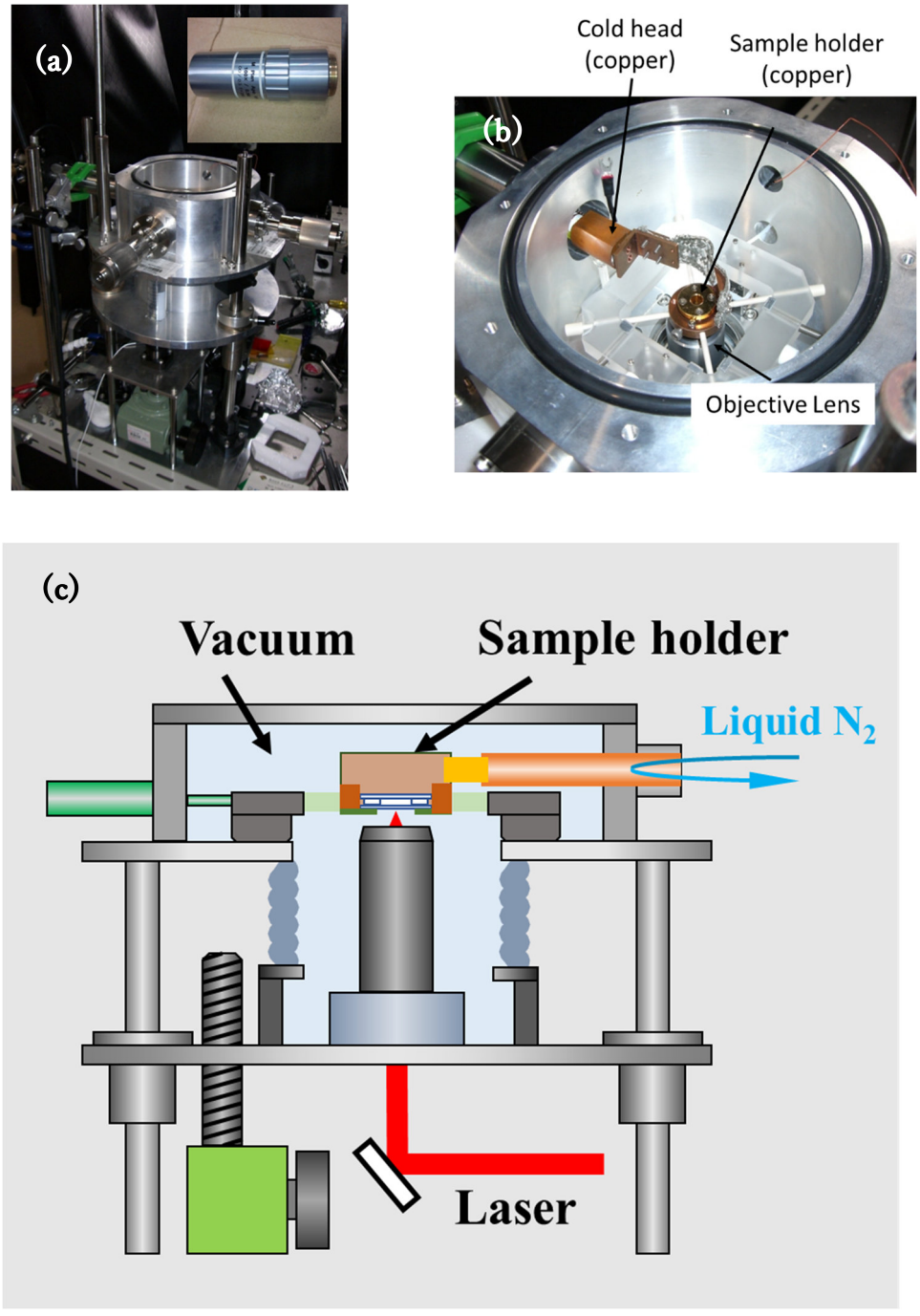

Figure 2-7 (a) A picture of the whole cryostat. An inserted picture shows the vacuum-compatible objective lens which is mounted within the chamber. (b) A picture of the inner room of the vacuum chamber. (c) An illustration of internal structure in the cryostat.

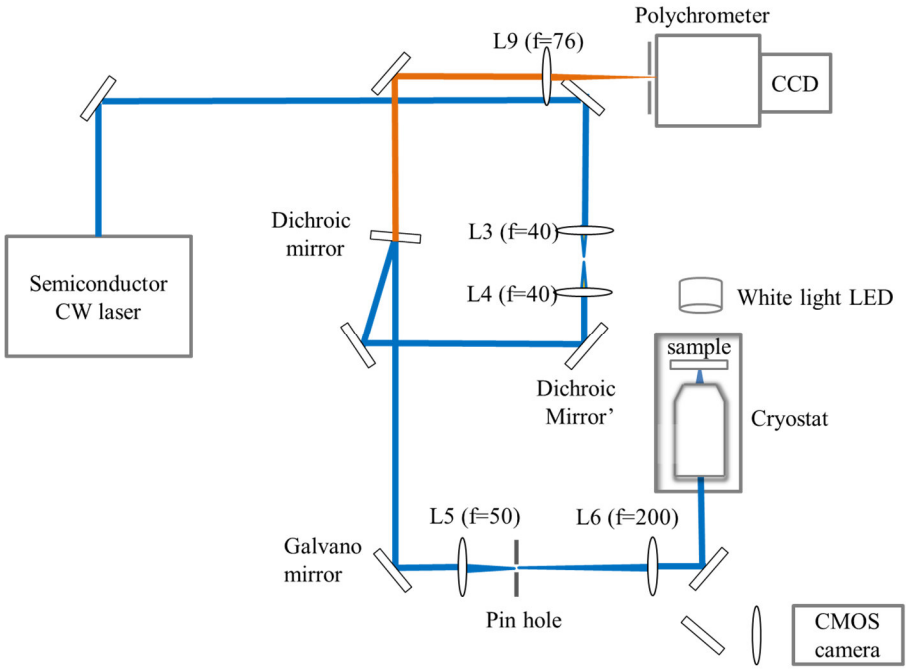

Figure 2-8 The optical path of the standard scanning confocal cryogenic optical microscope system. This system provides fluorescence spectrum at every pixel of a fluorescence image.

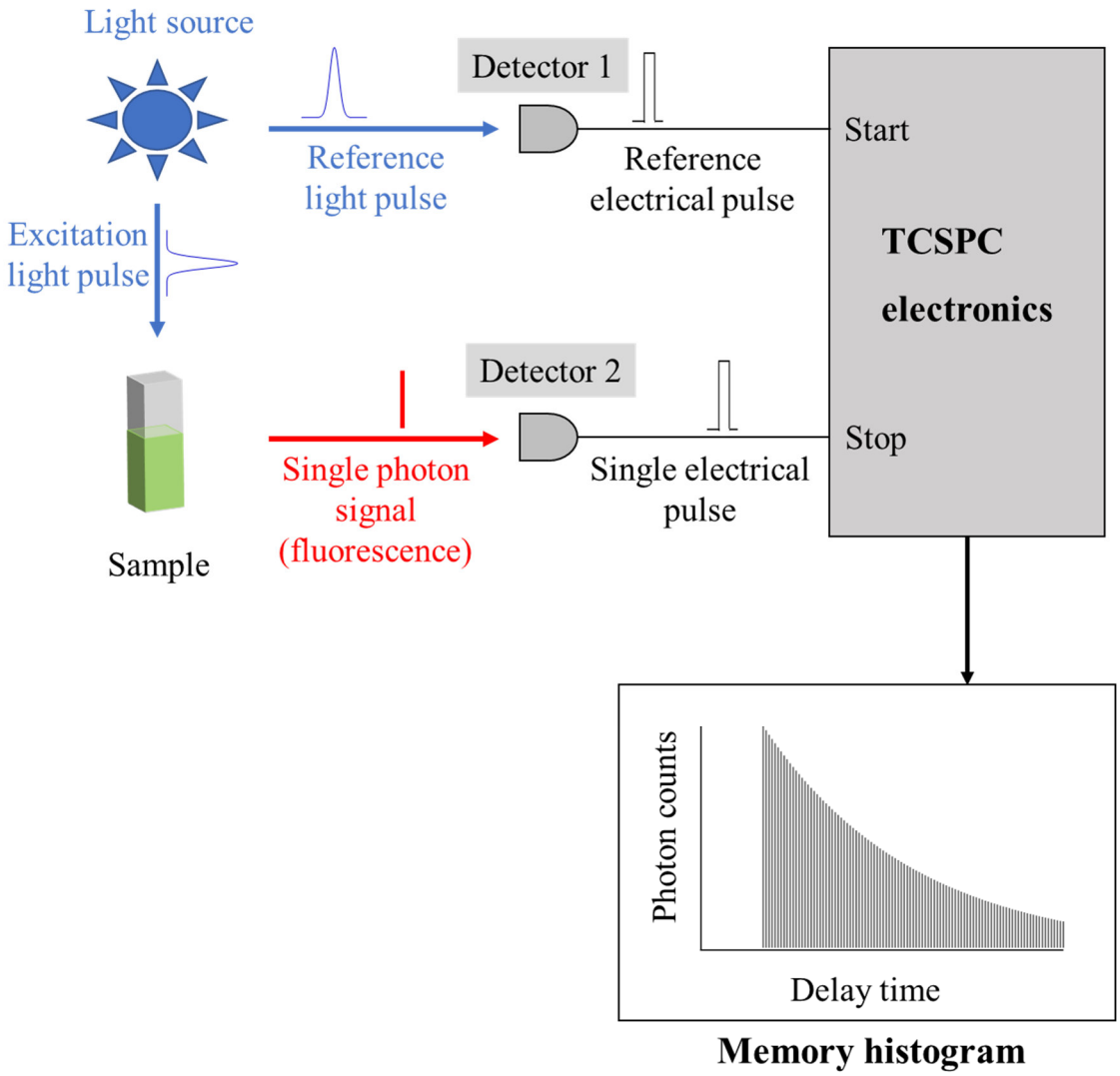

Figure 2-9 A schematic illustration of TCSPC method.

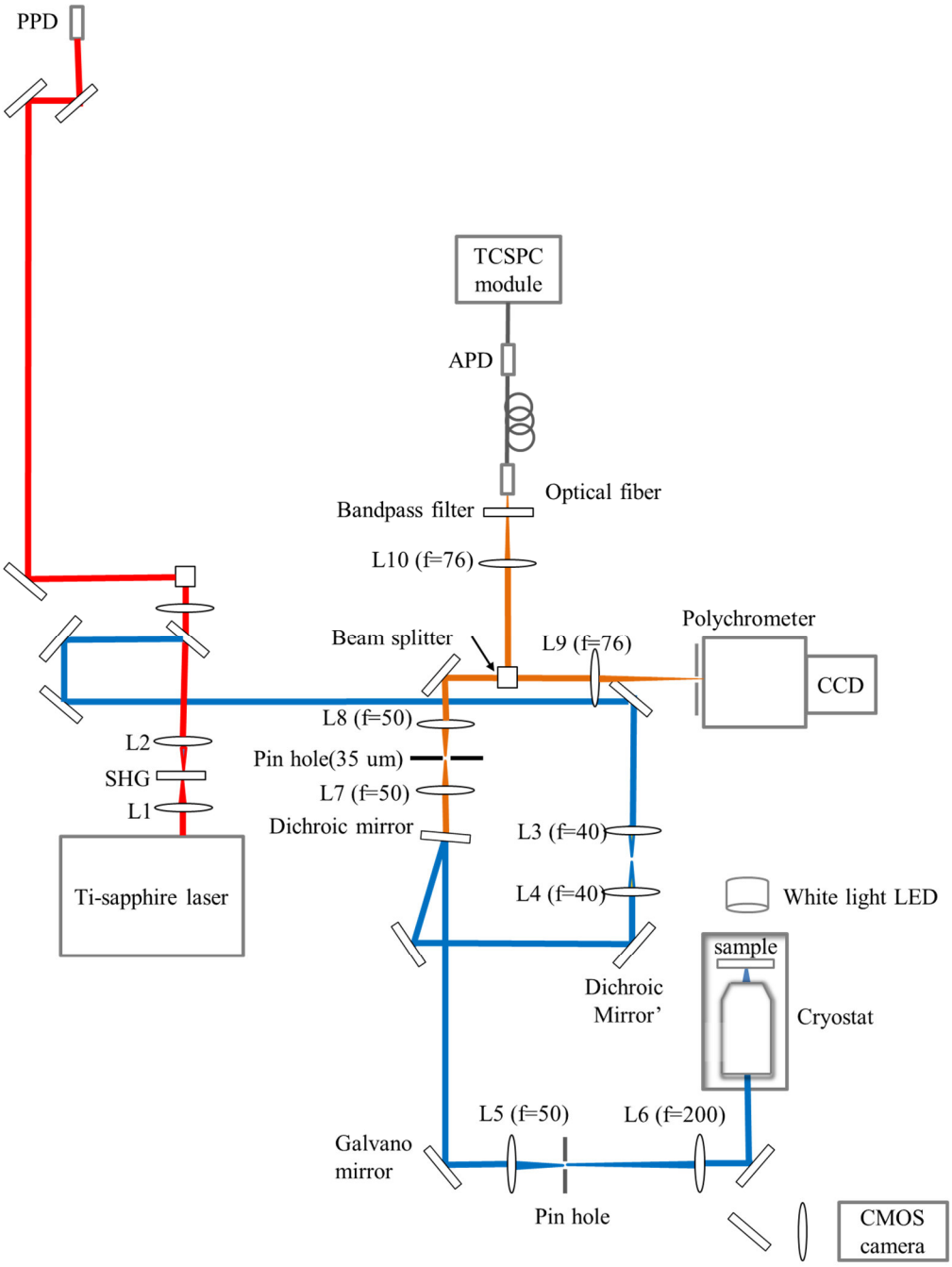

Figure 2-10 The optical path of the novel cryogenic FLIM system. This system simultaneously provides fluorescence spectrum and lifetime at every pixel of a fluorescence image.

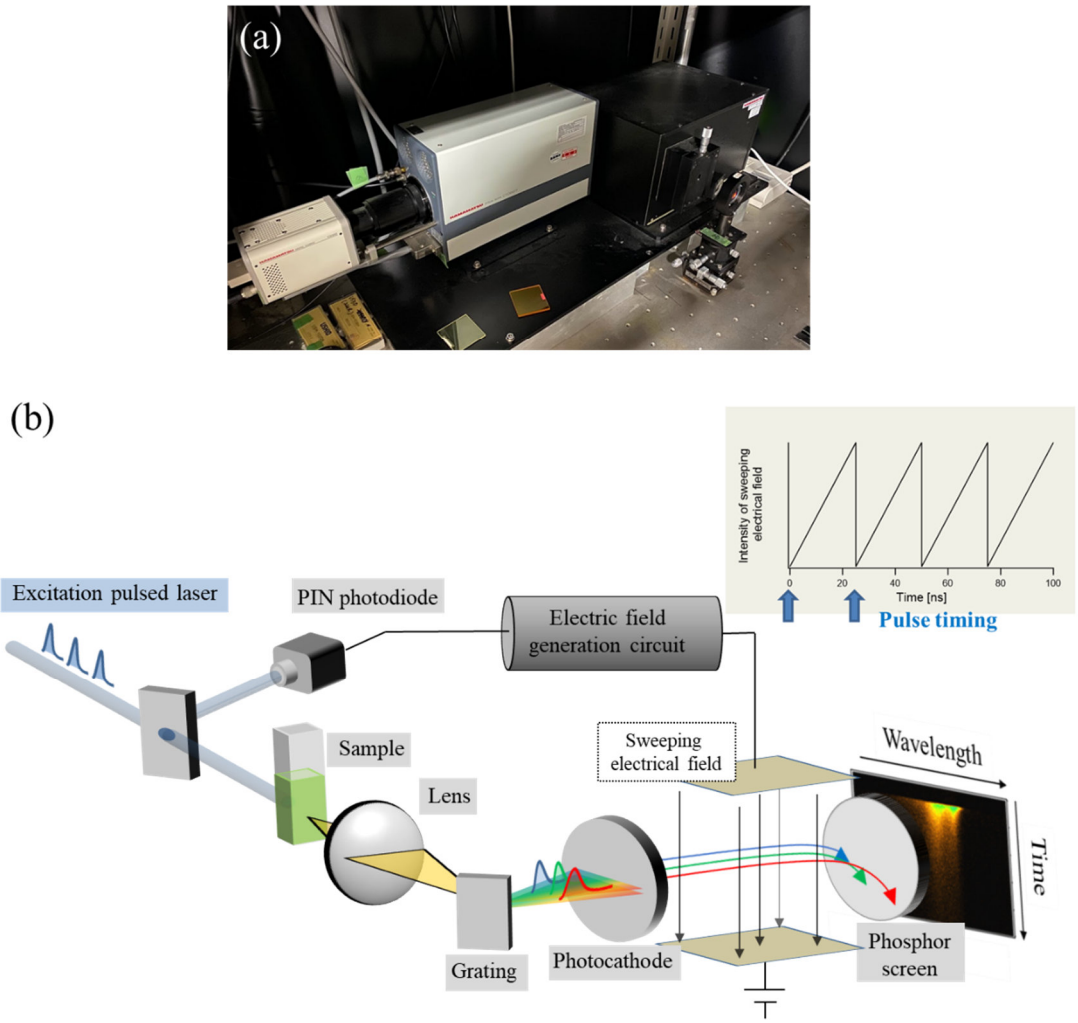

Figure 2-11 (a) A picture of the streak camera. (b) A schematic illustration of the streak camera setup. The inset graph shows the temporal variation of the intensity of the sweeping electric field applied perpendicular to the traveling direction of the photoelectron.

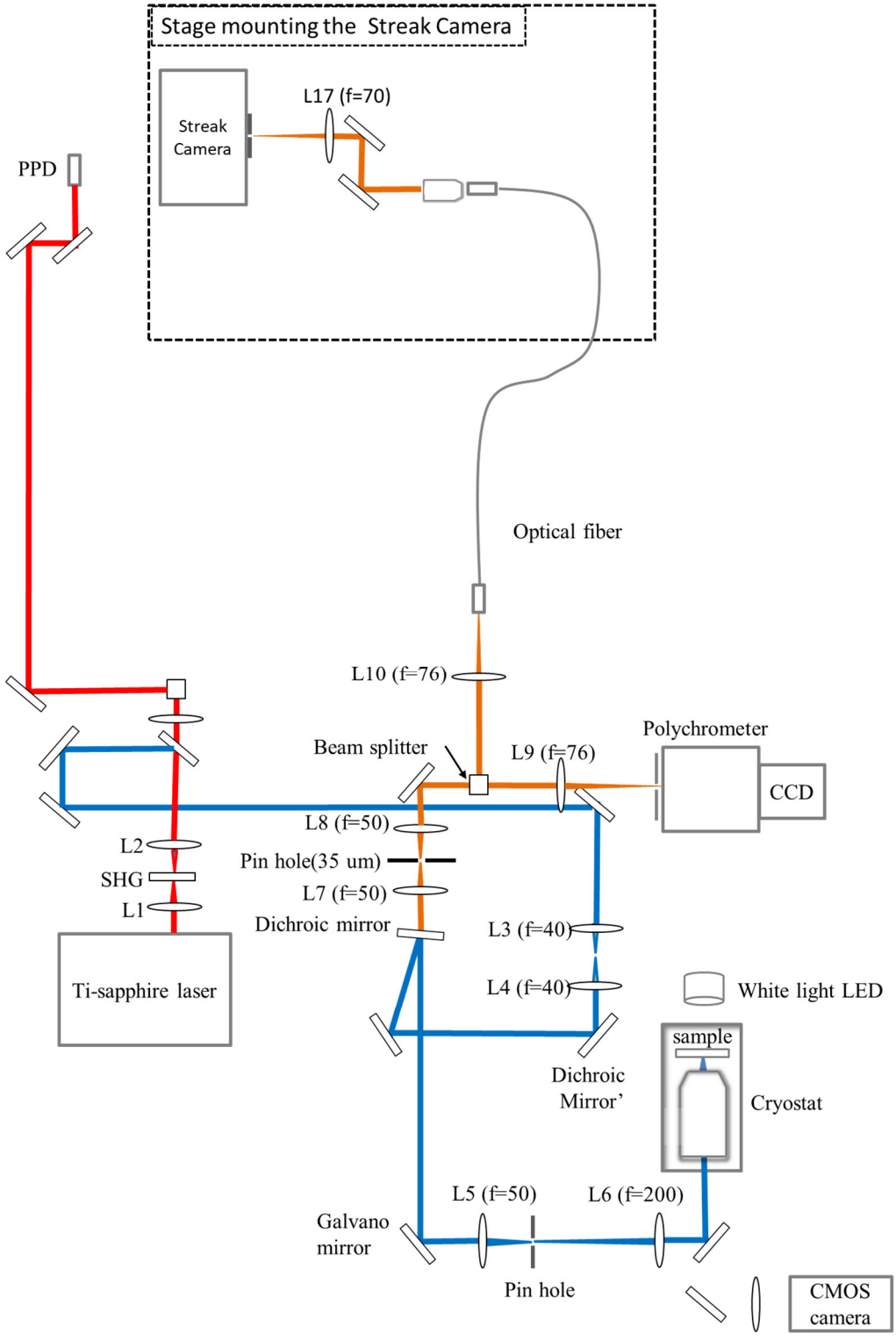

Figure 2-12 The optical path of the novel cryogenic streak-camera optical microscope system. This system provides a time-wavelength 2D image at arbitrarily chosen areas in a microscope image specified by the LABVIEW program.

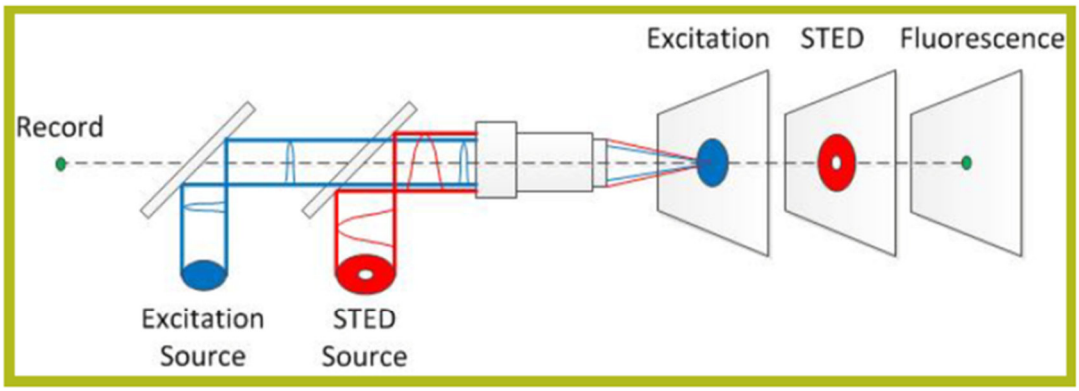

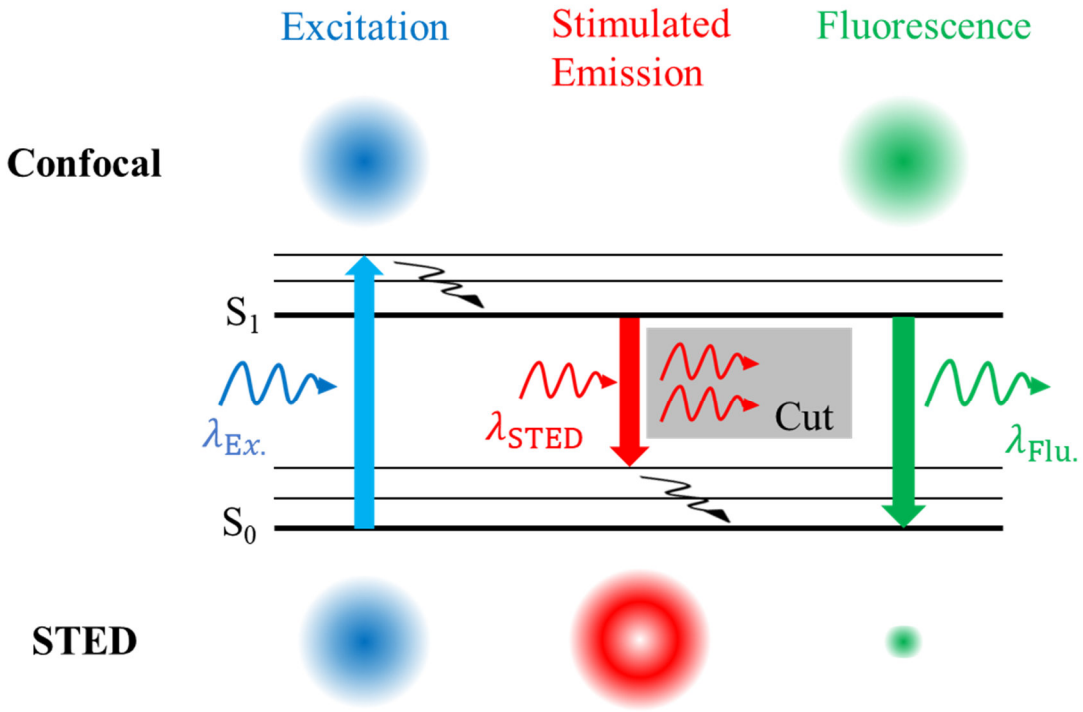

Figure 2-13 A schematic illustration of the STED technique.

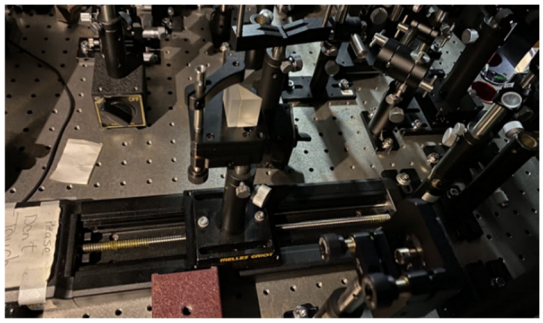

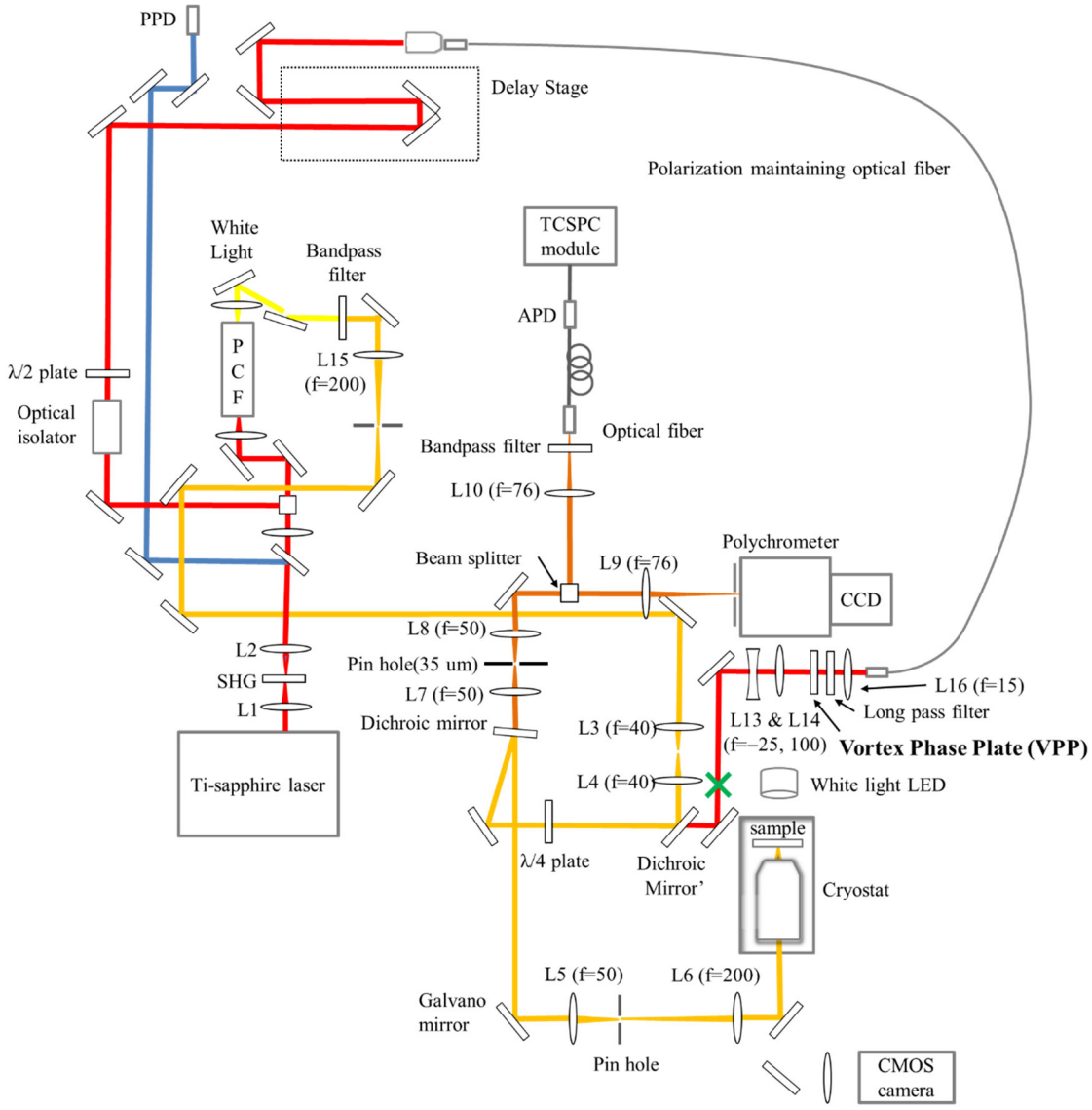

Figure 2-14 The optical path of the cryogenic STED microscope system under development. The inset shows the picture of the delay stage. The green cross indicates the place of the C-MOS camera used for the measurement of the shape of the STED beam as described in section 5-3.

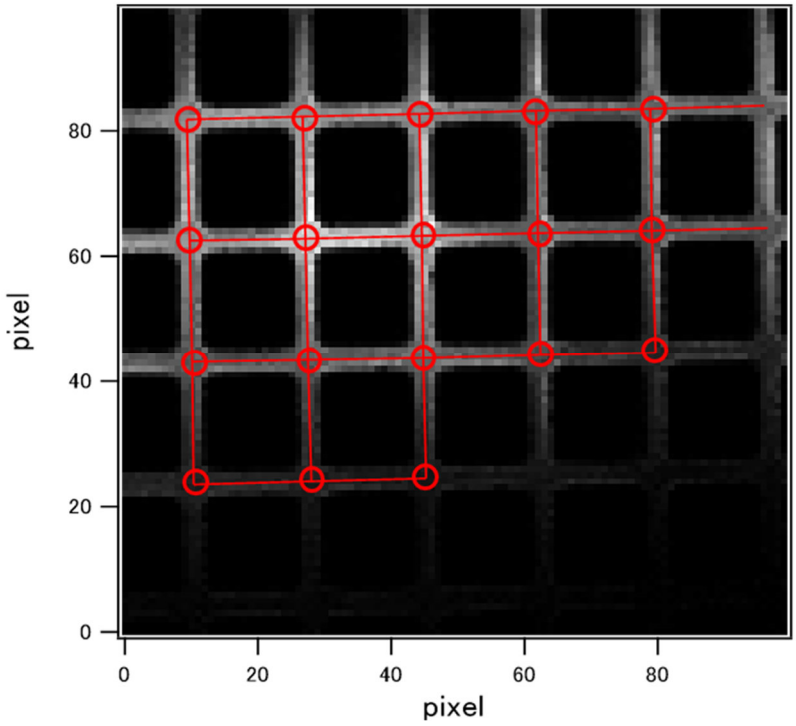

Figure 2-15 The image of the objective micrometer detected by the scattered light of the excitation laser (430 nm) from the surface. The intersections and liner fitting result are superimposed with the red circles and lines, respectively.

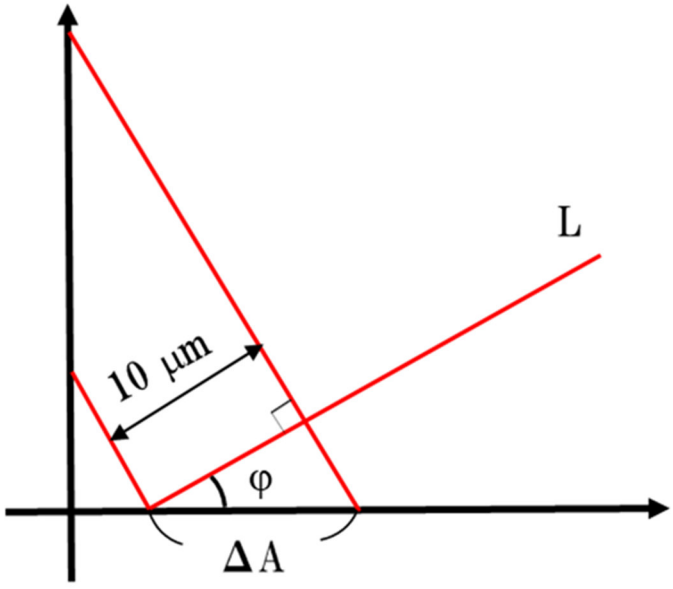

Figure 2-16 The schematic illustration for the calibration of the effective pixel size from the liner fitting result in Fig. 2-15.

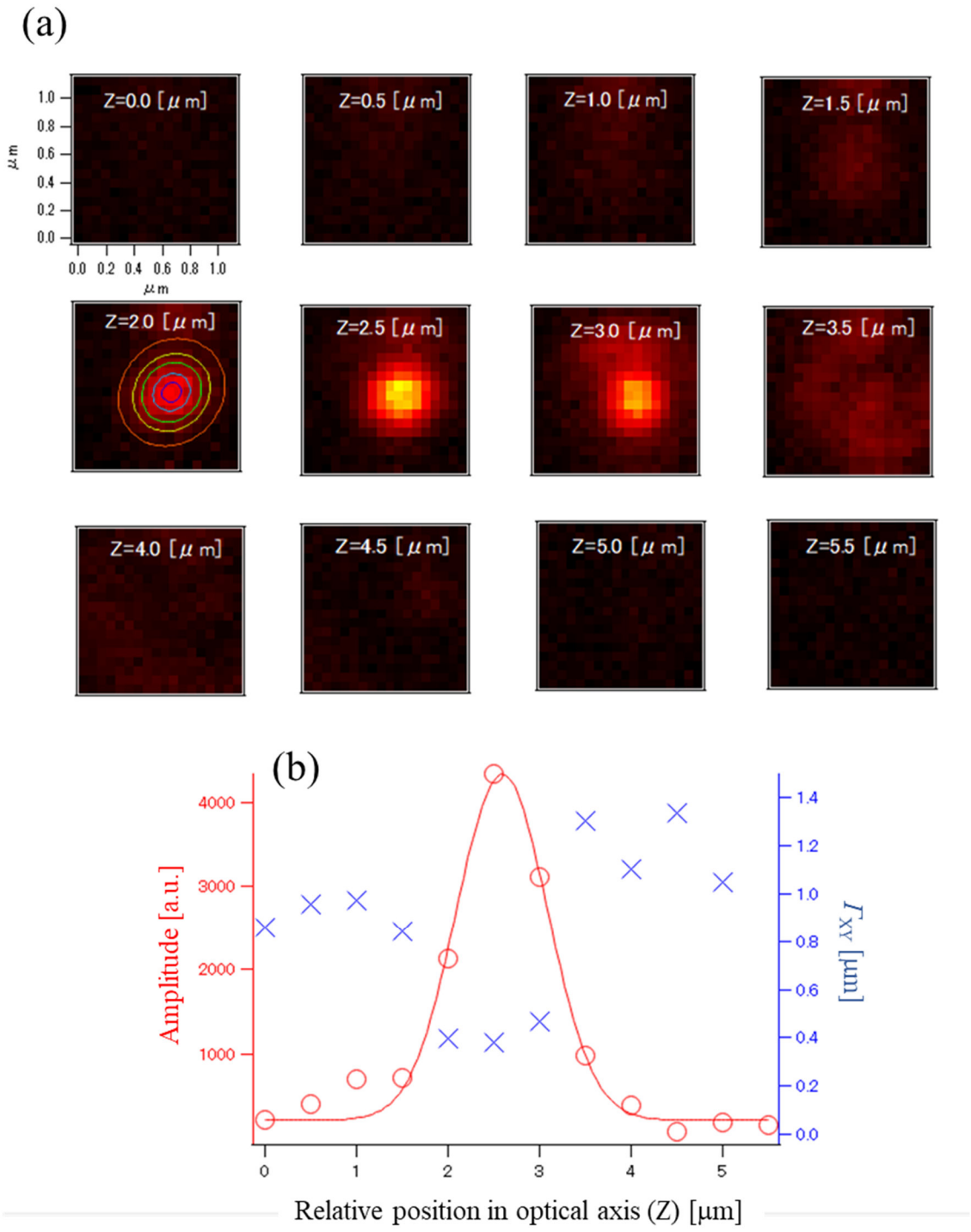

Figure 2-17 (a) Fluorescent images of a standard fluorescent bead acquired while varying stepwise the axial position of the objective lens. (b) FWHM of the bead image in XY direction at each optical axis position (Γ_{XY} (blue cross)) and fluorescence peak intensity (A (red circle)). The solid red line is the fitting curve by a Gaussian function.

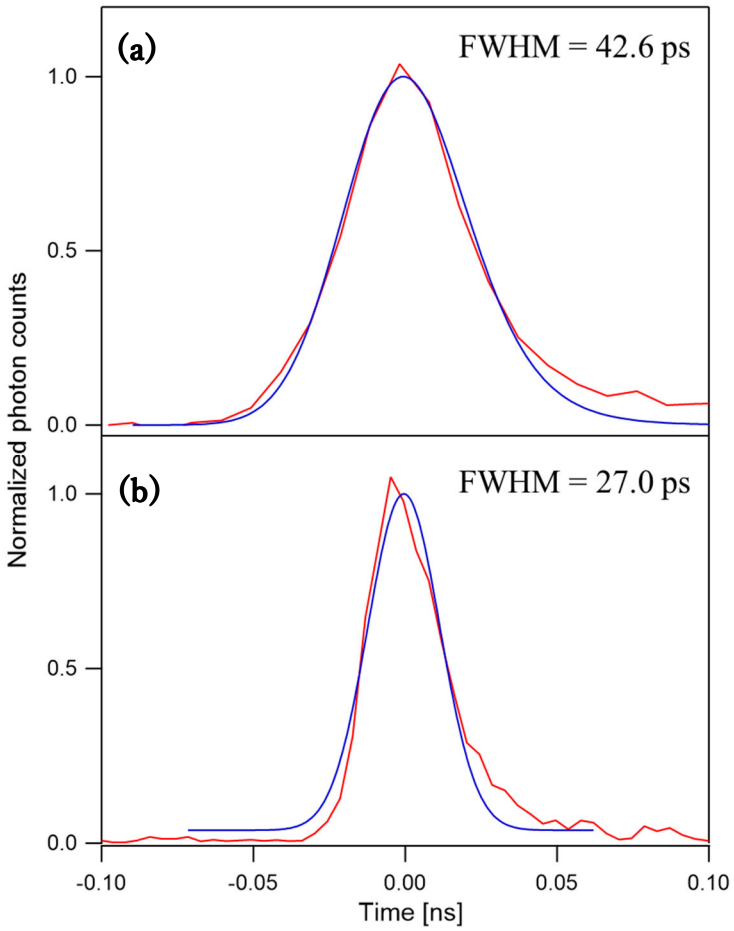

Figure 2-18 The fluorescence decay curves of a malachite green aqueous solution (red lines) measured with the cryogenic FLIM system (a) and the cryogenic streak-camera optical microscope system (b). The results of Gaussian fitting (IRF) are superimposed as blue solid lines. Estimated FWHM of each IRF is indicated in the graph.

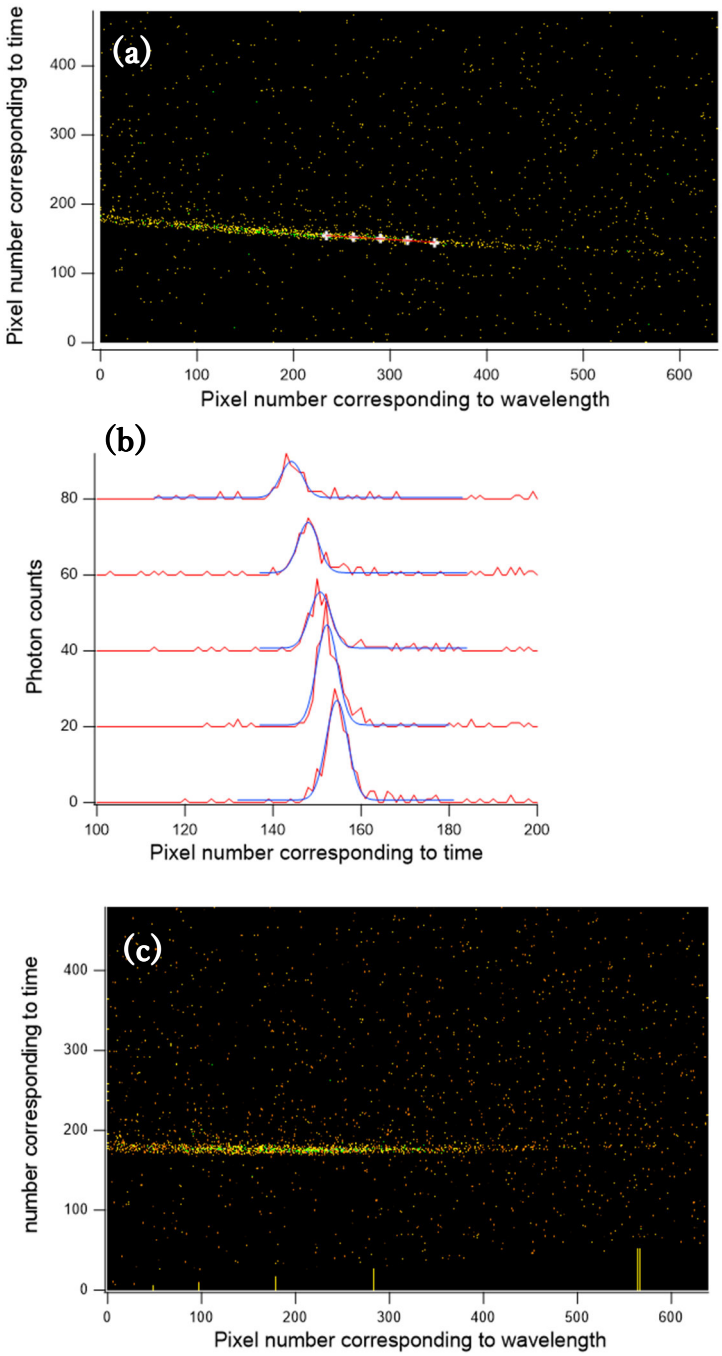

Figure 2-19 (a) A streak image of a malachite green aqueous solution measured with the cryogenic streak-camera optical system. (b) Integrated decay curves extracted from the image (a) (red solid lines), and the results of Gaussian fittings (blue solid lines). The estimated peak positions and the result of liner fitting to them are superimposed on the image (a) as white crosses and red line, respectively. (c) The obtained streak image after the correction for the distortion due to the chirp effect of the optical fiber passage.

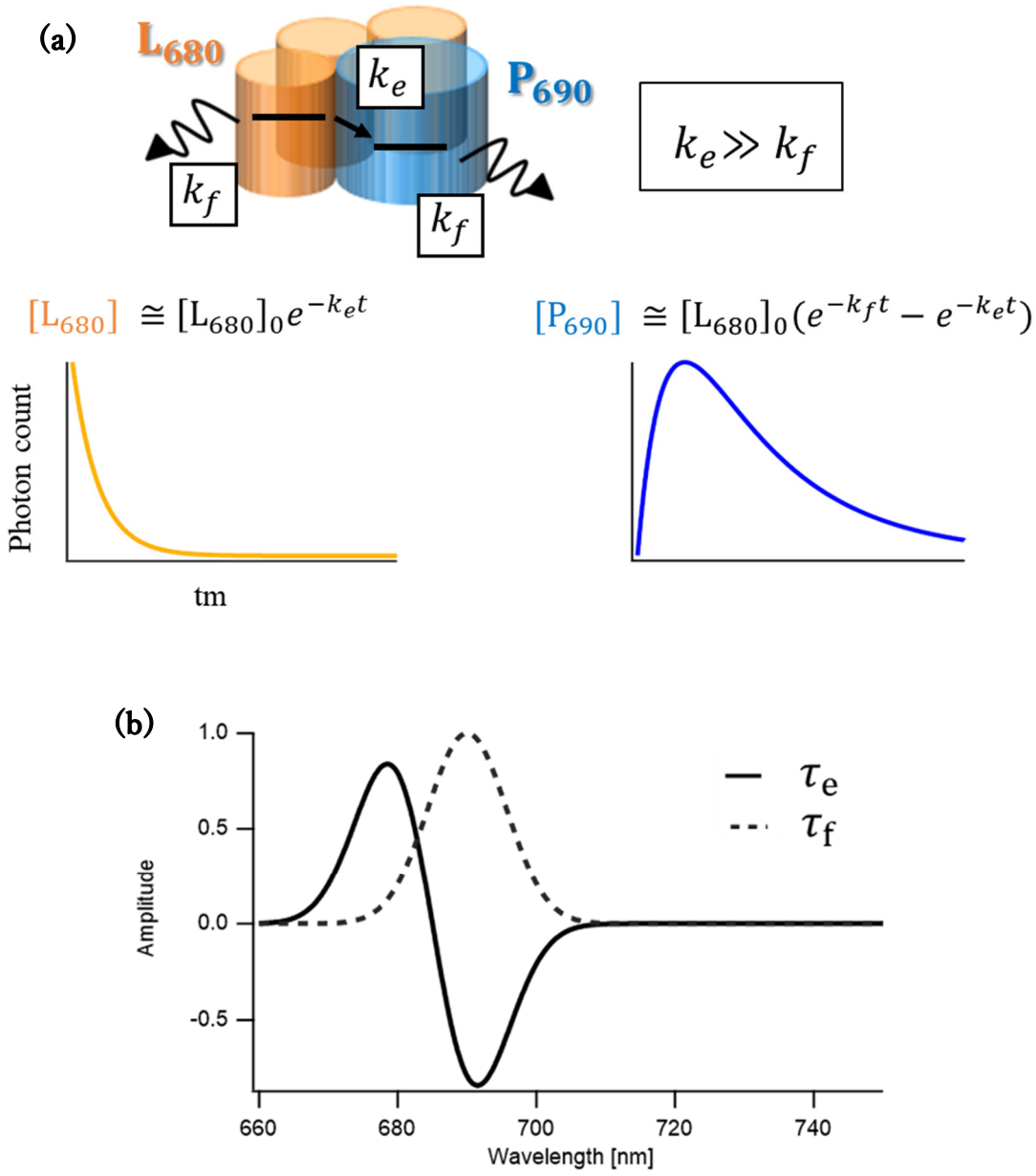

Figure 2-20 A diagram explaining the DAS analysis. (a) The simulation scheme assuming that the excitation energy of a 680-nm emitting pigment (L_{680}) is fed to a 690-nm emitting one (P_{680}) with a rate constant of k_e. The approximated population kinetics of the two pigments are depicted below. (b) Graph plotting amplitude vs. wavelength obtained by the DAS analysis with the above simulated model.

Table 2-1 A recipe of TAP medium.

TAP	**1 L**
Tris base	2.42 g
TAP salt	25 mL
Hutner trace elements	1 mL
(pH 7.0 / 100% Acetic acid)	1.05 mL
1 M KPO_4 (pH 7.0)	1 mL

TAP salt	**1 L (for 40L of TAP)**
NH_4Cl	15 g
$MgSO_4 7H_2O$	4 g
$CaCl_2 2H_2O$	2 g

TAP (NO_3) salt	**1 L**
KNO_3	71 g (or 28.35 g)
$MgSO_4 7H_2O$	4 g
$CaCl_2 2H_2O$	2 g

Hutner trace elements	**1 L**
EDTA	43.46 g
$ZnSO_4 7H_2O$	22.0 g
$CuSO_4 5H_2O$	1.57 g
$MnCl_2 4H_2O$	5.06 g
$CoCl_2 6H_2O$	1.61 g
$(NH_4)_6Mo_7O_{24} 4H_2O$	1.10 g
$FeSO_4 7H_20$	4.99 g
H_3BO_3 (Boric Acid)	11.4 g
(pH 6.7 / 10 M KOH)	
Incubate at r.t. with mixing for at least 1 month (then Store at 4 °C)	

1 M KPO_4 pH 7.0	**1 L**
1 M KH_2PO_4 (pH 4.0)	ratio 1
1 M K_2HPO_4 (pH 9.5)	ratio 4
Store at 4°C	

Table 2-2 A recipe of HSM medium.

HSM	**1 L**
No. 1 stock solution	10 mL
No. 2 stock solution	10 mL
Hunter trace element	1 mL

No. 1 stock solution	**1 L**
NH_4Cl	50 g
$MgSO_4 7H_2O$	2 g
$CaCl_2 2H_2O$	1 g

No. 2 stock solution	**1 L**
K_2HPO_4	144 g
KH_2PO_4	72 g

Table 2-3 Wavelengths of the emission lines (right column) of a standard neon lamp (light blue cells) and mercury lamp (light red cells) and their detected position (in pixel unit) on the CCD camera.

Pixel number of the CCD camera	Wavelength [nm]
72	435.84
394	546.07
512	585.25
596	614.31
632	626.65
672	640.23
729	659.90
826	692.95
856	703.24

Table 2-4 Wavelengths of the emission lines (right column) of a standard neon lamp (light red cells) and their detected position (in pixel unit) on the streak camera.

Pixel number of the streak camera	Wavelength [nm]
118	640.23
171	659.90
256	692.95
282	703.24

Chapter III Experiment with the FLIM System

3-1 Purpose of This Experiment

We newly developed the cryogenic FLIM system which simultaneously provides us fluorescence spectrum and lifetime at every pixel of a fluorescence image (see section 2-6). As I mentioned in section 1-5, a fluorescence measurement of a chloroplast at low temperature allows us to identify fluorescent peaks contributed from PSII, PSI and LHCII, respectively. In addition, we can estimate net FQY of pigment proteins of interest by means of a fluorescence lifetime measurement. We conducted an imaging of several *Chlamydomonas* cells by using the developed cryogenic FLIM system to reveal a location and function of the free-LHCII upon the state transitions.

3-2 Intracellular Segregation of PSII and PSI

Figure 3-1 (a) shows typical confocal fluorescence images of a *Chlamydomonas* cell in state2 detected by the polychromator + CCD camera. The image indicates that the cell has a cup shaped chloroplast. This characteristic shape is typical for *Chlamydomonas* (see Fig. 2-1). In our cryogenic FLIM system, we can obtain a fluorescence spectrum at every pixel. A typical example of the spectrum is shown as black dots in Fig. 3-1 (b). To decompose the fluorescence signal in each pixel into components contributed from LHCII, PSII, and PSI, we conducted a global Gaussian-decomposition analysis including spectra of isolated PSII-LHCII and PSI. Details of the procedure for determining the peak positions and the width of the Gaussian-functions are described below.

1) we calculated the averaged fluorescence spectra for all cells in state1 or state2.
2) The calculated averaged spectra of state1, state2, and the spectra of isolated PSII-LHCII and PSI purified from *Chlamydomonas* (kindly given by Minagawa lab., see section 2-2) were plotted against wavenumber (Fig. 3-2).
3) The above obtained spectra were globally fitted to sum of five Gaussian functions (orange, blue, red, and black Gaussian in Fig. 3-1 and Fig. 3-2) as expressed in Eq 3-1. The PSI component band (red Gaussian in Fig. 3-2) and the PSII-LHCII component bands (orange and blue Gaussian in Fig. 3-2) were not included for the fitting of the purified PSII-LHCII (Fig. 3-2 (c)) and of the isolated PSI (Fig. 3-2 (d)), respectively. We fitted these spectra with

a constraint that the peak position and the width of each Gaussian band have the same value for the four spectra, except for the PSII band at around 690 nm. We had to set the parameters of the band at around 690 nm free to vary to ensure a sufficient fitting quality. This indicates the sensitivity of the 690-nm band to the environment and the history of the treatment [98]. The obtained peak wavelength and FWHM of each Gaussian component are listed in Table 3-1.

4) We conducted the fitting of the spectra at all the pixels in the typical fluorescence images to sum of five Gaussian functions, where only the amplitudes of the functions were allowed to vary whereas the peak positions and widths were fixed to the values determined by the above global fitting.
5) Fluorescence images were reconstructed with areas of the obtained Gaussian functions at every pixel of the typical fluorescence image. LHCII, PSII, and PSI images in Fig. 3-1 (a) are regenerated from the areas of orange, blue, and red Gaussian functions in Fig. 3-1 (b), respectively.

$$F(x) = y_0 + \sum_{i=1}^{5} A_i \cdot e^{-\left(\frac{x-x_i}{width_i}\right)^2}, \qquad \text{(Equation } 3-1\text{)}$$

where y_0 is the background, A_i, x_i, and $width_i$ are the amplitude, peak position, and width of the *i*-th Gaussian function, respectively. In this experiment, we measured 10 cells in state1 and state2, respectively, Fluorescence spectra were averaged over all the 10 cells in each state in the procedure 1). Note that the global fitting for state1 cells and state2 cells used different parameters (values of the peak position and width at around 690 nm derived by the global fitting are different depending on the states, see the above procedure 3)). The slight difference in the parameters of the 690 nm reflect the high susceptibility of this band to slight perturbations on the protein environment, which has been frequently reported so far [98]. Here we assign the 680-nm band to the major antenna complex, LHCII, though this band may contain contributions from other minor antenna components such as CP26 and CP29. The two Gaussian functions around 685 nm and 690 nm were assigned to PSII core complex, and the 710-nm band was attributed to PSI. Since the broad 730 nm band (black Gaussian in Fig. 3-1 and Fig. 3-2) was contained in both the isolated PSII and PSI, it might be contributed from the vibronic band and was not assigned to any specific pigment-protein complex. These Gaussian functions assigned to each pigment protein were roughly consistent with the species-associated spectra (SAS), that are the presumed spectra of the

emitting species estimated by time-resolved measurements and the subsequent target analysis for *Chlamydomonas* sample reported in previous reports [31, 32]. After the fitting of all the pixels of the image, the spectra of 30 pixels were randomly extracted in order to confirm the validity of the fitting (Fig. 3-3). Then, we reconstructed the fluorescence images contributed from LHCII, PSII, and PSI components as shown in Fig. 3-1 (a).

The PSII / PSI image in Fig. 3-1 (a) shows the PSII/PSI ratio map obtained by dividing the signals in each pixel of the PSII image (PSII in Fig. 3-1 (a)) by that of the corresponding pixel of the PSI image (PSI in Fig. 3-1 (a)). Regions with very low signal intensities were blocked out to eliminate noisy signals due to division by tiny values. The ratio map showed intracellular inhomogeneities of the PSII and PSI fluorescence. The observed inhomogeneity in the PSII/PSI ratio reflects the non-uniform distributions of PSs within the *Chlamydomonas* chloroplast as well as the non-uniformities in the FQY and in the local antenna sizes of PSs. Although the thylakoid membranes in the chloroplasts of *Chlamydomonas* cells do not well develop grana-structures like those of higher plants, the two PSs have been known to show a certain degree of segregation with a characteristic size of ca. 300 nm [44]. Moreover, Cryo-ET method indicated the distributions of PSs are clearly segregated between stacked and unstacked thylakoid membrane regions, respectively [44]. As I certified in section 2-10, our cryogenic system achieved ca. 300 nm spatial resolution in lateral axis. We presumed that our system has a marginal resolution to distinguish the localizations of PSs, which is the first achievement in the world to observe the inhomogeneous distributions of PSs with in vivo measurement by using an optical microscope.

If we assume that the FQY of PSII and PSI are constant over the entire region of the chloroplast, the above ratio map from the fluorescence intensity is proportional to the local concentration ratio of PSII with respect to PSI. Indeed, it has been reported that the fluorescence lifetime of PSII and PSI were almost constant regardless of the binding of LHCII [31,32]. On the other hand, the FQY of LHCII changes depending on whether it is bound or dissociated from the two PSs. Thus, the simultaneous detection of the fluorescence decay curves at 680 nm at each pixel provides fruitful information on both the local concentration and the state of LHCII.

3-3 Comparing Spectra in PSII-rich and PSI-rich Regions

As I mentioned in section 1-4, in a current state-transition model, most LHCII is assumed to attach to PSII and fed their excitation energy to PSII in state1, whereas a preferential

PSII excitation induces LHCII to detach from PSII and move to PSI for maintaining excitation balance between PSs. I simply summarize this model in Fig. 3-5 (b). Since, as I explained in the previous section, our microscope measurement can spatially distinguish PSII-abundant and PSI-abundant regions, the obtained fluorescence spectra in principle should reflect the variation in LHCII local concentration.

To assess the differences in spectral characteristics between the PSII-enriched or PSI-enriched regions, we identified two characteristic intracellular regions with the PSII-enriched and PSI-enriched tendencies. To do this, we extracted intracellular domains with remarkably large/small values of the PSII/PSI ratio for each single cell. About 50 pixels having the highest and the lowest PSII/PSI ratios were picked up from the image of each cell. The former and the latter regions are assigned to the PSII-rich and PSI-rich regions, respectively. In the case of the cell shown in Fig. 3-1, the PSII-rich and PSI-rich regions satisfy PSII/PSI > 0.315 and PSII/PSI < 0.235, respectively. Figure 3-4 shows fluorescence images of all measured cells and the extracted two intracellular regions.

We averaged over all the fluorescence spectra obtained from each region assigned to either PSII-rich or PSI-rich in state1, state2, and *stt7* mutant (black dots in Fig. 3-5 (a)). The extracted and averaged spectra were re-fitted with the sum of five Gaussian functions as introduced in Eq 3-1. The fitting results are superimposed in the same manner as that in Fig. 3-2. In this fitting, the parameters of the Gaussian function at around 690 nm were necessary to be set free to vary to ensure a sufficient fitting quality. Not surprisingly, the spectra in the PSII-rich region have relatively stronger peak at around 685 nm mainly contributed from PSII, whereas those in the PSI-rich region have enhanced fluorescence band at around 710 nm mainly contributed from PSI. The four averaged spectra in state1 and state2 of the wt-cells in Fig. 3-5 (a) correspond to those in the four divided sections in the illustration of the state-transition model in Fig. 3-5 (b). We assumed that the fluorescence intensity of LHCII and the local concentration of LHCII are in a linear relationship, and we compared the changes in the relative intensity of LHCII within these regions. To do this, we calculated the ratio of the fluorescence band assigned to LHCII with respect to whole fluorescence spectra by the following equation,

$$\text{Occupancy of LHCII } (O_{LHCII})\ [\%] = \frac{A_1 \cdot width_1}{\sum_{i=1}^{5} A_i \cdot width_i}, \qquad \text{(Equation } 3-2)$$

where the subscripted numbers have the same meaning as Eq 3-1 (1 represents the LHCII component. The calculated O_{LHCII} are also described in Fig. 3-5.

As you see, there is no significant change in O_{LHCII} between PSII-rich and PSI-rich in each state. In addition, the spectra of *stt7* mutant also do not show effective change in O_{LHCII}. There are four possible reasons for these unexpected observations:

1) The FQY of LHCII differs depending on whether it is bound to PSII or PSI. Therefore, the local concentration of LHCII is not reflected on the local fluorescence intensity.
2) The fluorescence of LHCII fraction involved in the migration upon the state transitions is extremely small.
3) PSII-rich and PSI-rich regions do not exactly correspond to the two abundant regions due to the limited spatial resolution.
4) In the first place, LHCII does not move at all upon the state transitions.

Regarding 1), we analyzed the fluorescence lifetime at every pixel of the same cell to evaluate the heterogeneity in the FQY of LHCII depending on the intracellular locality (see section 3-4). Regarding 2), since LHCII feeds most of the absorbed energy to PSs, the number of fluorescence photons from LHCII may be relatively small compared to other pigment proteins. As I mentioned in section 1-3, *Chlamydomonas* contains a large LHCII system consisting of S-, M-, N-LHCII, and monomeric CP29 and CP26. Only a part of LHCII among these is assumed mobile upon the state transitions. When most of the Gaussian function assigned to LHCII is dominated by fluorescence from PSII, PSI, or LHCII that is not involved in the migration, the shuttle of LHCII is less reflected in the change in the Gaussian function. Regarding 3), as I mentioned in the previous section, the spatial resolution of our microscope is barely enough to spatially distinguish between PSI and PSI. Although the fluorescence spectra of PSII-rich and PSI-rich regions clearly show the difference in the relative intensities of the PSII band and PSI band, the PSI/PSII-rich domain does not mean that it is composed of 100% PSII/PSI but contains some amount of PSII/PSI mixed. Therefore, the difference in the relative LHCI fluorescence intensity is blurred by the mixed PSs. To eliminate this problem, we proceeded with the introduction of the STED technique that improves the spatial resolution of an optical microscope (see Chapter V).

3-4 FLIM Measurement

The cryogenic FLIM system provides fluorescence spectrum and lifetime simultaneously at every pixel of a fluorescence image. The analysis of the obtained spectra is described in section 3-4. Here, I will introduce the analysis procedure of the obtained fluorescence

lifetimes.

Figure 3-6 shows the fluorescence image detected by the TCSPC module of the same cell as that shown in Fig. 3-1. Each pixel contains accumulated photon counts. we installed the bandpass filter transmitted at around 680 nm in front of the APD. The transmission spectrum of the bandpass filter is superimposed as a green dashed line in Fig. 3-2 (a). Note that the filter transmits not only the fluorescence from LHCII, but also a part of those from PSs. The black dots in Fig. 3-6 (c) represent a typical fluorescence decay curve obtained at a certain pixel in Fig. 3-6 (a). In order to quantify the averaged fluorescence lifetime of each local region, the decay curve at each pixel was fitted to sum of four exponential decay models convolved with IRF, where only the amplitude of each exponential function was allowed to vary whereas the lifetime was fixed (τ_1=3.0 ps, τ_2=64 ps, τ_3=190 ps, τ_4=1.1 ns, in Fig. 3-6 (c)). These fixed lifetime values were determined by a global decay-decomposition analysis as described in Fig. 3-7. Detail of the analysis is given in caption of Fig. 3-7. The fittings to four exponential decay models as shown in Fig. 3-6 (c) and Fig. 3-7 were conducted using Eq 2-13 d in Chapter II. Surprisingly, we found the extremely faster component, represented as τ_1 (3 ps), than the IRF (42.6 ps, see section 2-12). The validity of the determination of the amplitude with the lifetime component faster than the IRF is described in section 3-8. Note that the parameters obtained through the fitting vary depending on the initial guess value of the start time of the fluorescence decay curve (t_0 in Eq 2-13 d). This has a significant effect on the determination of parameters with τ_1 (3 ps) component with a very fast lifetime. Although it is difficult to estimate an accurate initial value of t_0, the uncertainty in t_0 value did not greatly affect the final estimation of τ_{ave}. Therefore, an apparently plausible value was manually determined and set as the initial value of t_0. After the fitting of all the pixels of a fluorescence image was completed, the fluorescence decay curves of 20 pixels were randomly extracted in order to confirm the validity of the fitting (Fig. 3-8). The average lifetime (τ_{ave}) was calculated for all pixels using the following equation,

$$\tau_{\mathrm{ave}} = \frac{\sum_i^N a_i \tau_i}{\sum_i^N a_i} . \qquad \text{(Equation } 3-3\text{)}$$

Here, a_i is the amplitude of the i-th decay component. Figure 3-6 (b) shows the map of τ_{ave}. Regions with very low signals were blocked out in Fig. 3-6 (b) as the PSII / PSI ratio map in Fig. 3-1 (a).

To evaluate the difference in the FQY of LHCII between the PSI-rich and PSII-rich regions, we plotted the obtained τ_{ave} of the LHCII component at each pixel against the PSII/PSI

ratio calculated by the method introduced in section 3-2 at the same pixel. The plots for all measured cells are represented in Fig. 3-9 (Panels (a), (b), and (c) belong to state1, state2, and stt7-mutatnt groups). Here, vertical and horizontal axes indicate the calculated τ_{ave} and PSII/PSI ratio at each pixel, respectively. Each single pixel in a fluorescence image gives a dot in Fig. 3-9. It should be noted here that the PSII/PSI ratio were calculated using the spectral areas rather than heights. Under simple assumption that the fluorescence decay curve detected by the TCSPC module mainly reflects the fluorescence signals of LHCII component, the calculated τ_{ave} is proportional to the FQY of LHCII. A positive correlation between τ_{ave} and PSII/PSI ratio in Fig. 3-9 suggests that the FQY of LHCII co-localized with PSII tends to be higher than those co-localized with PSI, and vice versa. The fitting to straight lines is shown as black solid lines in Fig. 3-9. To evaluate the correlation quantitatively, we estimated the Pearson's correlation coefficient (R) between τ_{ave} and the PSII / PSI ratio according to the following equation,

$$R = \frac{\sum_{i=1}^{n}(x_i - \bar{x})(y_i - \bar{y})}{\sqrt{\sum_{i=0}^{n}(x_i - \bar{x})^2}\sqrt{\sum_{i=0}^{n}(y_i - \bar{y})^2}}, \qquad \text{(Equation } 3-4\text{)}$$

where x_i and y_i represent the value of τ_{ave} and the PSII / PSI ratio of each dot in Fig. 3-9, respectively. R has a value between –1 and +1. A value of R near +1 suggests a positive correlation between the two quantities, while that near -1 suggests a negative correlation. The calculated R of each cell is also given in Fig. 3-9. The several tendencies can be seen in Fig. 3-9, as described below.

The values of τ_{ave} in state2 tends to be lower than those in state1. This tendency seems to be attributed to the decreased contribution of the PSII fluorescent rather than the difference in FQY of LHCII component. Comparing the fluorescence spectra of state1 and stae2 in Fig. 3-2 (a, b) and Fig. 3-5 (a), the redder Gaussian component at around 14500 cm^{-1} of the two PSII components is larger in state1 than in state2. The previous study on isolated PSII particles have suggested that CP47 component as shown in Fig. 1-7 (a) mainly contributes to 695 nm fluorescence band [99]. Chls in CP 47 are not so efficient in excitation energy transfer to the PSII RC at 80 K as compared to those in LHCII?? the other PSII antenna?? due to the lower excitation energy of its terminal emitter, leading to its relatively slower fluorescence lifetime. Since the bandpass filter used in the present study allows transmission of the short wavelength side of the CP47 fluorescence with the longer-lifetime, more CP47 fluorescence were detected in the state1 cells, and the τ_{ave} also became slower in state1. I will discuss later in section 3-6 the trial to derive the pure LHCII kinetics by subtracting the slower decay components assigned to the PSs.

Since *stt7* mutant is unable to turn to state2, the state1-induced wild-type and *stt7* cells were expected to show similar behaviors. However, there was a large variation in the values of τ_{ave} in state1 and *stt7* mutant cells. Regarding to this tendency, we do not have any plausible explanation at present. Since in the experiments for state1 and *stt7* mutant cells, the signal to noise (SN) ratio of the detected fluorescent signal was not so high due to some uncontrollable factors such as the poor transparency of the frozen suspension, the low precision fitting obscured the estimation of accurate τ_{ave}.

The values of R are slightly higher in state2 cells. Since a clear increase in R has not been obtained, we cannot continue a deeper discussion. As I will introduce in section 3-5, the specific regions with significantly higher fluorescence signals from PSI and faster fluorescent lifetime at around 680 nm have been found in some cells in state2. These specific intracellular regions were presumably reflected on the slightly higher values of R in state2.

In any case, no systematic difference in FQY of LHCII component between the PSI-rich and PSII-rich regions was found in our analysis. Although our measurement and analysis were conducted under the simple assumption that the fluorescence decay curve detected by the TCSPC module mainly reflects the fluorescence signals of LHCII component, effective transmission spectrum of the bandpass filter indicates that the contribution of fluorescent signals from PSs components are not negligible. It is necessary to adopt a bandpass filter with a shorter transmission wavelength width in order to ensure the extraction of the fluorescence signal exclusively assigned to LHCII. This will enable a discussion based on the accurate FQY of LHCII component.

3-5 Specific Sub-Cellular Regions with High PSI in State2 Cell

Figure 3-10 (a, b) represent the PSII/PSI ratio map obtained as explained in Section 3-2. The cells shown in (a, b) are cell_12 and cell_15, respectively. Both cells were induced to state2. Green squares in Fig. 3-10 (a, b) highlight the areas where the fluorescent signal from the PSI is relatively high. These specific regions tended to be located in the basal regions surrounding the pyrenoids within the cells. Figure 3-10 (c, d) show τ_{ave} images of the same cells as those in Fig. 3-10 (a, b), respectively. Note that the τ_{ave} in these specific areas with high fluorescence intensity of PSI exhibit lower τ_{ave} values. Averaged and normalized fluorescence spectra and decay curves over the whole cells and within the green square areas are shown as red and green

solid lines in Fig. 3-10 (e - h), respectively. Fig. 3-10 (e, g) reflect the signals in cell_12 while panels (f, h) indicate signals from cell_15. The spectra in Fig. 3-10 (e, f) are normalized at PSII peak with 682 nm. Obviously, the green solid lines in fluorescence spectra have a stronger PSI peak and those in fluorescence decay curves exhibit clearly faster fluorescence lifetime. The black solid lines in Fig. 3-10 (e, f) represent the difference spectra between the normalized fluorescence spectra averaged over the whole cell and those over the specific areas (green lines minus red lines in Fig. 3-10 (e, f)). Surprisingly, a new peak at around 676 nm is found in green lines. This peak is mainly contributed from LHCII. In the fluorescence decay curves, we did not perform assignments of lifetime components to the specific pigment-protein complexes due to the large uncertainty in the obtained parameters depending on the initial value of t_0. There will be two possible reasons for the shortened lifetime in the specific areas, as described below.

1) Since the fluorescence lifetime of PSI is faster than that of PSII in this spectral region, the fluorescence decay curve is shorter in the area where the contribution from PSI is larger.
2) The FQYs of LHCII in these specific areas are relatively low.

As described above. the adopted bandpass filter transmits not only the LHCII fluorescence but also those from PSII and PSI. Therefore, the differences in the fluorescence lifetimes between PSII and PSI should also be reflected in the detected fluorescence decay curves. Actually, some previous papers using lifetime measurements [100, 101] or theoretical calculations [13, 41, 42] for purified pigment proteins have suggested that PSI exhibits relatively shorter fluorescence lifetime than PSII. However, in our in vivo measurement, there is no significant correlation between the τ_{ave} and the heterogeneity of PSs (see Fig. 3-9), indicating an incompatibility of the possibility 1). Moreover, the possibility 1) cannot explain the appearance of the LHCII peak at 676 nm in the specific area. On the other hand, some previous papers have suggested that the free-LHCII, which associates neither PSII nor PSI, exhibits a shorter fluorescence lifetime probably due to its aggregation [31, 32, 33, 34]. The aggregation-induced LHCII quenching has been discussed in relation to the non-photochemical quenching (NPQ) which plays a role to inhibit the generation of reactive oxygen species (ROS) [57, 58, 59]. In addition, the rise in the peak at 676 nm indicates that the local concentration of short-lived components increases, which is consistent with the aggregation of free-LHCII. At present, it is assumed that induction of state2 causes LHCII aggregation and subsequent NPQ in a part of PSI peripheral region (stroma lamella) in lobe [102]. However, these behaviors were observed for only two cells out of ten induced to

state2, and the reproductivity is insufficient to proceed the deeper discussion

3-6 Comparing Lifetime in PSII-rich and PSI-rich Regions

Here, we evaluate the variation in fluorescence decay curves between the PSI-rich and PSII-rich subdomains. As I explained in section 3-3, we identified two characteristic intracellular regions, PSII-rich, PSI-rich, where remarkably large/small values of the PSII / PSI ratio were obtained. About 50 pixels having the highest and the lowest PSII/PSI ratios were picked up from the image of each cell. The former and the latter regions are assigned to the PSII-rich and PSI-rich regions, respectively. We averaged the fluorescence decay curves obtained from each region of the state1-, state2-induced cells, and *stt7* mutant cells. Then, I obtained 6 decay curves distinguished as state1/2/*stt7*-PSII-rich, state1/2/*stt7*-PSI-rich (black dots in Fig. 3-11). All decay curves are normalized to unity. These 6 decay curves were re-fitted to the four exponential decay models convolved with the IRF. The fitting curves and assigned four exponential components are superimposed as the red lines and the filled curves, respectively. As I mentioned in section 3-4, these fittings and assignments for four exponential decays, especially determination for τ_1 (curves filled with black in Fig. 3-11), have large uncertainties depending on the initial value of t_0.

As you see, decay curves in state1 and *stt7* mutant exhibit clearly longer lifetime than those in state2. The assigned exponential decays indicate that this feature is attributed to the increase in the amplitude of the time constant with 150 ~ 170 ps (curves filled with pale gray in Fig. 3-11) in state1 and *stt7* mutant. As I mentioned in section 3-5, PSII involves relatively longer lifetime component assigned to CP47, and increase in signals of this component mainly contributes to the enhanced slower component.

By applying the Förster resonance energy-transfer theory [103] to the recently determined structure of the PSII-LHCII supercomplex, the time constant of the excitation energy transfer from LHCII to PSII was estimated to be less than 100 ps [42]. Under a simple assumption that the signals from LHCII are concisely assigned to two faster exponential decay components (time constants with 3~5 ps and 50 ~100 ps corresponding to functions fulfilled with black and thick-gray in Fig. 3-11, respectively), we estimated the ratio of local concentration of LHCII in each PS-enriched region. In general, the obtained amplitude in the fitting to the exponential decay model reflects the concentration of a pigment species of interest. We calculated the ratio occupied

with the concentration of LHCII among those of all pigment proteins by the following equation,

$$\text{Occupancy of LHCII } (O_{LHCII})\ [\%] = \frac{A_1 + A_2}{\sum_{i=1}^{4} A_i}, \qquad \text{(Equation } 3-5)$$

where A_i represents the estimated amplitude of the *i*-th exponential-decay component. A_1 and A_2 indicates the amplitudes of time constants with 3 ~ 5 ps and 50 ~ 100 ps, respectively. The calculated O_{LHCII} are also given in Fig. 3-11. As you see, O_{LHCII} in the PSII-rich region exhibit slightly higher value compared with that in the PSI-rich region in state1, whereas in state2, there is no significant difference between those values. It simply suggests that a part of LHCII moves from peripheral PSII to PSI upon the state transitions. However, we cannot see the reproductivity in *stt7* mutant which forced to be fixed to state1 due to deficiency of STT7 kinase. The value of O_{LHCII} is highly susceptible to A_1 whose precise determination is difficult due to the uncertainty of the fitting. This unstable determination of A_1 obfuscate our evaluation on the local concentration of LHCII. At present, we cannot clearly distinguish signals from LHCII component among all pigment proteins by means of our cryogenic FLIM system. To overcome this problem, we have attempted to identify a component with a certain lifetime constant and assign its spectral feature using a novel cryogenic optical microscope combined with a streak camera (see Chapter IV).

3-7 Two-Dimensional Autocorrelation

Some previous papers have suggested that the state transitions cause a dynamic change in the ultrastructure of the thylakoid membrane and accompanies variations in the size of the stacked membrane region where PSII is abundant [30, 74, 102]. As described in section 3-2, the cryogenic optical microscope system allows us to roughly distinguish the stacked and unstacked membrane regions in terms of PSII/PSI fluorescence intensity ratios. Here, we discuss changes in the size of stacked membrane region upon the state transitions by applying two-dimensional autocorrelation allowing us to estimate the width of the repeating pattern of the PSII/PSI intensity ratio.

A 2-dimensional autocorrelation of a quantity I is given by,

$$G(\Delta x, \Delta y) = \frac{< I(x,y) \times I(x+\Delta x, y+\Delta y) >}{< I(x,y)^2 >}, \qquad \text{(Equation } 3-5)$$

where $I(x,y)$ represents the target quantity depending on the spatial coordinates x and y, Δx and Δy indicates the shift in the x-ais and y-axis, respectively. An autocorrelation function

defined above gives a rough estimate of the characteristic domain size in which the quantity I maintains the similar value. We produced a 2-D correlogram image ($G(\Delta x, \Delta y)$) indicating the repeating pattern of the PSII / PSI intensity ratio by applying the Eq 3-5 to the PSII / PSI ratio map described in section 3-2. Figure 3-12 (a) shows the calculated 2-D correlogram image of cell_12. The horizontal and vertical axes represent the shift in x-axis (ω_1) and y-axis (ω_2), respectively. A circular peak emerges within ± 1 μm around the origin of the coordinate. We interpreted the width of this peak as the average size of the observed PSII/PSI-rich domain. The obtained 2-D correlogram image was converted into a 1-D correlogram along the radial vector by averaging the image over the azimuthal angle. Figure 3-12 (b) shows the averaged 1-D correlograms of all the measured cells in state1 (red solid line), state2 (blue solid line), and *stt7* mutant (black line). Red, blue, and gray fills represent the standard deviation of the 1D correlograms calculated for all measured cells in state1, state2, and *stt7* mutant, respectively. As you see, the curve in state2 declined more rapidly than that of state1, implying smaller size of the stacked membrane region in cells induced to state2. However, *stt7* mutant cells forced to be fixed to state1 exhibit the most rapid decline of the 1-D correlogram. Besides, the standard deviations, indicating the variability of the 1-D correlogram, were very large. From these results, I concluded that it is difficult to evaluate the change in the size of the stacked membrane region upon the state transitions. As I described in section 3-2, our cryogenic microscope has a marginal spatial resolution to distinguish the two characteristic membrane regions. We conclude that since the actual size of the stacked membrane region is not reflected in the PSII/PSI ratio map, the analysis of 2D autocorrelation function cannot output the effective repeat pattern. To eliminate this problem, we have proceeded with the introduction of the STED technique that improves the spatial resolution of an optical microscope (see Chapter V).

3-8 Validity of Identification of a Fast Lifetime Component

In our lifetime measurement using the cryogenic FLIM system, we found a component with the lifetime ($\approx$ 3 ps) much faster than the IRF. In section 3-6, we used the amplitude of this fast lifetime component to estimate O_{LHCII} as the rough estimate for the local concentration of LHCII. To evaluate the accuracy in determining an amplitude of very rapidly decaying component by the present system, we measured a dye malachite green in aqueous solution known to have a very short fluorescence lifetime of less than 1ps [78,79]. I prepare malachite green solutions with

several different concentrations and measured their fluorescence time profiles by the system (black solid lines in Fig. 3-13 (a)). Obtained decay curves could be fitted to single Gaussian function (red solid lines in Fig. 3-13 (a)). Amplitude of the fluorescence decay of a malachite green aqueous solution estimated by the fitting is plotted against its concentration (a cross point in Fig. 3-13 (b)). the dashed line in Fig. 3-13 (b) indicates the linear approximation. From the observation, we could confirm a sufficient linearity between the concentration and the amplitude of decay curve even for a fluorescent dye having a shorter lifetime than IRF.

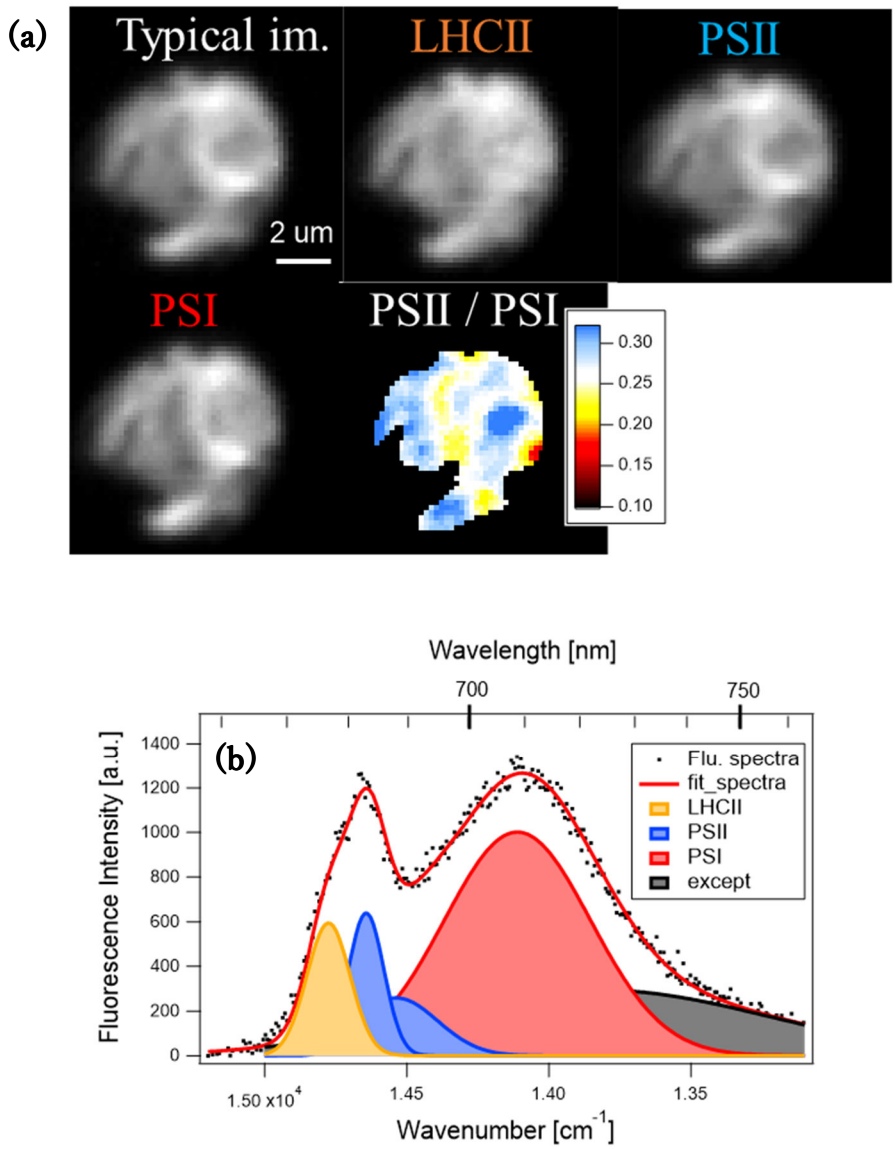

Figure 3-1 (a) A typical fluorescence images of a *Chlamydomonas* cell induced to state2 detected by the CCD camera (upper left image of (a)). The LHCII, PSII PSI images show the fluorescence images reconstructed with the LHCII, PSII, and PSI components, respectively. PSII / PSI image shows PSII/PSI ratio map. Scale bar indicates 2 μm. (b) A fluorescence spectrum (black dots) of a typical pixel in the micrograph is shown. Red solid line is the fitting curve, respectively. Gaussian peaks filled with orange, blue, and red are the component spectra of LHCII, PSII, and PSI, respectively. The Gaussian peak filled with gray is a mixed contribution from the vibronic bands of all the components and excluded from the image reconstruction.

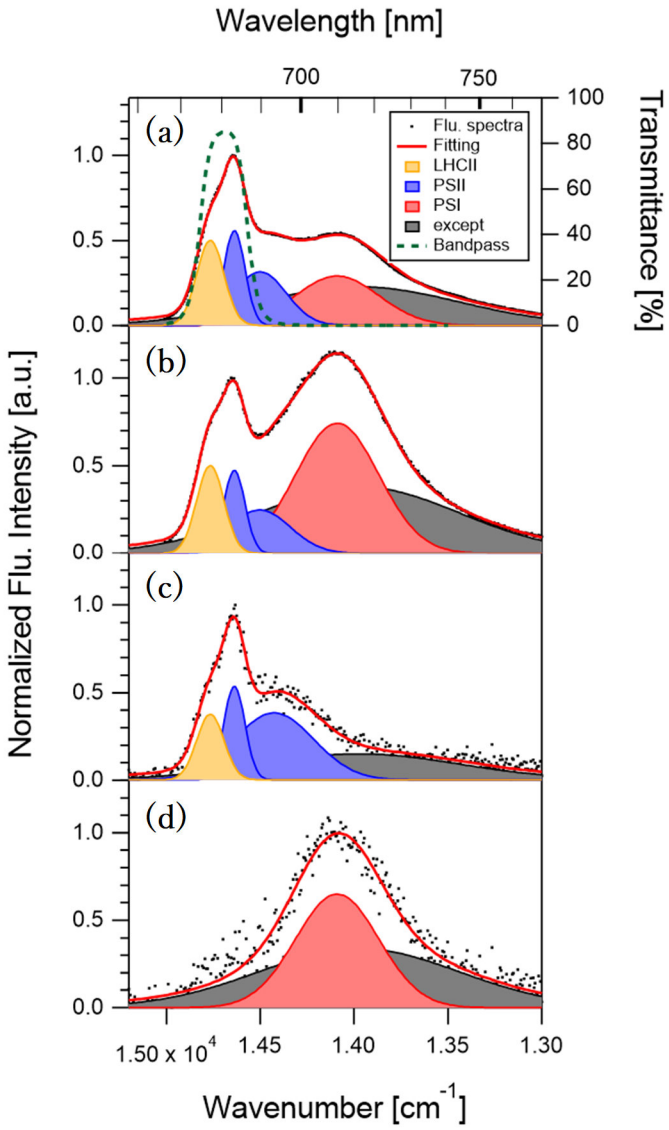

Figure 3-2 The black dots show the averaged fluorescence spectra over all measured *Chlamydomonas* cells in state1 (a), state2 (b), the fluorescence spectra of the isolated PSII-LHCII (c), and PSI (d) purified from *Chlamydomonas*. All spectra were measured with the cryogenic FLIM system. These four spectra plotted against wavenumber were globally fitted to sum of five Gaussian functions. The Gaussian function filled with orange, blue, red, and black were assigned to the component spectra of LHCII, PSII, PSI, and the vibronic bands of these pigment proteins, respectively. Green dashed line in (a) shows the transmission spectrum of the bandpass filter used in the cryogenic FLIM system. It should be noted that the bandpass filter transmitted not only the fluorescent component of LHCII but also the short wavelength side of the fluorescent components of PSII and PSI.

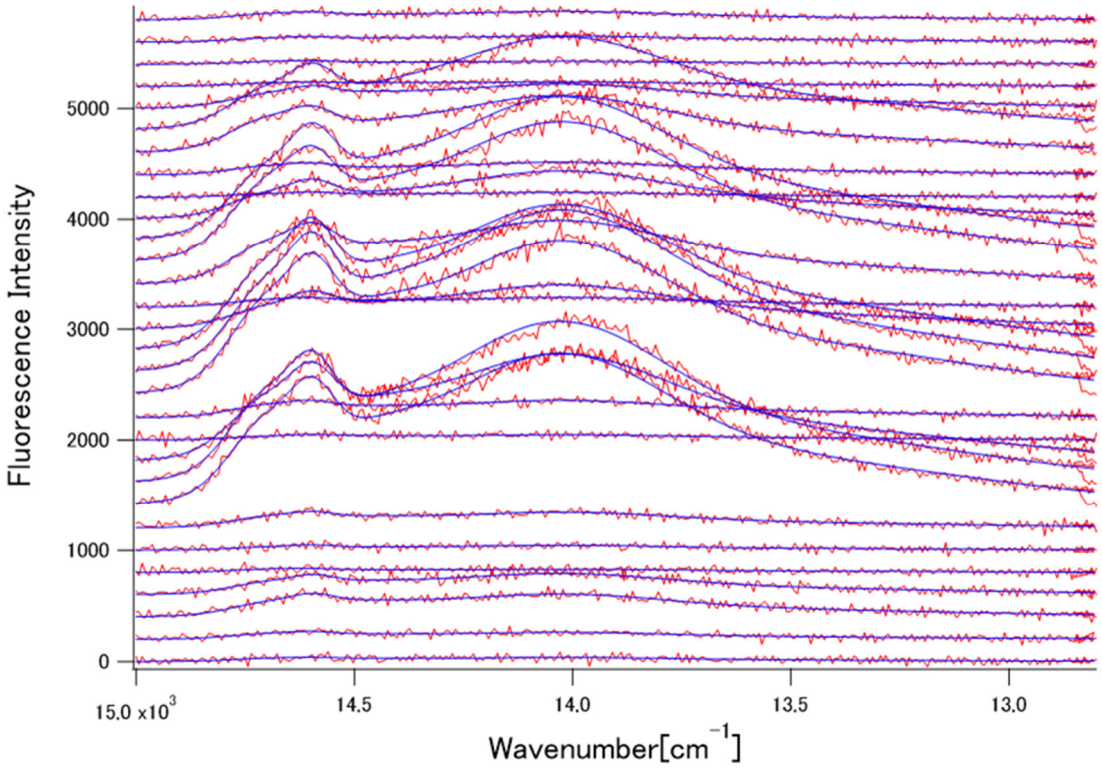

Figure 3-3 Fluorescence spectra of 30 pixels randomly selected from a cell image (red lines) and their fitting results with the sum of the five gaussian functions (blue lines).

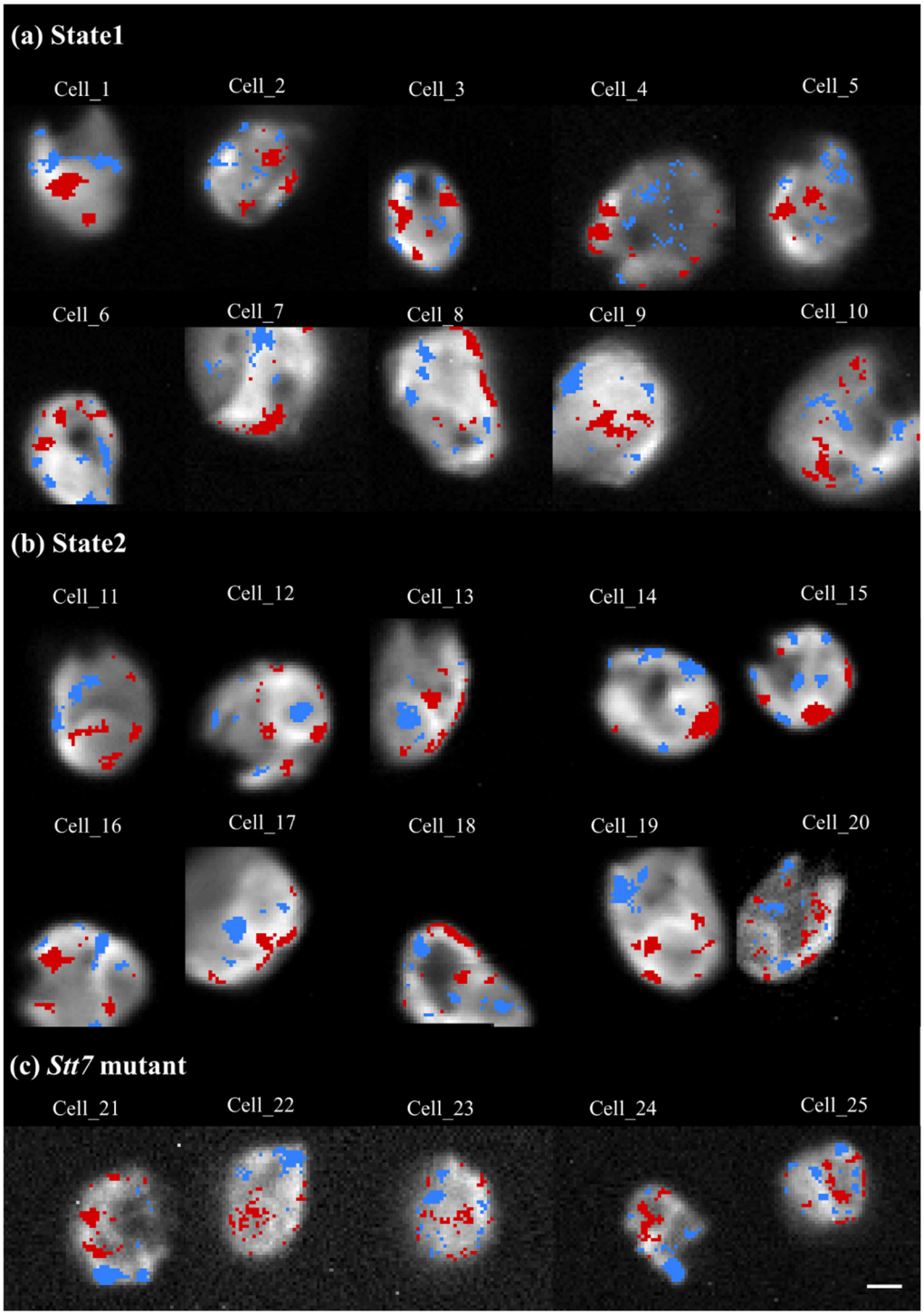

Figure 3-4 The fluorescence images of all measured cells in state1, state2, and *stt7* mutant. Identified PSII- rich and PSI-rich regions are superimposed by blue and red colored pixels, respectively. Each cell is allocated to a specific cell number indicated in each panel, which is used to specify cells in this thesis. The scale bar indicates 2 μm.

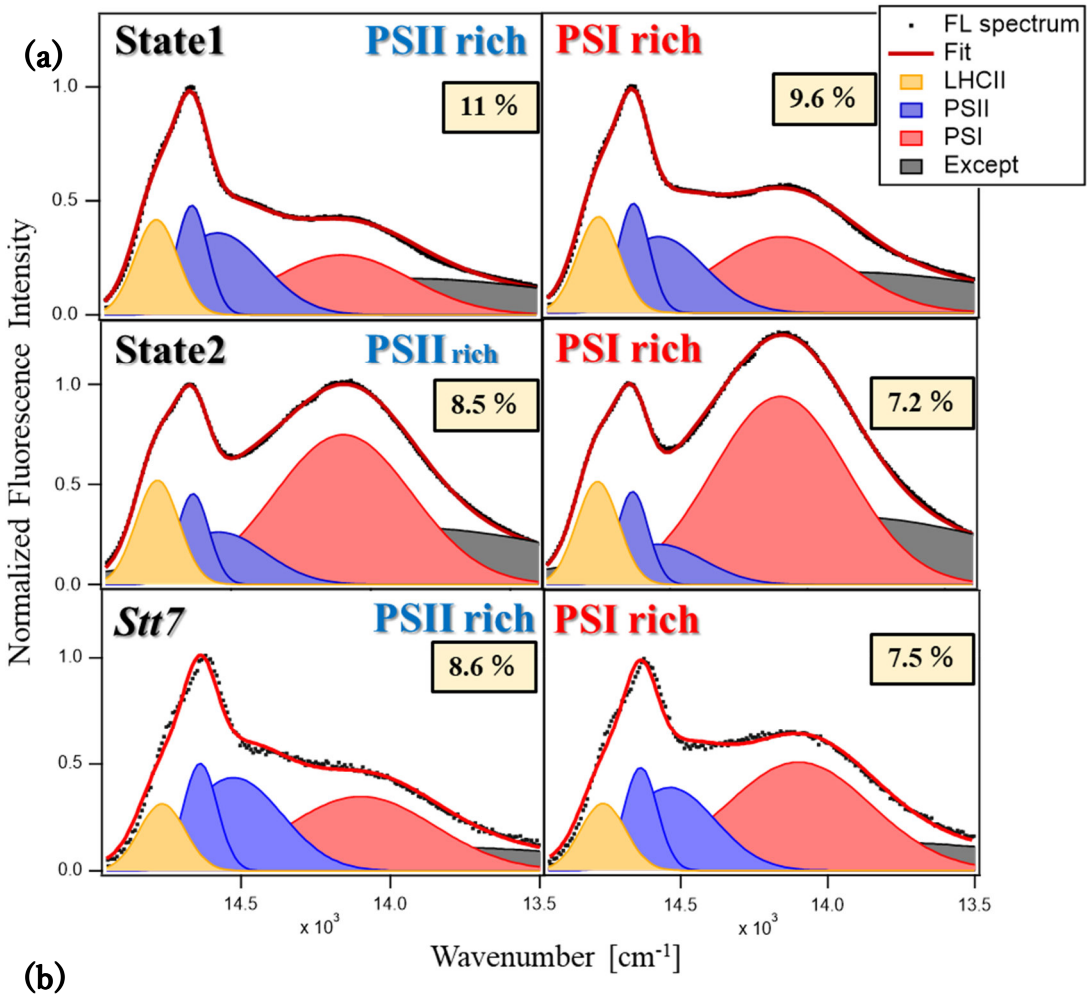

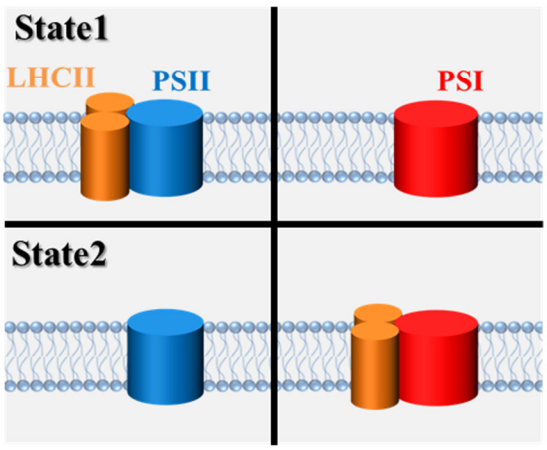

Figure 3-5 (a) Fluorescence spectra averaged over the sub-cellular regions classified into PSII-rich (left), PSI-rich (right) in the state1-induced (top), state2-induced (middle), and *stt7* (bottom) cells. The obtained spectra were re-fitted to the sum of five Gaussians. The area ratios of the LHCII component (O_{LHCII}) are shown in boxes. (b) Current state transition model assuming shuttles of LHCII as the main mechanism. The averaged spectra in (a) correspond to those expected to be observed in the divided four sections in (b).

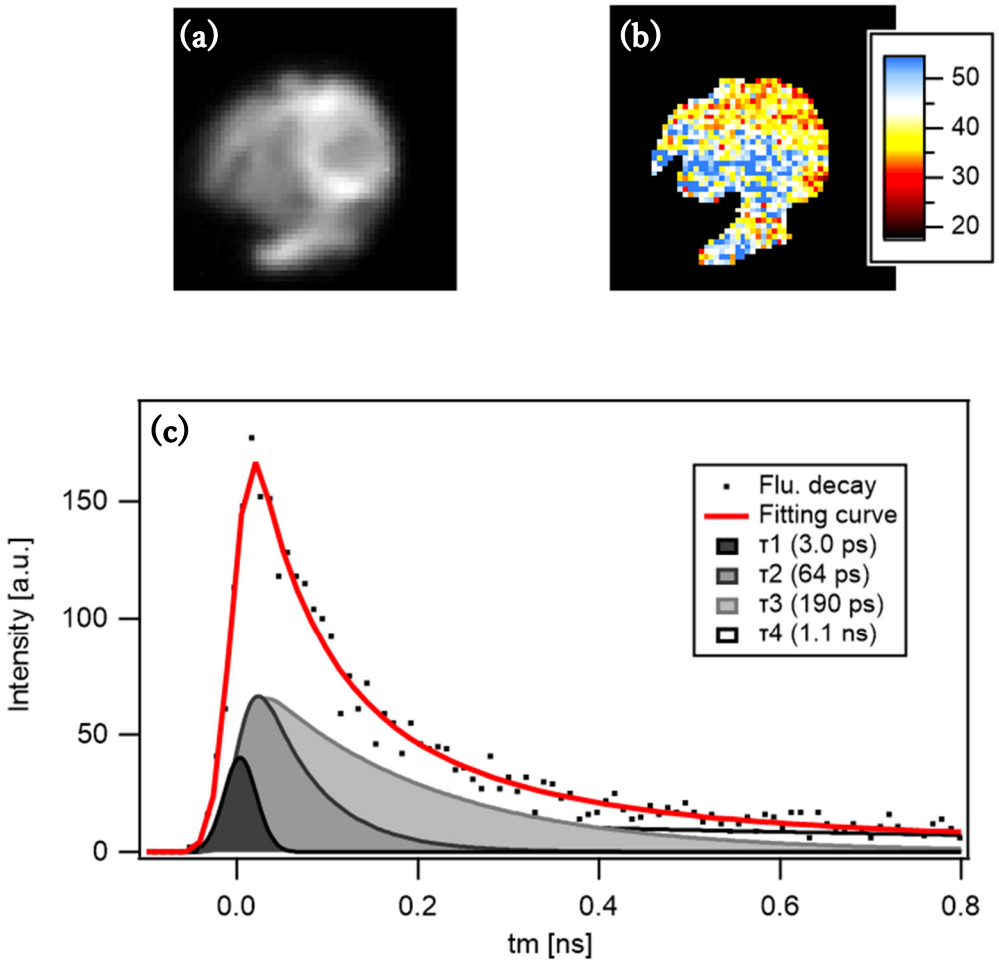

Figure 3-6 (a) The fluorescence image of the same cell as that shown in Fig. 3-1 detected by the TCSPC module. Panel (b) shows the map of the average lifetime (τ_{ave}). The values on the color scale are shown in ps units. Panel (c) shows a fluorescence decay curve (black dots) of a typical pixel in the micrograph. The red line is the fitting curve. The functions filled with black, thick-gray, pale-gray, and white show the four exponential decay components convolved with the IRF, respectively.

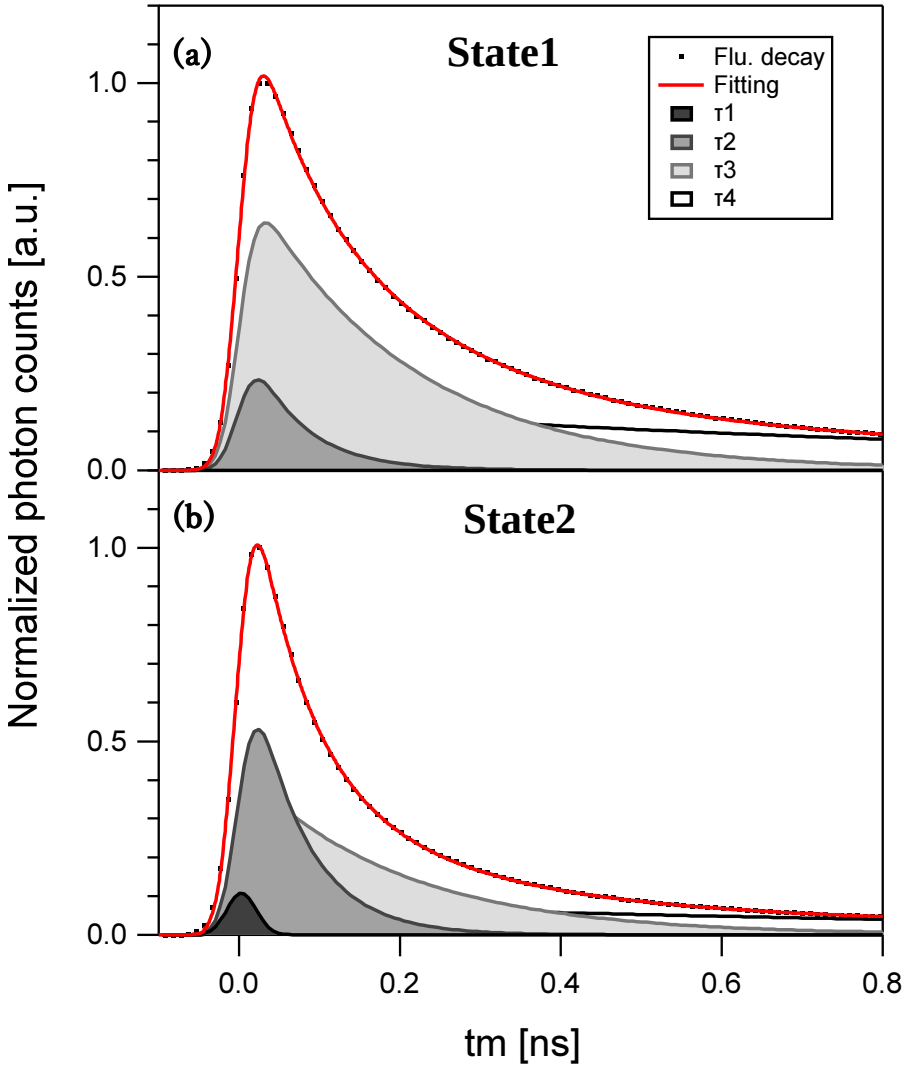

Figure 3-7 The black dots show the fluorescence decay curves averaged over all the measured cells in state1 (panel (a)) and state2 (panel (b)) detected by the TCSPC module of our cryogenic FLIM system. We performed global fitting of the data to sum of four exponential decays with the constraint to fix each time constant to take the same value for the state1 and state2. Estimated IRF as described in section 2-16 was convolved with each decay component. The red lines show the fitting curves. The functions filled with black, thick-gray, pale-gray, and white show the four exponential decay components with time constants of τ_1=3.0 ps, τ_2=64 ps, τ_3=190 ps, and τ_4=1.1 ns, respectively.

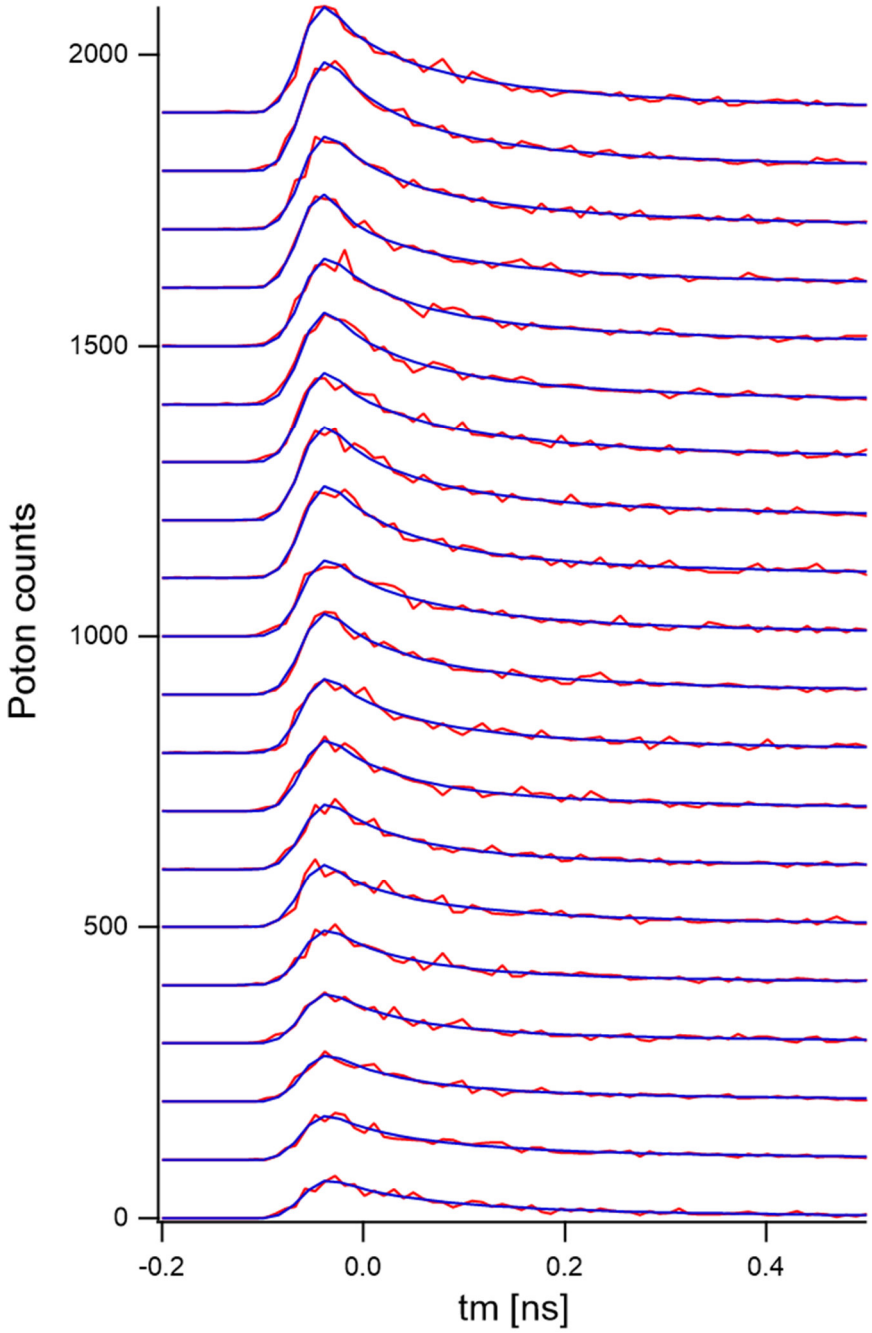

Figure 3-8 Fluorescence decay curves of 20 pixels randomly selected from a cell image (red lines) and their fitting results with the sum of four exponential decay models (blue lines).

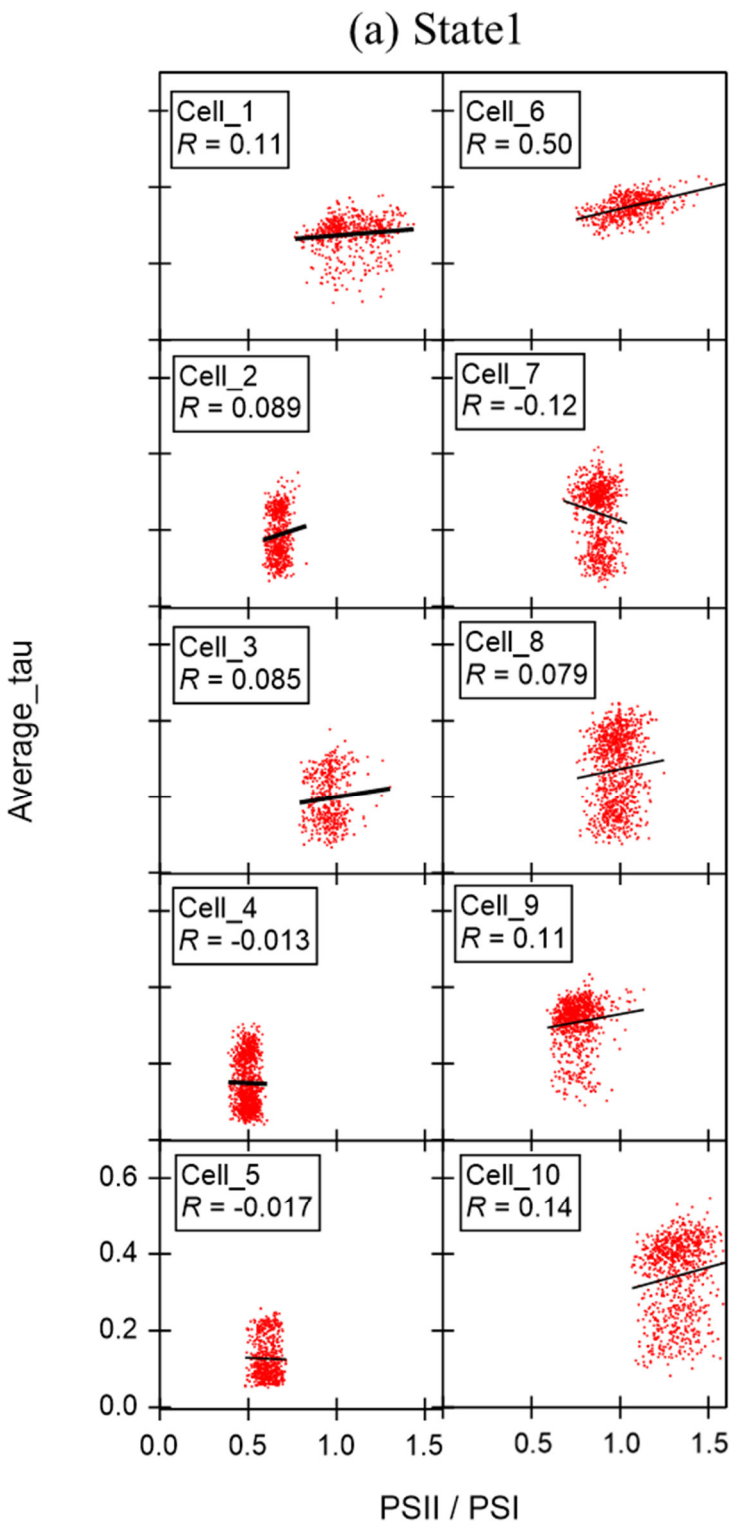
(a) State1
Cell_1
R = 0.11
Cell_6
R = 0.50
Cell_2
R = 0.089
Cell_7
R = -0.12
Cell_3
R = 0.085
Cell_8
R = 0.079
Cell_4
R = -0.013
Cell_9
R = 0.11
Cell_5
R = -0.017
Cell_10
R = 0.14
Average_tau
PSII / PSI
0.0
0.2
0.4
0.6
0.0
0.5
1.0
1.5

(b) State2

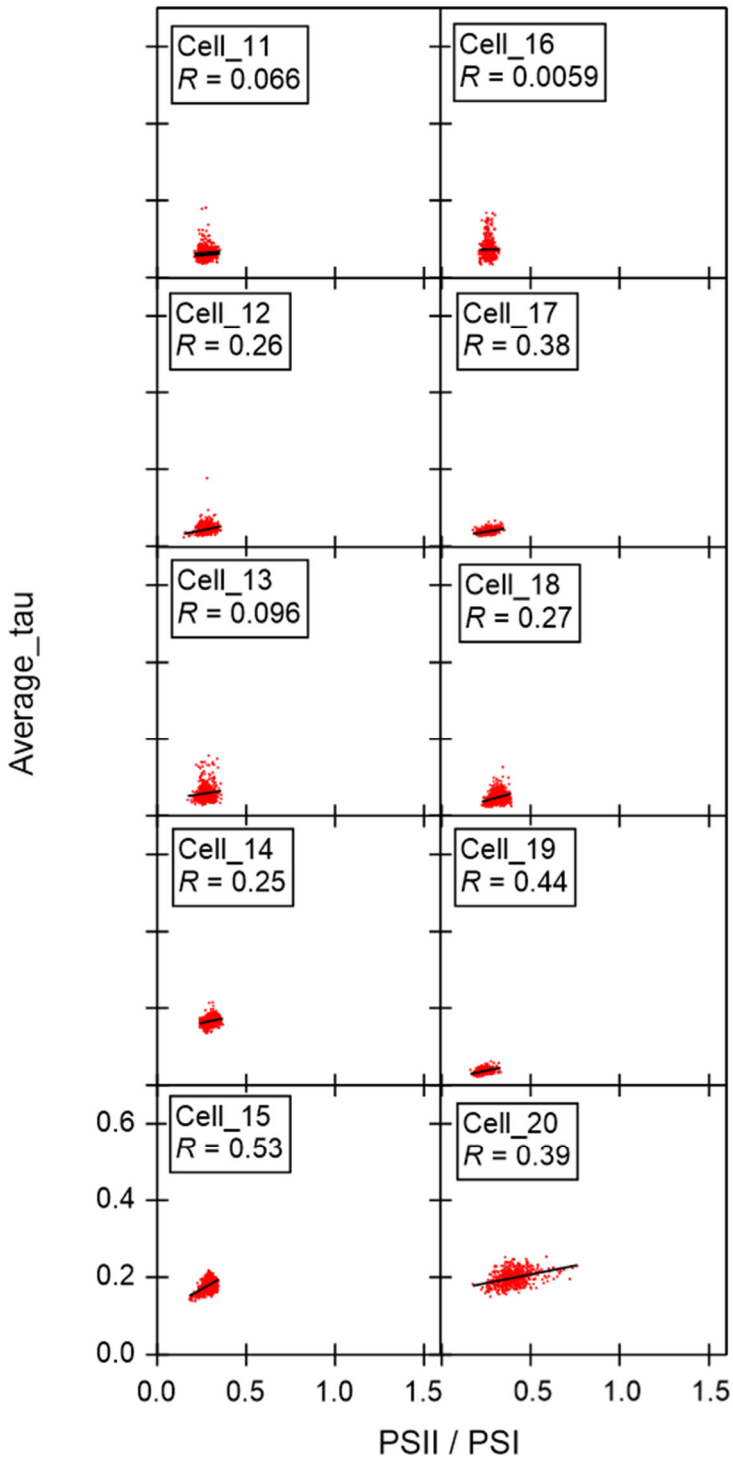
Cell_11
R = 0.066
Cell_16
R = 0.0059
Cell_12
R = 0.26
Cell_17
R = 0.38
Cell_13
R = 0.096
Cell_18
R = 0.27
Cell_14
R = 0.25
Cell_19
R = 0.44
Cell_15
R = 0.53
Cell_20
R = 0.39
Average_tau
0.0
0.2
0.4
0.6
0.0
0.5
1.0
1.5
0.5
1.0
1.5
PSII / PSI

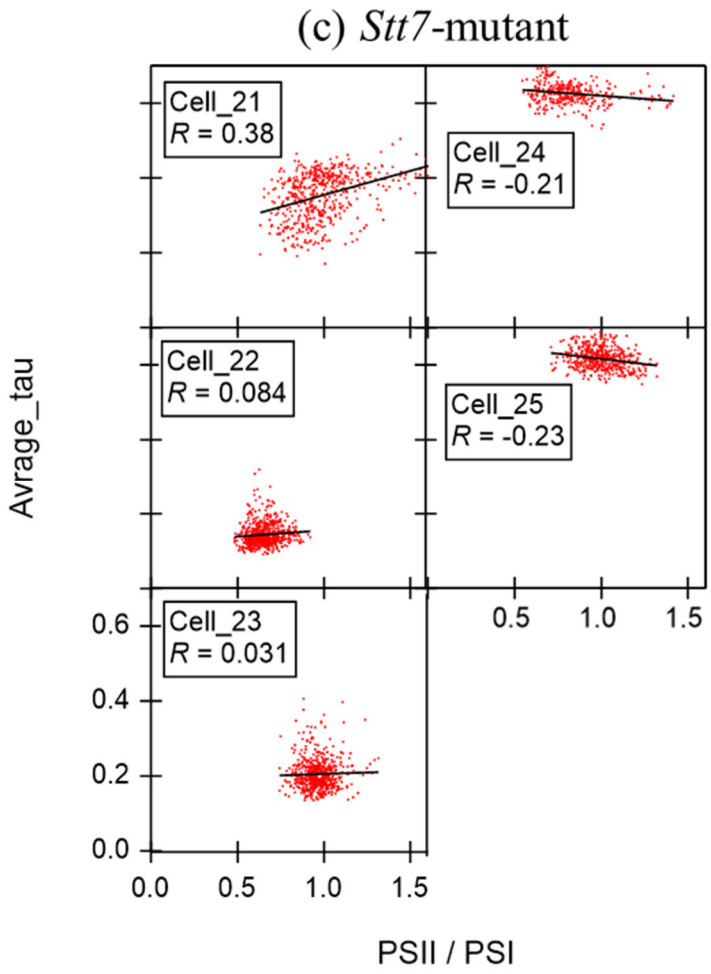

Figure 3-9 Correlation plots of the average tau (τ_{ave}) in ns unit vs. the PSII / PSI ratio within a cell (red dots). The black solid lines are the fitting to linear functions. Panels (a), (b), and (c) show the plots of cells induced to state1, state2, and stt7-mutatnt cells, respectively. The image of the cell in each panel can be found in Fig. 3-4 by referring the cell number indicated in boxes. The scales on the vertical and horizontal axes are the same for all graphs.

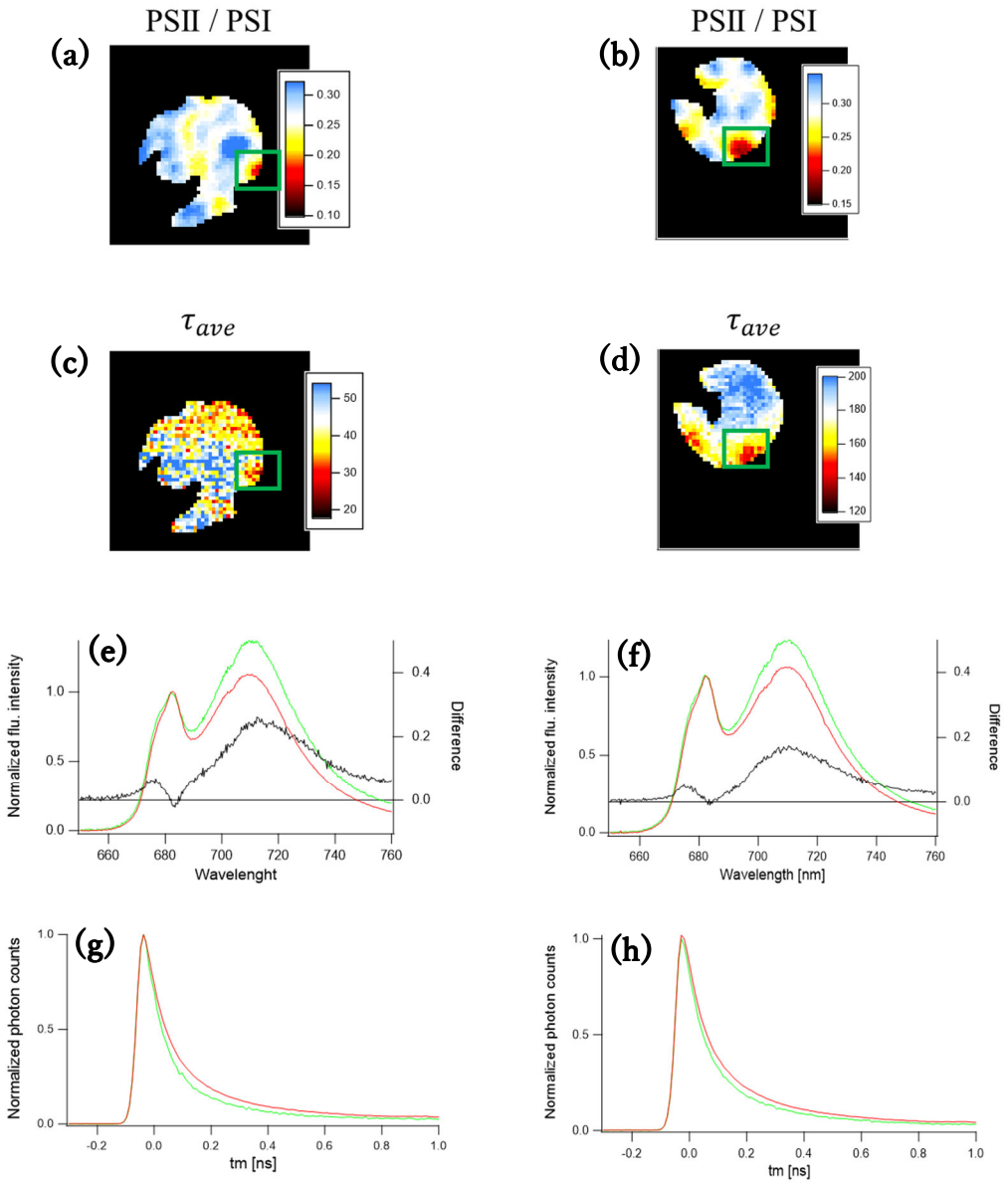

Figure 3-10 Panels (a, b) show PSII / PSI ratio maps of cell_12 and cell_15, respectively. Panels (c, d) show averaged fluorescence lifetime (τ_{ave}) images of the same cells as those in panels (a, b), respectively. The values on the color scale are shown in ps units. Green squares highlight the specific areas where conspicuously high PSI fluorescence and very fast fluorescence lifetime at around 680 nm were observed. Normalized fluorescence spectra and decay curves averaged over whole cells and within the green square areas are shown as red and green solid lines in panels (e, f, g, and h), respectively. Panels (e, g) reflect the signals of cell_12 and panels (f, h) show signals of cell_15. Black solid lines in panel (e, f) represent the difference spectra between red and green solid lines.

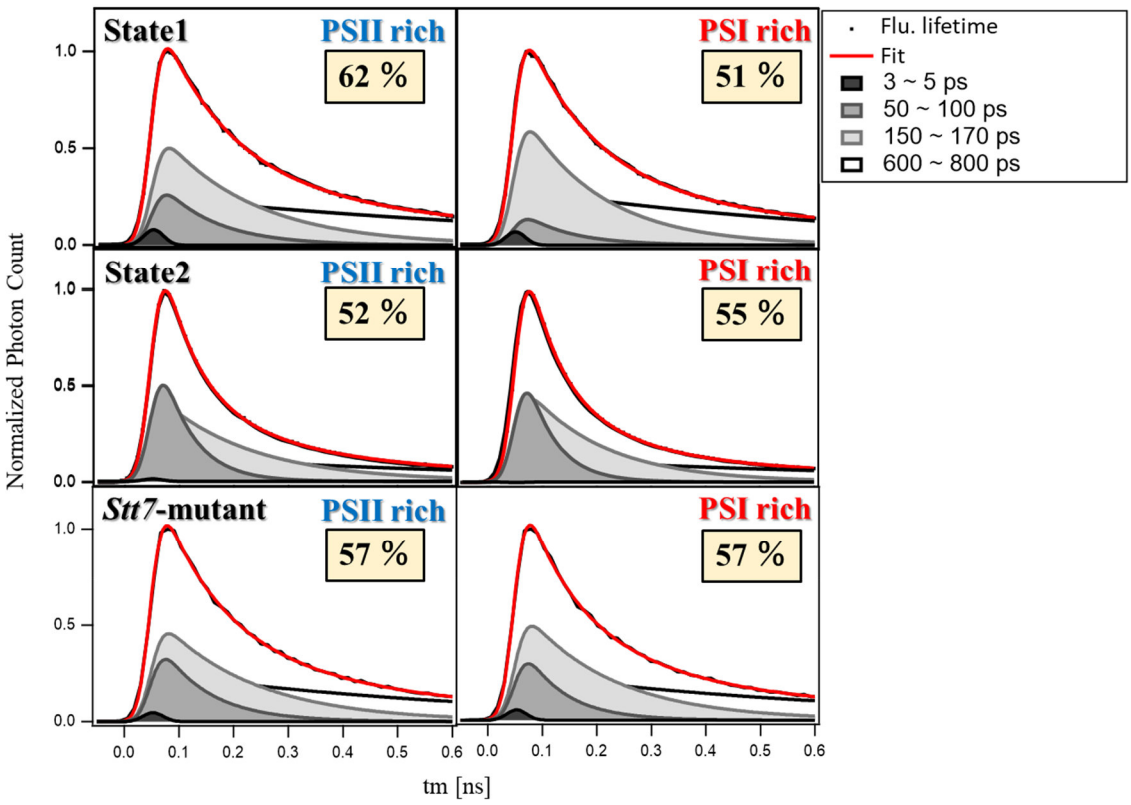

Figure 3-11 Black dots are the normalized fluorescence decay curve averaged over each region classified into the PSII-rich (left) and PSI-rich (right) in the state1-induced (top), state2-induced (middle), and *stt7* mutant cells (bottom). The obtained decay curves were re-fitted to the four exponential decay models convolved with the IRF. Fitting results are represented as red solid lines. Assigned four exponential decay components are superimposed as the curves filled with black, thick-gray, pale-gray, and white, respectively. The occupancy ratios of LHCII estimated as in section 3-6 are indicated in boxes.

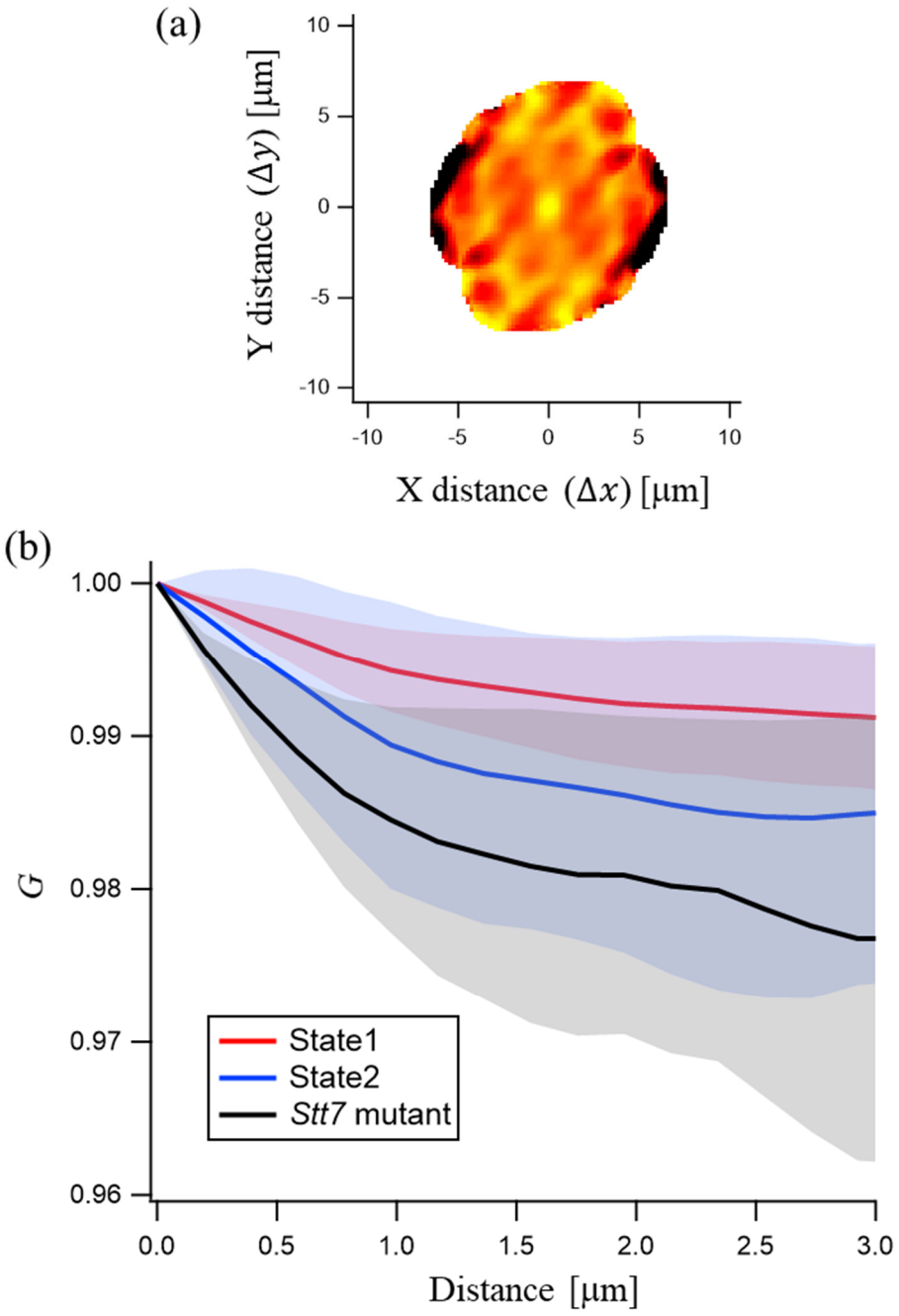

Figure 3-12 (a) A 2-D correlogram of cell_12. (b) Averaged 1-D correlograms over all measured cells in state1 (red solid line), state2 (blue solid line), and *stt7* mutant (black line). Red, blue, and gray fills represent the standard deviation of the 1D correlograms calculated for all measured cells in state1, state2, and *stt7* mutant, respectively.

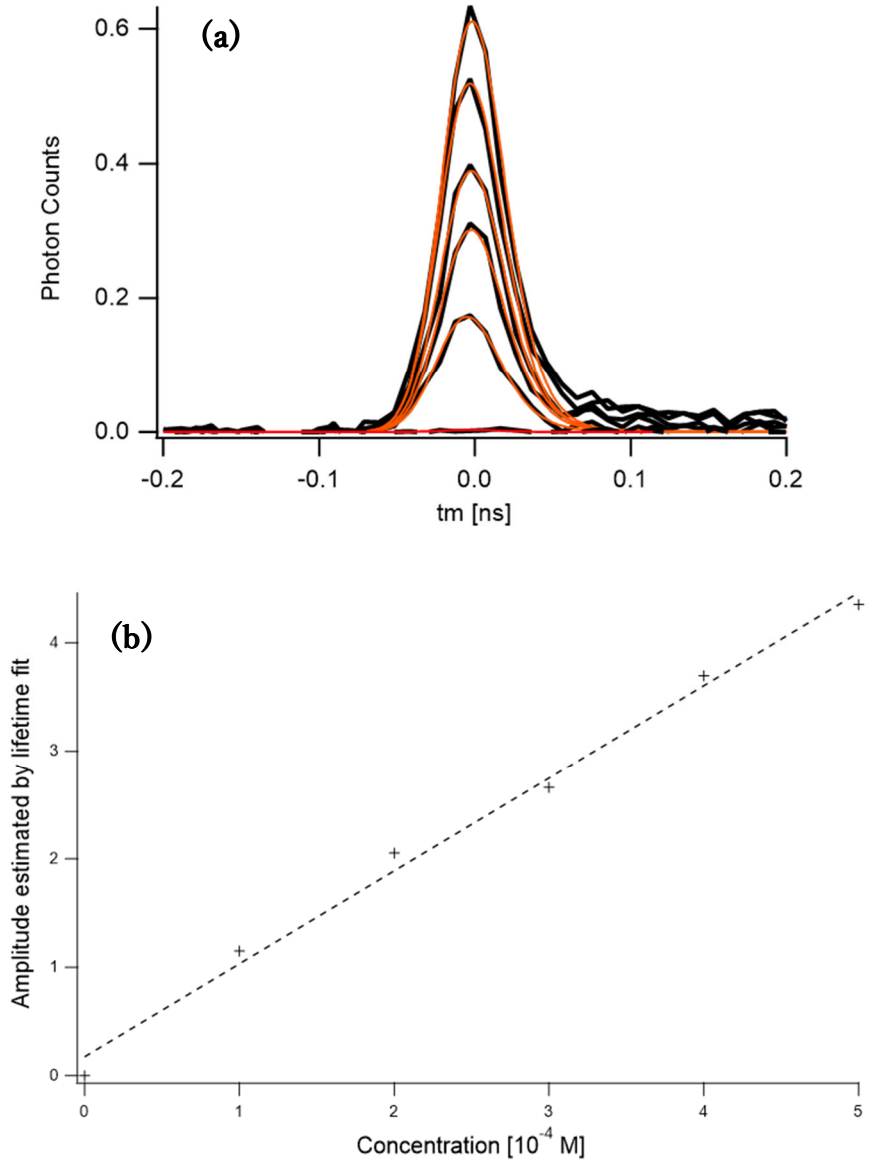

Figure 3-13 (a) Fluorescence decay curves of a malachite green aqueous solutions with several concentrations measured with the cryogenic FLIM system (black solid lines) and fitting curves to single Gaussian function (red solid lines). (b) Amplitudes of the fluorescence decays of the malachite green aqueous solutions are plotted against its concentration. The cross points show the measured data, and the dashed line indicates the linear approximation. Malachite green has a fluorescence lifetime of less than 1 ps, which is much shorter than the IRF of our system.

Table 3-1 The parameters obtained by the global fitting of the four spectra (state1, state2, isolated PSII-LHCII, and isolated PSI). The values of the linked components are omitted with the symbol ◆, and the components excluded from the fitting are listed as None (see section 3-2 for the detail). The values of the right of ± symbols show standard errors.

		State1	State2	Isolated LHCII-PSII	Isolated PSI
LHCII	Peak	676.2±0.4 nm	◆	◆	None
	FWHM	7.8 ±0.6 nm			
PSII	Peak	683.2 ± 0.8 nm	◆	◆	None
	FWHM	6.2 ± 0.4 nm			
	Peak	689.6 ± 2.0 nm	689.5 ± 2.7 nm	693.2 ± 1.1 nm	None
	FWHM	15.6 ± 2.1 nm	18.2 ± 2.9 nm	24.0 ± 1.3 nm	
PSI	Peak	709.7 ± 0.3 nm	◆	None	◆
	FWHM	26.3 ± 0.6 nm			
except	Peak	715.6 ± 1.0 nm	◆	◆	◆
	FWHM	64.7 ± 1.8 nm			

Chapter IV Streak Camera within Microscopic Area

4-1 Purpose of This Experiment

In Chapter 3, I discussed the correlation between the FQY, local concentrations of LHCII, and the intracellular heterogeneity of PSII/PSI ratio, by means of the acquirements of fluorescence spectrum and decay curve simultaneously at every pixel of the cell image. The bandpass filter at 680 nm made us to obtain the decay curve mainly involving signals from LHCII. However, since the contribution of the fluorescent signals of PSII and PSI was too large to be ignored in the 680 nm fluorescence band, it was difficult to extract the pure LHCI signal. Therefore, I could not discuss the local energy-transfer dynamics in detail. As described in sections 2-15, by using the time-resolved fluorescence spectra obtained by the streak camera and the subsequent DAS analysis which identifies the spectra associated with certain delay times, I can resolve the fluorescence spectrum contributed from LHCII and reveal the excitation energy transfer kinetics from LHCII to PSs. Recently, we have newly developed the cryogenic streak-camera optical microscope system, which provides us the streak image within microscopic sub-domains within a target cell at 80 K (see section 2-7). In this experiment, we have attempted to distinguish the spectrum from LHCII component, elucidate excitation energy transfer kinetics from LHCII to PSs, and reveal the function and localization of the free-LHCII.

4-2 Experimental Procedure

Figure 4-1 (a) shows an obtained typical fluorescence image of a *Chlamydomonas* cell induced to state1 and the fluorescence spectrum obtained from a certain pixel. Wavelength bands mainly assigned to PSII and PSI are highlighted on the spectrum graph in Fig. 4-1 (a) as blue and red fills, respectively. As I assumed in Chapter III, the fluorescence intensities of PSII and PSI directly reflect their local concentrations. Three-step excitation laser scanning was performed to detect the fluorescence signals in the PSII abundant and the PSI abundant regions within a cell by using the streak camera. I introduce the detail of this procedure in this section.

In the first step, the excitation laser was scanned over the whole cell and the fluorescence spectrum at each pixel was acquired with the polychromator + CCD camera. Then, I identified the intracellular PSI and PSII abundant regions by comparing the intensities assigned to PSII and PSI in a microscopic area. To do this, PSII/PSI ratio map was calculated by dividing the

fluorescence intensity integrated over the range of 676 – 692 nm (PSII preferential wavelength) by that over the range of 706 – 727 nm (PSI preferential wavelength) for every pixel of the image. Then, about 50 pixels with the largest and smallest PSII/PSI values were picked up as the PSII- and PSI-rich regions of the image, respectively. In the second and third steps, the excitation laser was scanned over the pixels belonging to the PSII-rich region and those belonging to the PSI-rich region identified in the first step, respectively. The beam splitter was set on the fluorescence path and reflected fluorescence was input to a multimode optical fiber to be guided (Fig. 2-12) to the streak camera for acquirement of the streak images Fig. 4-1 (b) and (c). During the second and third scans, signals were continuously accumulated by the streak camera to achieve a sufficient S/N ratios. Thus, the streak images averaged over the PSII-rich and the PSI-rich regions were obtained after the second and third scans, respectively. On the other hand, the fluorescence transmitted through the beam splitter was detected by the CCD camera during the second and third step to obtain the spectra accumulated over each specific region. These three-step scan and identification of the PSII-rich and PSI-rich region were realized by a self-written program operating on LabVIEW software (see section 4-3).

It should be noted that in Chapter III we identified PSII-rich and PSI-rich regions by means of the Gaussian decompositions with five components of the spectra of all pixels. We now recognized that the spectral overlap between the PSI and PSII is not significant and then using the fluorescence intensities integrated over the certain ranges works well to identify the PSII-rich and PSI-rich regions. In experiments with the three-step scans, it was important to minimize the effect of draft of the sample position during the three-step scans. The simplified identifications of the PSII-rich and PSI-rich regions were also effective to minimize the time interval between the first and the second scans and then minimize the drift.

4-3 Introduction of the Self-Written Algorithm of LabVIEW Software

Figure 4-2 shows the front panel window of the self-written LabVIEW program which conducts the three-step scan and identification of PSII-rich and PSI-rich regions. The detail of the role of each panel on the front window are explained below.

A sequence of the fluorescence spectra obtained at all pixels of the image is displayed in the panel (c). The panel (a) displays a fluorescence image generated by the total fluorescence intensity integrated over all wavelengths. The panel (b) displays the fluorescence image generated

by the signal integrated over the wavelength range specified by the red lines on the panel (c). Panel (d) shows an image in which only pixels with signal intensities beyond a certain threshold are highlighted in yellow. One can set any arbitrary threshold on the front panel window. The PSII-and PSI-rich regions are identified as the pixels satisfying the following equations,

$$\frac{\sum \mathrm{Gr}}{\sum \mathrm{Gr} + \sum \mathrm{Cy}} > \mathrm{Gr\_threshold}\,, \qquad \text{(Equation } 4-1 \text{ a)}$$

$$\frac{\sum \mathrm{Cy}}{\sum \mathrm{Gr} + \sum \mathrm{Cy}} > \mathrm{Cy\_threshold}. \qquad \text{(Equation } 4-1 \text{ b)}$$

Here, $\sum \mathrm{Gr}$ and $\sum \mathrm{Cy}$ are the fluorescence intensities of the PSII and PSI spectral regions integrated over the wavelength ranges specified by green lines and cyan lines on the panel (c), respectively. $\mathrm{Gr\_threshold}$ and $\mathrm{Cy\_threshold}$ can be set arbitrarily on the front panel window. Pixels satisfying Eq 4-1 a are displayed as green pixels on the panel (e), whereas those satisfying Eq 4-1 b are expressed as cyan pixels on the panel (e). You can regard the pixels specified by green and cyan as PSII-rich and PSI-rich regions, respectively. These pixel-pick up operations are applied only to the pixels highlighted in panel (d). In the second and third scan, excitation laser is only scanned on the colored pixels on panel (e). Unfortunately, the current algorithm is not able to synchronize the streak camera. In this experiment, the streak camera measurement was manually started at the same time as beginning of the second and third scans.

4-4 Performance Evaluation of the Self-Written Algorithm of LabVIEW Software

To confirm that the self-made algorithm exhibits the desired performance, we conducted a demonstration experiment using two fluorescent beads with different fluorescence wavelengths. As a sample, a mixed aqueous suspension of 250-fold diluted F8811 and F8807 containing 1% polyvinyl alcohol (PVA) was spin coated on a glass substrate. F8811 and F8807 have the center fluorescence wavelengths at 515 nm and 680 nm, respectively. The 460 nm excitation pulse laser with a laser power of about 5 μW on the sample surface was used.

Figure 4-3 (a) shows a typical fluorescence image of the thin-film containing the two types of the fluorescent beads obtained by the first-step scanning. The exposure time for each pixel was 0.05 s. Figure 4-3 (c) shows a fluorescence spectrum averaged over all pixels of the image. Two peaks reflect the signals from the two types of fluorescent beads (emphasized by blue and red bands in Fig. 4-3 (c)), indicating that both beads are present in the acquired image. Since the dichroic mirror with the cut-on wavelength at 550 nm was installed to separate fluorescence

and excitation lights, fluorescence signals below 550 nm were not observed. We integrated fluorescence signals in the 545 - 598 nm (F8811) and 656 - 707 nm (F8807) regions at each pixel. The former and latter are stored as $\sum \mathrm{Gr}$ and $\sum \mathrm{Cy}$, respectively. We specified the pixels exhibiting relatively high values of $\sum \mathrm{Gr}$ and $\sum \mathrm{Cy}$ as blue and red pixels in Fig. 4-3 (b), respectively, according to Eq 4-1. These series of operations are completed instantly on the LabVIEW software after acquirement of the fluorescence image. The black lines in Fig. 4-3(d) and (e) show normalized fluorescence spectra averaged over the pixels colored in blue and red, respectively. As you see, the main peaks in Fig. 4-3 (d) and (e) emerge at 550 nm and 690 nm, indicating successful selections of pixels exclusively containing either of the two beads.

In the second and third scans, the excitation laser was irradiated only on the selected pixels colored in blue and red. The exposure time for each pixel was set to be 3 s. The blue dashed dotted line in Fig. 4-3 (d) and red dashed dotted line in Fig. 4-3 (e) represent normalized fluorescence spectra detected by the CCD camera during the second (scanning on the blue pixels) and the third steps (scanning on the red pixels), respectively. As you see, the fluorescence spectra obtained by the second and third scans are similar to those obtained in the first scan, the black lines in Fig. 4-3 (d) and (e), respectively. This indicates that the excitation laser was scanned exclusively over the selected spots corresponding to the colored pixels. The blue solid line in Fig. 4-3 (d) and red solid line in Fig. 4-3 (e) show the normalized steady state fluorescence spectra detected by the streak camera. The spectra also exhibit a fluorescence peak derived from each fluorescent bead. These observations certified that the cryogenic streak-camera optical microscope system and the self-written LabVIEW program allow us to acquire the streak image corresponding to the specific microscopic area of interest.

The spectra obtained by the streak camera (blue and red lines in Fig. 4-3 (d) and (e)) have a much lower S/N ratio than those acquired by the polychromator + CCD camera (blue and red dashed dotted lines in Fig. 4-3 (d) and (e)). Since the maximum sampling rate of the streak camera is 20 MHz that is four-times lower than the repetition rate of the excitation pulse laser, the detection efficiency of the fluorescence signal is not so high as that of the CCD camera. Another factor is that a part of fluorescent signals delivered to the streak camera is lost due to passing through the optical fiber installed before the entrance of the streak camera. Although one solution is extension of the exposure times for the second and third scans, we also have to minimize the extra-irradiation to avoid the photodamage of the sample. Typically, the measurement for the

Chlamydomonas have been conducted with 5 s exposure time.

4-5 Time Resolved Fluorescence Spectra within Intracellular Subdomain

Figure 4-4 shows typical fluorescent images of *Chlamydomonas* cells measured in the first scan with the cryogenic streak-camera optical microscope system. Five cells induced to either state1 or state2 (Fig. 4-4 (a) and (b), respectively) were measured. A *Chlamydomonas* has a cup-shaped chloroplast as shown in Fig. 2-1. While several measured images reflect this characteristic shape, the other images exhibit a spherical shape. Similar microscope images of spherical *Chlamydomonas* cells were also observed in a previous investigation by using the structured illumination microscope (SIM), one of the super-resolution fluorescence optical microscopes. It was interpreted that the shapes of *Chlamydomonas* cells observed by the optical microscope depend on the orientations of the cells against the laser scanning-plane or the depth of the plane within the cells [74].

As I mentioned in Section 4-3, the identification of the PSII-rich and PSI-rich region is promptly completed by the self-written LabVIEW program after the first scanning finished. In this experiment, about 50 pixels were specified as the PSII-rich and PSI-rich regions for each measured cell (blue and red pixels in upper images in Fig. 4-4). The lower images in Fig. 4-4 represent the PSII-rich (blue) and PSI-rich (red) regions estimated by the Gaussian decomposition of the spectrum at every pixel as in Chapter III. In this case, about 100 pixels are colored and displayed. The spots of the blue-red pixels shown in the upper and lower images nicely matched, indicating that the PSII-rich and PSI-rich regions were as successfully distinguished as done by the method described in Chapter III.

Figure 4-5 shows the accumulated streak images within the intracellular PSII-rich and PSI-rich regions and their steady state fluorescence spectra. The monitor range of the delay time was set to 2 ns. The previous report has suggested that each PSs has a fluorescence decay component with a lifetime longer than 1 ns. Thus, the 2-ns time range seems insufficient to estimate the slower time constants correctly. Even though, the 2 ns time range was applied so as to ensure the evaluation of the lifetime behaviors of LHCII exhibiting a relatively shorter time constant. The streak images of the PSII-rich and PSI-rich sub-regions were obtained for each measured cell. Then, I accumulated the streak images for the five measured cells induced to either state1 (Fig. 4-5 (a, b) for PSII-rich and PSI-rich, respectively) or state2 (Fig. 4-5 (c, d) for PSII-

rich and PSI- rich, respectively). As far as I know, this is the first achievement to obtain streak images for selected sub-cellular domains under the microscope. Actually, the acquired streak images are slightly tilted due to the chirp effect of the optical fiber. Figure 4-5 displays the streak images corrected for the chirp by using the data of the malachite green aqueous solution as described in sections 2-13.

The steady state fluorescence spectra displayed below the streak images in Fig. 4-5 were calculated by integrating them along the time axis. All the spectra exhibit the PSII/ PSI intensity ratios which are consistent with the change in the absorption cross-section of PSs upon the state transitions and the difference in the content of PSs within the measured microscopic sub-domains.

4-6 The DAS Analysis for the Obtained Streak Images

Figure 4-6 (a) shows the same streak image as that displayed in Fig. 4-5 (c). The streak image from 662 nm to 730 nm was divided into 17 segments represented by the white lines in Fig. 4-6 (a). Then, 17 decay curves were calculated by integrating the 17 segments along the wavelength axis. Figure 4-6 red solid lines represent the 17 decay curves extracted from the streak images for PSII-rich and PSI-rich regions in state1 (b, c) and those in state2 (d, e). The center wavelengths of the segments are also given in Fig. 4-6 (b). All the decay curves in each panel of Fig. 4-6 were globally fitted to sum of four exponential decay models convolved with the IRF according to Eq 2-15. FWHM of the IRF was estimated to be 27 ps by using the malachite green aqueous solution (see section 2-12). In this global fitting, t_o (the peak position of the IRF) and τ_i (each time constant) were constraint to have the same values between the 17 decay curves and only A_i (amplitude corresponding to each time constant) was set free to vary. Blue lines in Fig. 4-6 (b, c, d, and e) represent the fitting results.

Figure 4-7 (a, b, c, and d) indicate the DASs calculated for the PSII-rich and PSI-rich regions in the state1-induced cells, and those for the PSII-rich and PSI-rich regions in the state2-induced cells, respectively. These DASs were produced by plotting the estimated F_i against the center-wavelength of the corresponding decay curve. The annotations in Fig. 4-7 indicate the determined time constants associated with the DAS components. Surprisingly, DAS components with extremely short time constants (< 10 ps) were identified by the present analysis (black lines in Fig. 4-7). Similar fast lifetime component was found in the measurement with the cryogenic FLIM microscope system (see Chapter III). The validity of the estimation of A_i with the shorter

time constant than the IRF will be confirmed in section 4-7.

Green and red solid lines in Fig. 4-7 shows the DASs with relatively slower time constants. These DASs are positive over the whole spectral range from 685 nm to 720 nm, indicating no contribution of the energy-transfer process. They can be assigned to the pigments bound to PSs and having lower excitation energies than the primary dimer (PD) where charge-separation reaction occurs. Due to their low excitation energy, energy transfer hardly occurs from these pigments to the PD. Therefore, these pigments emit fluorescence with a slow lifetime comparable to the natural lifetime. Since the estimated time constants were significantly faster than the natural lifetime, the fluorescence decay from the PD might be mixed in these DAS components. In the measurements with the cryogenic FLIM system discussed in Chapter III, the fluorescence decay at around 680 nm was apparently slower for the cells in state1 than those in state2. The fitting with sum of exponential decay models suggested an increase in the contribution of the component with the 190 ps time constant as the origin of the slower decay in state1. The main factor for the increase of the 190-ps component seems to be attributed to the enhanced fluorescence from CP47, which has been reported to exhibit relatively slow fluorescence lifetime and red-shifted fluorescence [99]. The DASs with ca. 150-ps time constant in state1 (green lines in Fig. 4-7 (a, b)) exhibited relatively higher peak intensity at around 688 nm than those in state2 (green lines in Fig. 4-7 (c, d)), which is similar to the behavior of the ca. 190-ps component obtained with the FLIM measurement. Since previously reported study suggested that CP29 can migrate to PSI together with LHCII upon state transitions, we interpreted that the reduction in the supply of excitation energy to CP47 due to the depletion in antenna size causes a decrease in the fluorescence signals belonging to the ca. 150-ps component in state2 [29].

Blue solid lines in Fig. 4-7 shows the DASs with ca. 50-ps time constants. In state1, these DAS exhibit positive contribution at around 680 nm, suggesting loss of fluorescence due to the excitation energy in an antenna Chl. being trapped by RC. In state2, on the other hand, the DAS components with similar time constants of 40-50 ps have positive peaks at around 680 nm and negative peaks at around 710 nm. As I described in section 2-15, a DAS component with positive and negative peaks reflects excitation energy transfer from a donor with the emission at the positive peak to an acceptor with the emission at the negative peak. Thus, the obtained DASs for state2 indicate the energy transfer from LHCII to PSI apparently with ca. 50 ps time constant. It strongly corroborates the LHCII attachment to PSI upon the induction to state2, and the

estimated time constant is good agreement with the previously reported observation (about 50 ps) [104]. As I mentioned in section 2-15, the absolute amplitude of a DAS component reflects the local concentration of the pigment contributing to the DAS. The minus peak in DAS for the PSI-rich region in state2 (blue solid line in Fig. 4-7 (d)) slightly more prominent than that for the PSII-rich region in state2 (blue solid line in Fig 4-7 (c)), indicating that LHCII-PSI super complex are more abundantly included in PSI-rich region. Since the current analysis cannot make finer resolution of the DAS components due to the limited S/N ratios of the decay curves, it is difficult to distinguish the spectral components at around 680 nm that reflect either energy transfer to RC within PSII or energy transfer from LHCII to PSI.

The error bars of the DASs with the shortest time constants (black solid lines in Fig. 4-7), which indicate the standard error of the global fitting, are larger than those with the other time constants (especially, the error bars of the DASs in state2 PSI-rich region, in Fig. 4-7 (d)). This is presumably due to the difficulty in the accurate estimation of the parameters of the component with time constants shorter than IRF. Even though, we can obtain spectra with positive and negative peaks reflecting the excitation energy transfer. In state1, DASs for both the PSII-rich and PSI-rich regions indicated energy transfer from the 675-nm emitting to 685-nm emitting species. Previously reported study showed that CP 29 involved in LHCII-family transfer the excitation energy to CP47 with a time constant of about 15 ps [42], which is roughly the same as the shortest time constants of the obtained DASs. We interpreted that the above positive and negative peaks reflect the energy transfer from CP29 to CP47. This is consistent with the assumption mentioned above that the increase in the amplitude at 688 nm of the 150-ps DAS component in state1 is attributed to the increases in the energy supply to CP47. In the 7.5-ps DAS in the PSII-rich region, a negative peak appeared at around 710 nm. This negative band is contributed from the acceptor species, which receive energy form the 675-nm emitting species. This negative peak was not seen for the 8.8-ps DAS in the PSI-rich region, excluding the possibility of the energy transfer from LHCII to PSI. We assumed that the negative peak at around 710 nm in the 7.5-ps DAS in the PSII-rich region of state1 reflects the formation of PSII-PSI megacomplexes localized in the PSII-rich region. The existence of the PSII-PSI megacomplexes and the energy transfer from PSII to PSI called spillover have been also suggested in the previous report [105].

In State 2, there are large differences in the fastest DASs between the PSII-rich and PSI-rich regions. In the PSII-rich region in state2, the fastest?? DAS suggested the energy transfer

from the 675-nm emitting to 685-nm emitting species can be assigned to that from LHCII to PSII as in state1. This suggests that not all LHCIIs move to PSI upon the induction to state2. In the PSI-rich region, the fastest DAS exhibits a drastically short time constant of 3.5 ps and a blue-shifted negative peak at around 680 nm. We interpret that it reflects the energy transfer within super complexes of LHCII-LHCI-PSI. Recently, Cryo-EM observations revealed that the two LHCII-trimers are connected to the side of PSI where LHCI is not attached as shown in Fig. 1-7. Calculation based on the identified Chl positions and orientations have revealed the possible two-step energy-transfer pathway from outer LHCII trimer to PSI via inner LHCII-trimer. In our DAS analysis, we can see a coincidence between the positions of the negative peak of the 3.5-ps component and the positive peak of the 42-ps component which is specified as the LHCII associated with PSI (see black and blue lines in Fig. 4-7 (c, d)). Based on the above considerations, we conclude that the excitation-energy transfer from the outer LHCII to the inner one has the time constant of 3.5-ps, then the energy arrives at PSI core part with the 42-ps time constant.

Surprisingly, we found another positive peak around 695 nm in the 3.5-ps DAS for the PSI-rich region. It is quite unlikely that the positive peak at 695 nm indicates an energy feed to the 680-nm emitting species showing a negative peak in the 3.5-ps DAS, since such an uphill energy transfer should be highly suppressed at low temperatures. Instead, this positive peak at around 695 nm suggests an existence of a rapidly decaying emission species at this wavelength. We interpret this component as the free-LHCII, which does not transfer the excitation energy to neighbors and exhibits a drastically rapid fluorescence decay. Several previous reports have suggested the existence of the free-LHCII, which connects to neither PSII nor PSI exhibits and is in a quenched state probably due to the formation of aggregate. Furthermore, the assumed formation of the aggregate is considered to induce the red-shifted fluorescence feature. In spite of frequent reports on the aggregated free LHCIIs, their locations have never been clarified. Based on our present cryo-microscope observations, we could obtain for the first time experimental evidence which strongly supports the localizations of the aggregated free-LHCII in the PSI-rich region upon induction to state2.

The validity of the determination on the DAS components with the substantially shorter time constants than the IRF will be discussed in Section 4-7. Here, I test the validity of the positive peak of the 3.5-ps DAS at around 695 nm. Blue and red solid lines in Fig. 4-8 (a) shows the decay curves integrated from 680 nm to 700 nm of the streak images for the PSII-rich and PSI-rich

regions in state2, respectively. The curves in Fig. 4-8 were integrated over a wider wavelength region than those used for the DAS analysis in order to improve the S/N ratio. As you can see, the red solid line clearly exhibits a more rapid rise than the blue one. Figure 4-8 (b) and (c) show the results of the renewed fitting of the decay curves to the sum of four exponential decay models. In this fitting, the time constants were fixed to those obtained in the DAS analysis. The assigned exponential components with time constants shorter than 10 ps (black fills in Fig. 4-8 (b) and (c)) showed substantially different contributions to the time profiles between the PSII-rich and PSI-rich regions: in the former it has a negative amplitude showing the fluorescence rise with this time constant, whereas in the latter it gives a positive amplitude clearly indicating the existence of the very rapid fluorescence decay. It should be noted that the decay curves of the PSII-rich and PSI-rich domains were measured for the same cells. Therefore, there is no ambiguity in the relative position of t_0, the time origin of the excitation laser, between the two curves. This ensures the validity of the above test.

Figure 4-9 shows an up-dated model of state transitions based on the results of the present study. The estimated time constants of the energy transfer from LHCII, and fluorescence emitted from PSs are also given in Fig. 4-9. A part of LHCII moves to PSI upon the transition to state2. As a new finding, aggregated free LHCII in the quenched state and with the red-shifted fluorescence is localized in the PSI-rich region in state2. It is considered that these functions are equipped to inhibit the ROS generation caused by the prolonged excited state of Chl.

4-7 Validity of Identification of a Fast Lifetime Component

In our lifetime measurement using the cryogenic streak-camera microscope system, we found drastically faster lifetime component (time constant with < 10 ps) than the IRF. In order to evaluate the accuracy in determining an amplitude of the rapidly decaying component by the present system, we measured a standard dye malachite green known to have a very short fluorescence lifetime of less than 1ps [78, 79] while changing its concentration (black solid lines in Fig. 4-10 (a)). Obtained decay curves were fitted to single Gaussian function (red solid lines in Fig. 4-10 (a)). Amplitude of the fluorescence decay of a malachite green aqueous solution estimated by the fitting is plotted against its concentration (crosses in Fig. 4-10 (b)). the dashed line in Fig. 4-10 (b) indicates the linear approximation. From the observation, we could confirm a sufficient linearity between the concentration and the amplitude of decay curve even for a

fluorescent dye having a shorter lifetime than IRF.

4-8 Streak Measurement for Bulk *Chlamydomonas* Cell Suspension

To assess the validity of the exponential components identified through the measurement with the cryogenic streak camera optical microscope system and the subsequent DAS analysis, we conducted a conventional streak-camera measurement for a bulk-*Chlamydomonas* cell suspension, providing a streak image with high S/N ratios. The obtained streak image for a bulk- *Chlamydomonas* cell suspension at 77-K are shown in Fig. 4-11 (a). As the bulk sample, the suspension in HS medium is immersed in liquid nitrogen in a Dewar vessel and mounted before the entrance of the streak camera. The excitation pulse beam from the fs Titanium: Saphire laser was irradiated to the sample and fluorescence was detected by the streak camera. The size of the focal spot can be roughly estimated to be 30 μm and the laser power was regulated to 200 uW so that the laser power per unit area was the same as that applied to the cryogenic streak camera optical microscope system. During the signal-accumulation time of 1000 s, the sample position was manually moved slowly so that it changed about 100 μm in 5 s. This handling was done to realize the same excitation condition as that done in the cryo-microscope measurement, in which an extreme care was taken to avoid inhibition of any photo-induced change in the sample by the excitation laser. The red and blue solid lines in Fig. 4-11 (b) show the fluorescence decay curves integrated from 675 to 685 nm of the streak image obtained for the bulk sample and for intracellular PSII-rich region in state2 measured with the cryogenic streak camera optical microscope system, respectively. As you see, the decay curve obtained from the bulk sample exhibit a significantly longer lifetime. This behavior is seen in those at all fluorescence-wavelength range. One plausible factor is the temperature difference between the sample in the Dewar vessel and that in the sample holder set in the cryostat. In the case of the bulk measurement, the sample suspension was sealed in a perforated copper plate and the edge of the plate was immersed in liquid nitrogen, ensuring a temperature very close to 77 K. On the other hand, in the low temperature measurement with the cryostat, the sample holder made of cupper is cooled by the flow of liquid nitrogen, resulting in the slightly rise in the temperature above the 77 K. The temperature of the sample holder is estimated to be 80-85 K by means of the thermocouple. The decay curve measured with the microscopic system may exhibit shortened lifetime possibly because the elevated temperatures increased the probability of the energy access through the

uphill energy transfer to the RC where the energy is trapped. To verify this, the streak measurements of bulk *Chlamydomonas* cells were performed with several temperatures. In the detail, the vessel was left to stand, and three streak images were acquired every 30 minutes. Cyan, green, and red solid lines in Fig. 4-11 (c) represent the decay curves integrated over the same range and measured at elevated temperatures. Although we could not record the temperature in current bulk-measurement set up, the surface of liquid nitrogen was below the edge of the copper plate at the time of the final streak measurement (red solid line in Fig, 4-11 (c)). Blue solid line in Fig. 4-11 (b) is the same as that in (c). Against the above expectation, decay curves for the sample with gradually-elevated temperatures did not show as short decay as that for the measurement with the microscope system. At present, we assume that the bulk measurement provides signals significantly contributed from contaminated broken cells exhibiting relatively slow lifetime.

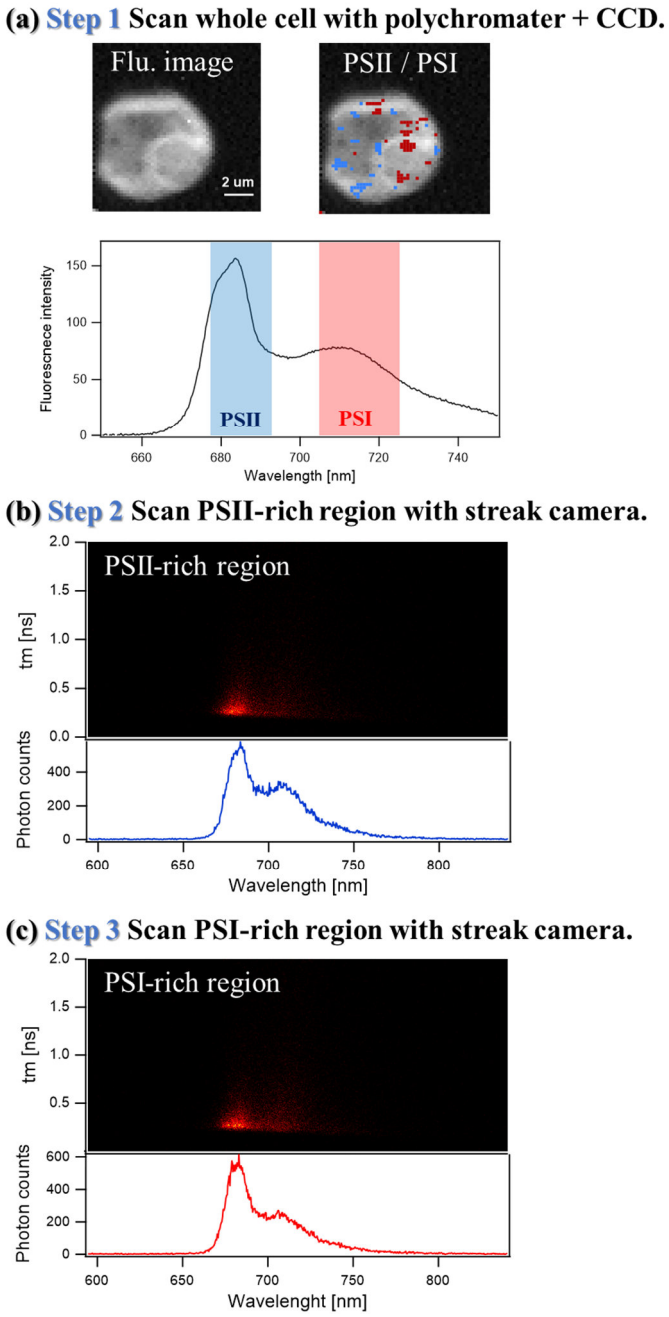

Figure 4-1 Typical results obtained by the three-step scan measured with the cryogenic streak-camera optical system. (a) Typical fluorescence image and fluorescence spectrum obtained at a certain pixel. Wavelength bands mainly assigned to PSII and PSI are highlighted as blue and red fills respectively. The PSII / PSI image in (a) indicates PSII-rich region and PSI-rich region as blue and red pixels, respectively. Typical streak images in (b) and (c) are obtained for PSII-rich pixels and PSI-rich pixels, respectively. Fluorescence spectra given lower the streak images are calculated by integrating them along the time axis.

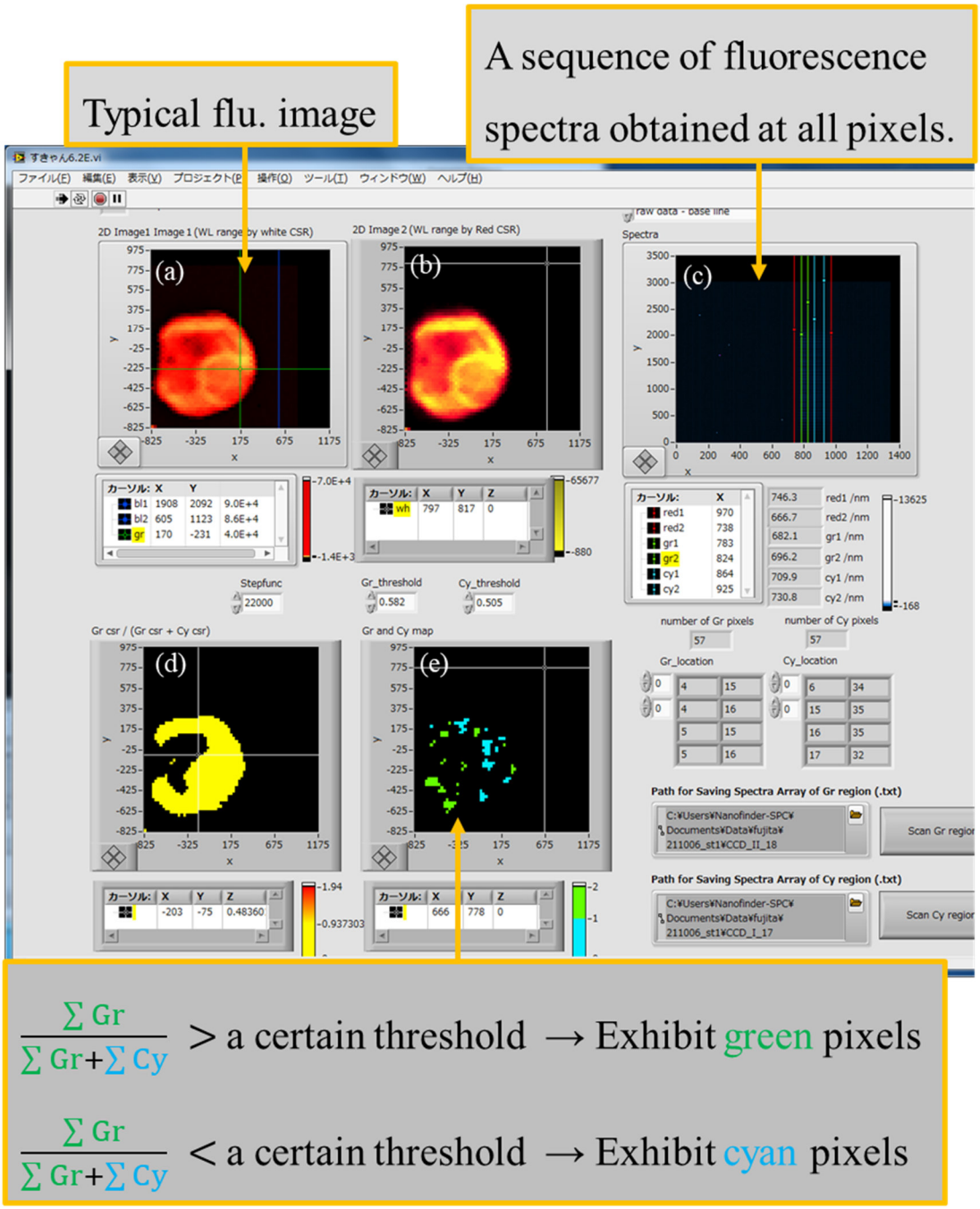

Figure 4-2 A front panel window of the self-written LabVIEW program which controls the three-step scan and identification of PSII-rich and PSI-rich regions. See the text in section 4-3 for the detail.

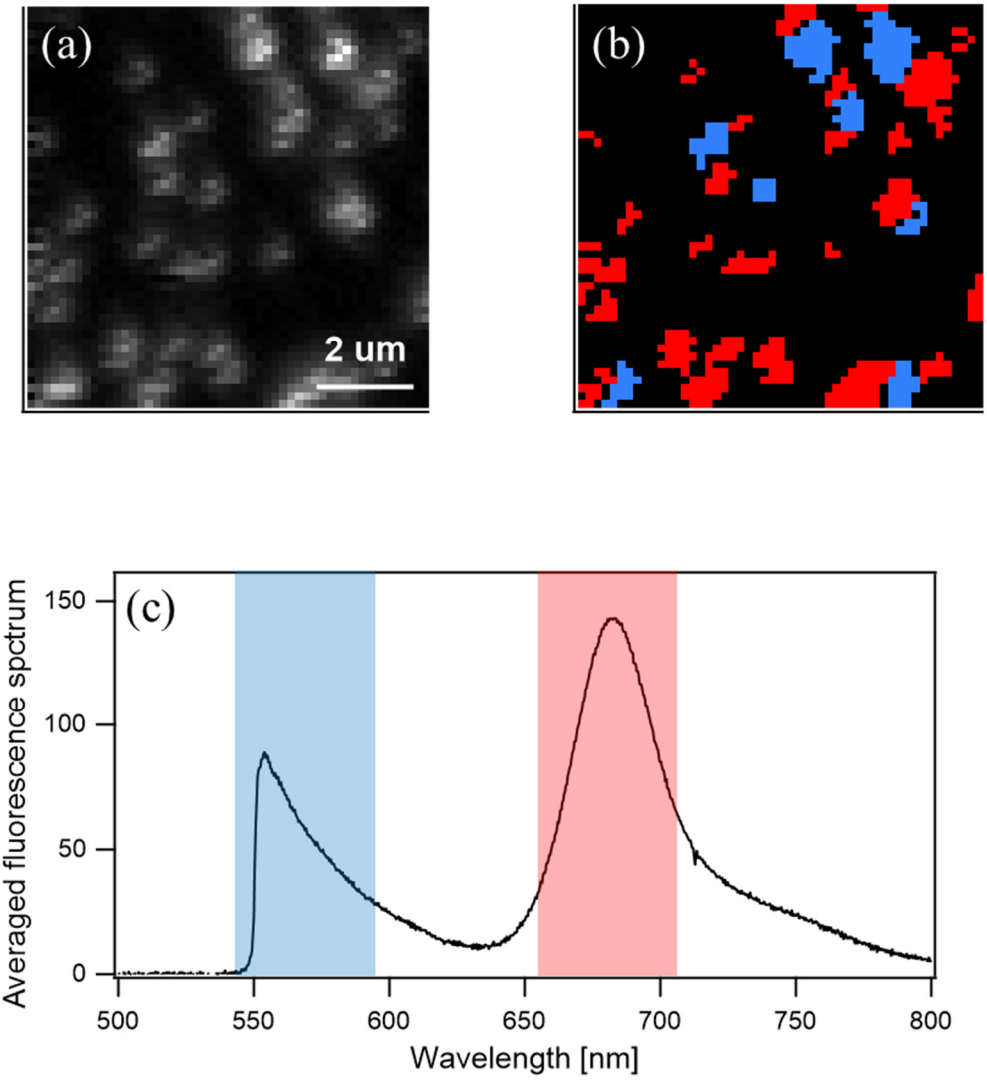
(a)
2 um
(b)
(c)
Averaged fluorescence spctrum
150
100
50
0
500
550
600
650
700
750
800
Wavelength [nm]

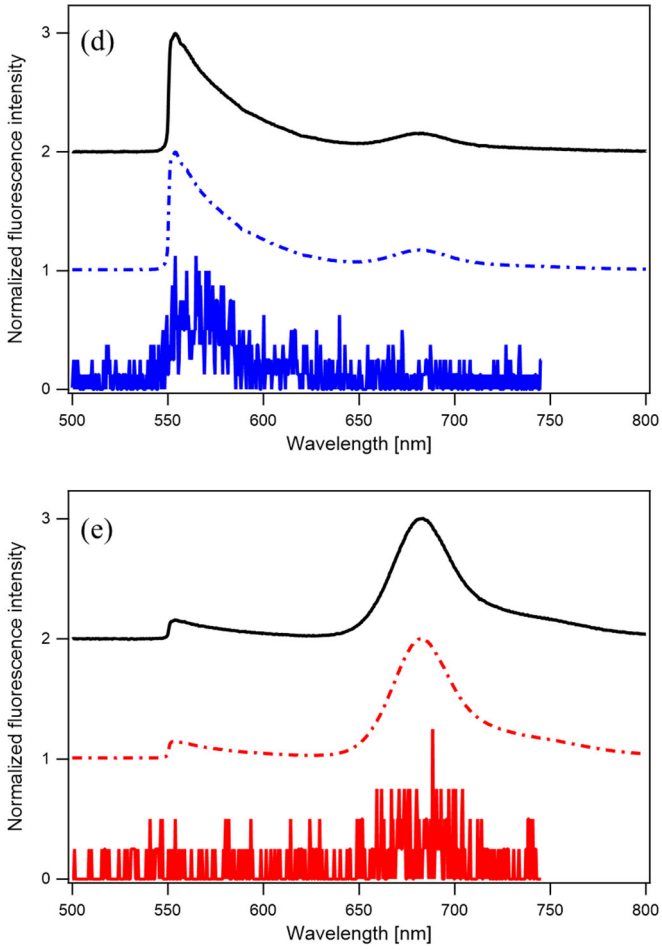

Figure 4-3 (a) Typical fluorescence images of a thin-film sample containing two types of fluorescent beads (F8807 and F8811) measured with the cryogenic streak-camera optical microscope. (b) The same image as in (a) with pixels with relatively higher fluorescence signals from F8807 and F8811 highlighted by blue and red, respectively. (c) A fluorescence spectrum averaged over all pixels in image (a). The two fluorescence bands mainly contributed from F8807 and F8811 are highlighted as blue and red fills, respectively. Black solid lines in panel (d) and (e) represent a fluorescence spectrum averaged over blue and red pixels in panel (b), respectively. Blue dashed dotted line in panel (d) and red dashed dotted line in panel (e) are the fluorescence spectra, detected by the CCD camera while the excitation laser was scanned over the pixels colored by blue and red, respectively. Blue solid line in panel (d) and red solid line in panel (e) are the fluorescence spectra, detected by the streak camera while the excitation laser was scanned over the pixels colored by blue and red, respectively. All spectra in panel (d) and (e) are normalized at each peak position.

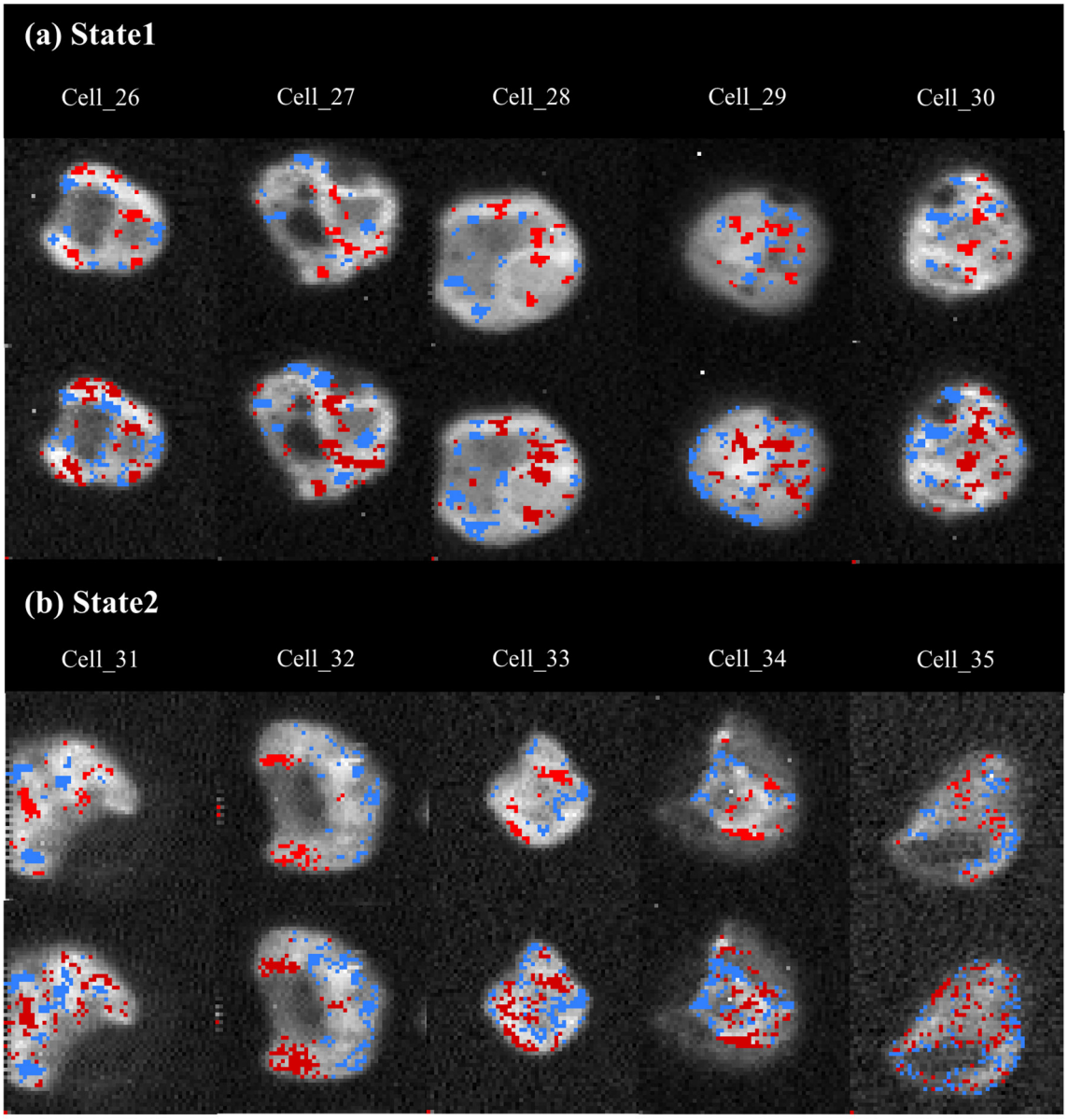

Figure 4-4 Typical fluorescence images of five *Chlamydomonas* cells induced to either state1 (a) or state2 (b) measured with the cryogenic streak-camera optical microscope system. We add a serial number to each cell. Blue and red pixels in the upper images highlight the spots where the excitation laser was scanned in the second (PSII-rich region) and third (PSI-rich region) steps, respectively. The lower images represent the PSII-rich (blue) and PSI rich (red) regions estimated based on the Gaussian decompositions of the spectrum at every pixel.

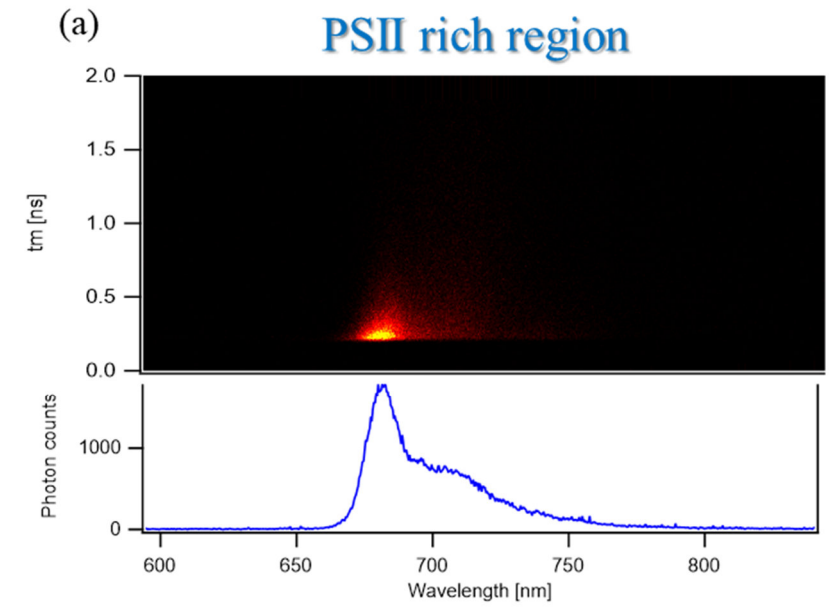
(a)
PSII rich region
2.0
1.5
1.0
0.5
0.0
tm [ns]
Photon counts
1000
0
600
650
700
750
800
Wavelength [nm]

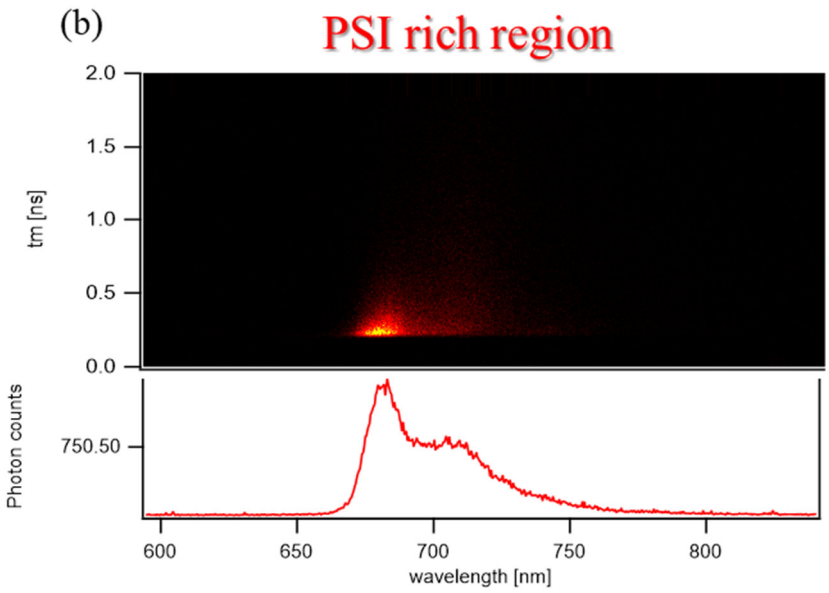
(b)
PSI rich region
2.0
1.5
1.0
0.5
0.0
tm [ns]
Photon counts
750.50
600
650
700
750
800
wavelength [nm]

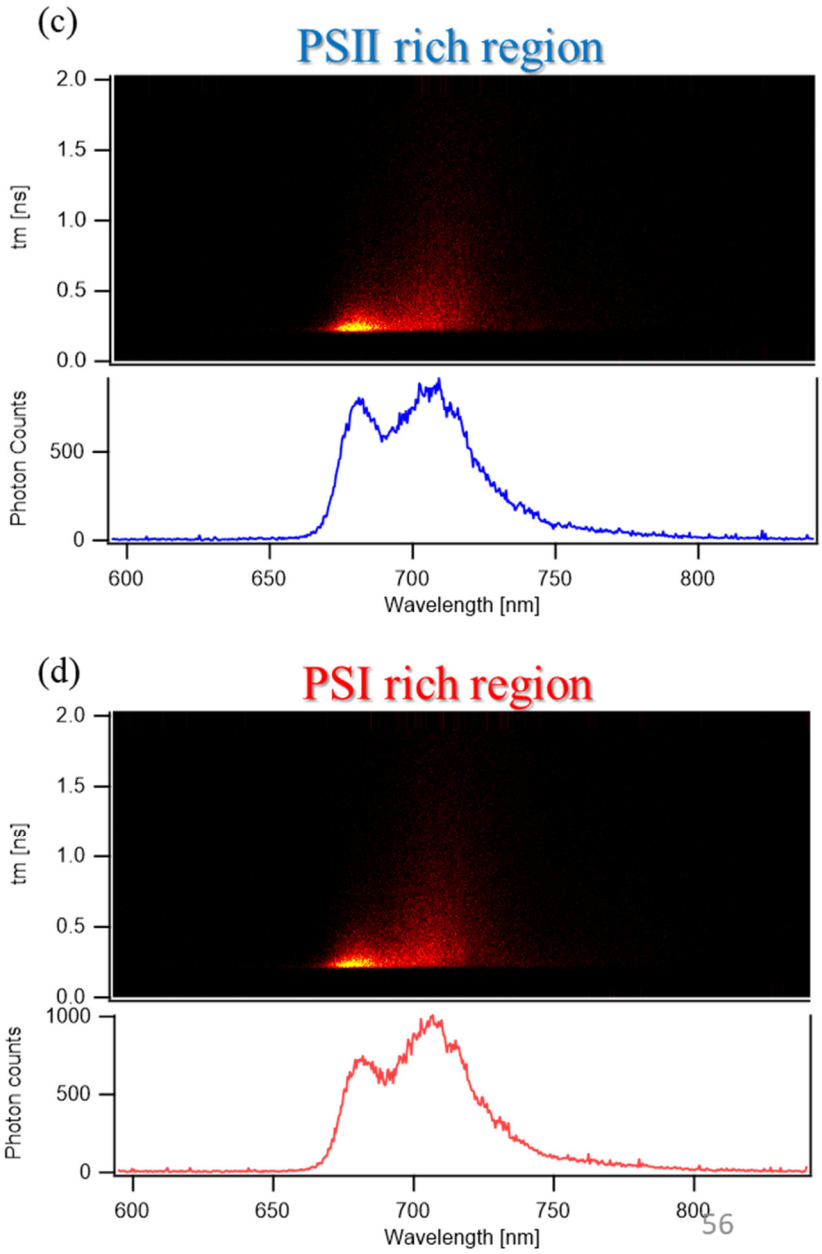

Figure 4-5 Accumulated streak images and their steady state fluorescence spectra calculated by integrating the images along the time axis for the specific microscopic areas of *Chlamydomonas*. Each obtained streak image is accumulated for five measured cells induced to state1 ((a) for PSII-rich and (b) for PSI-rich regions) or state2 ((c) for PSII-rich and (d) for PSI-rich regions).

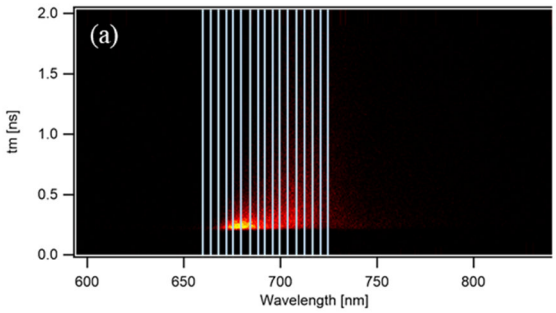
(a)
tm [ns]
2.0
1.5
1.0
0.5
0.0
600
650
700
750
800
Wavelength [nm]

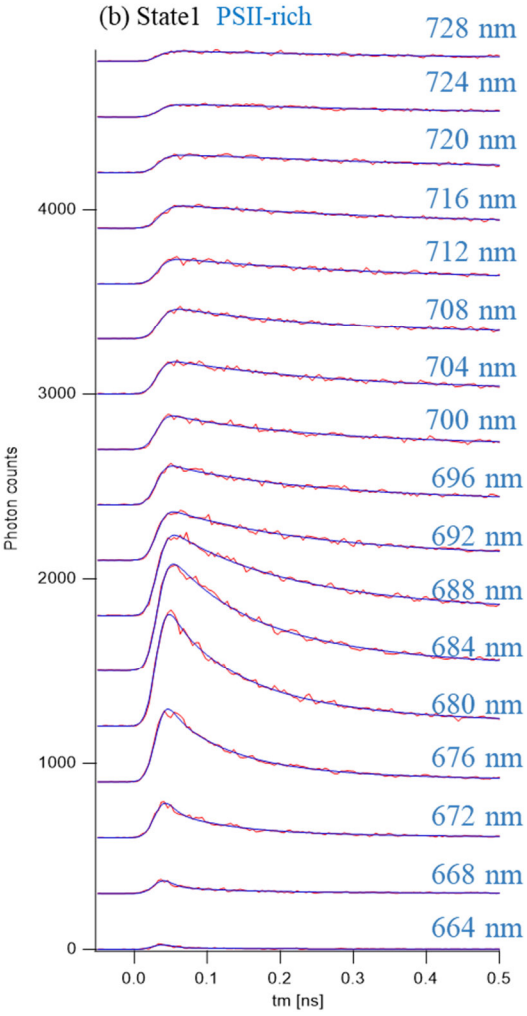
(b) State1 PSII-rich
728 nm
724 nm
720 nm
716 nm
712 nm
708 nm
704 nm
700 nm
696 nm
692 nm
688 nm
684 nm
680 nm
676 nm
672 nm
668 nm
664 nm
Photon counts
4000
3000
2000
1000
0
0.0
0.1
0.2
0.3
0.4
0.5
tm [ns]

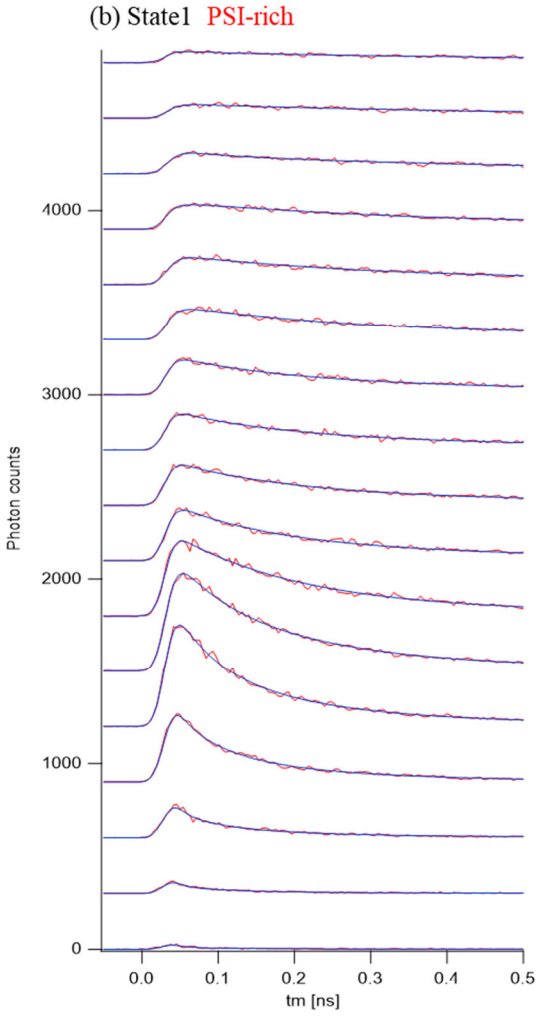
(b) State1 PSI-rich
Photon counts
4000
3000
2000
1000
0
0.0
0.1
0.2
0.3
0.4
0.5
tm [ns]

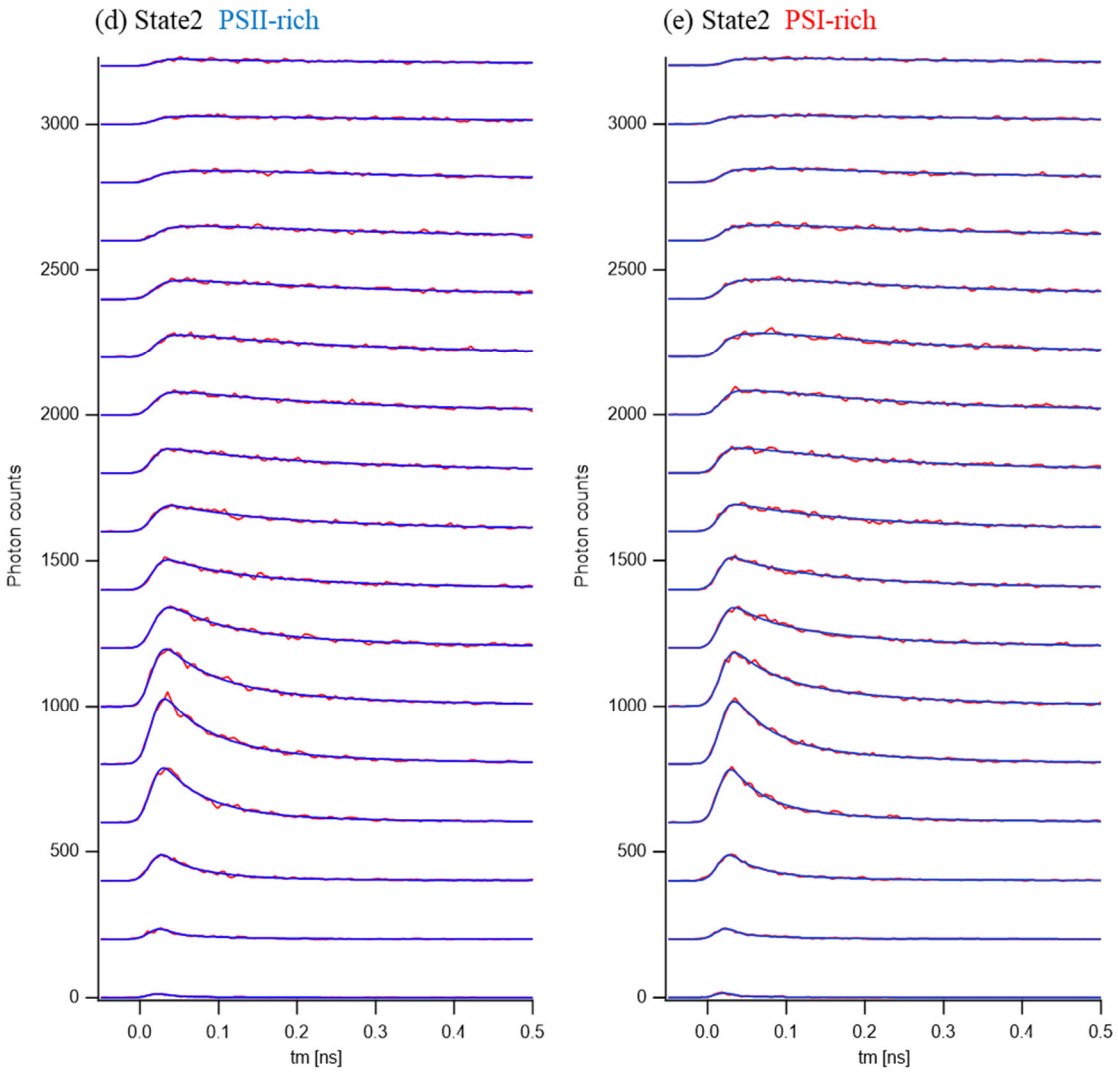

Figure 4-6 (a) The accumulated streak image which is the same as that displayed in Fig. 4-5 (c). The streak image was divided into 17 segments represented by the white lines. The 17 decay curves were obtained by integrations along the wavelength axis in the segments. They are displayed as red solid lines in panels (b) (state1, PSII-rich), (c) (state1, PSI-rich), (d) (state2, PSII-rich), and (e) (state2, PSI-rich). Blue solid lines represent the fitting curves with sum of four exponential decay models.

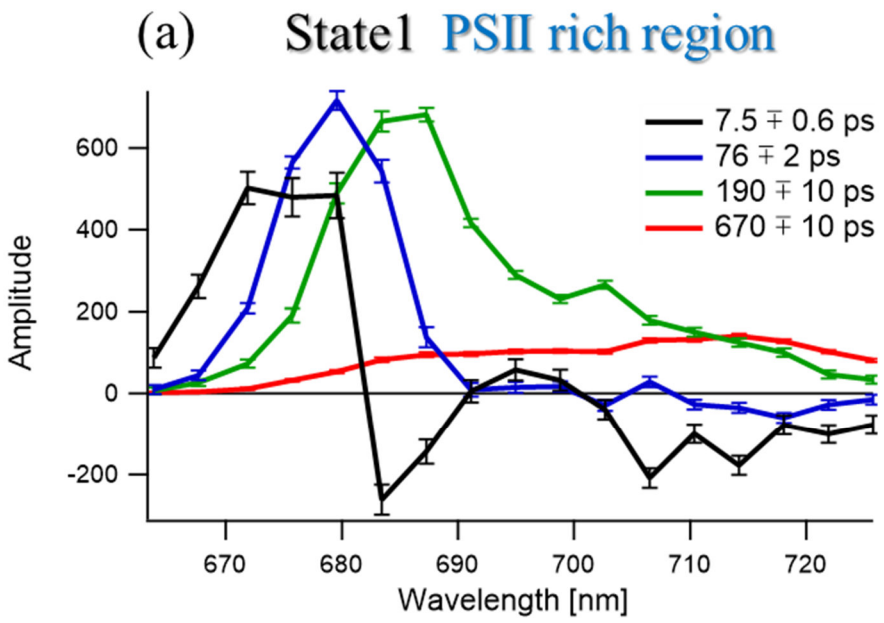
(a) State1 PSII rich region
7.5 ∓ 0.6 ps
76 ∓ 2 ps
190 ∓ 10 ps
670 ∓ 10 ps
Amplitude
600
400
200
0
-200
670
680
690
700
710
720
Wavelength [nm]

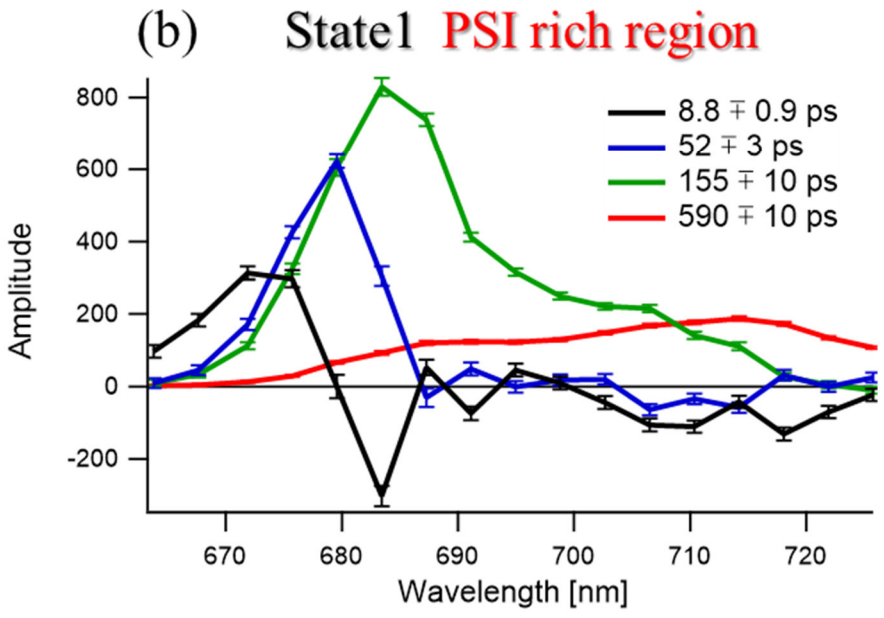
(b) State1 PSI rich region
8.8 ∓ 0.9 ps
52 ∓ 3 ps
155 ∓ 10 ps
590 ∓ 10 ps
Amplitude
800
600
400
200
0
-200
670
680
690
700
710
720
Wavelength [nm]

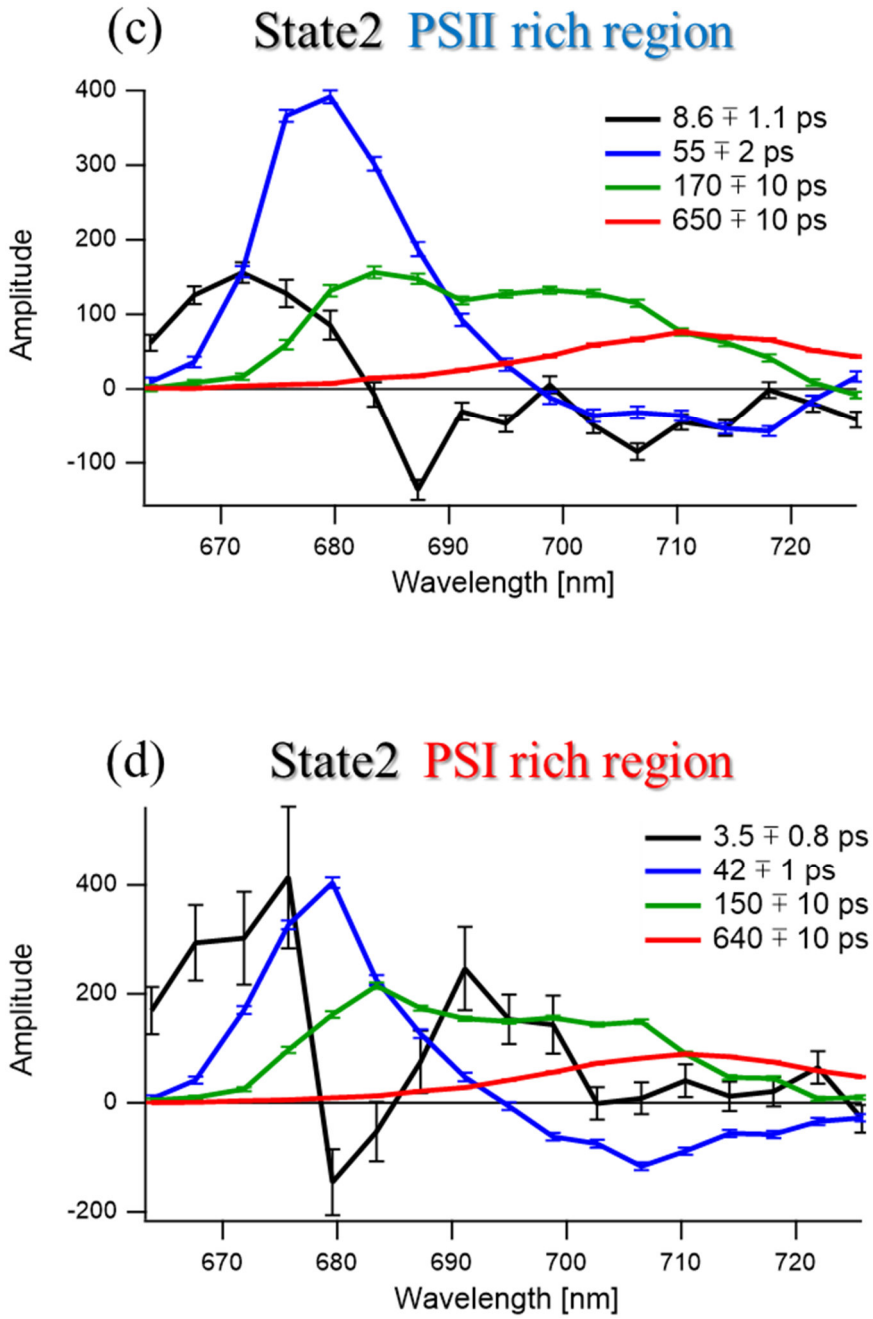

Fig. 4-7 Decay associated spectra calculated for the intracellular PSII-rich (a) and PSI-rich (b) regions in state1 and PSII-rich (c) and PSI-rich (d) regions in state2. Black, blue, green and red solid lines show the spectra associated with the indicated time constants. The error bars and values of the right of ∓ synbols in the annotation indicate the standard error of the global fitting with the exponential decay model.

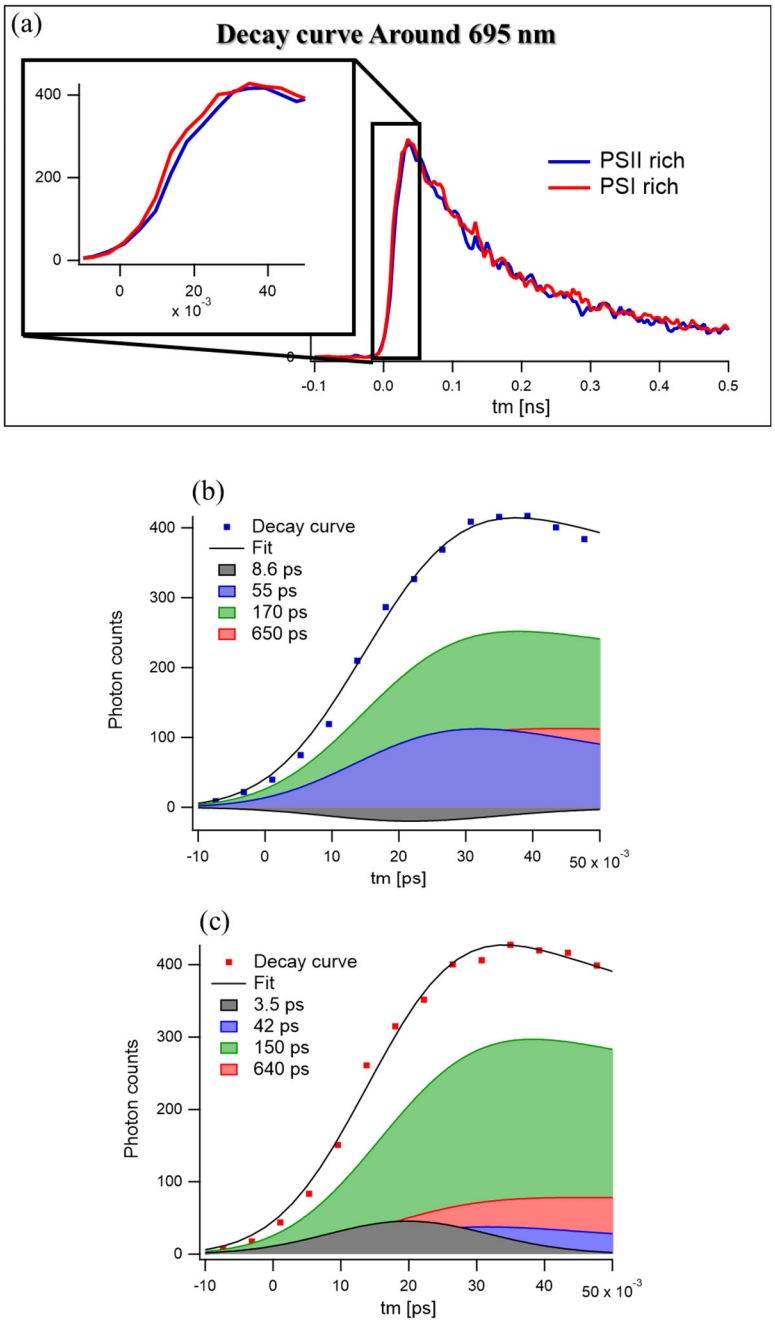

Fig. 4-8 (a) Fluorescence decay curves obtained by integrating around 695 nm of the streak images for the PSII-rich (blue) and PSI-rich (red) in state2 regions. Blue dots in panel (b) and red dots in panel (c) are the same ones as the red and blue solid lines in panel (a), respectively. These two decay curves were fitted to sum of four exponential models. Black lines in panels (b) and (c) shows the fitting curves. The curves filled by black, blue, green, and red, represent the four exponential decay components with the time constants given in the annotations.

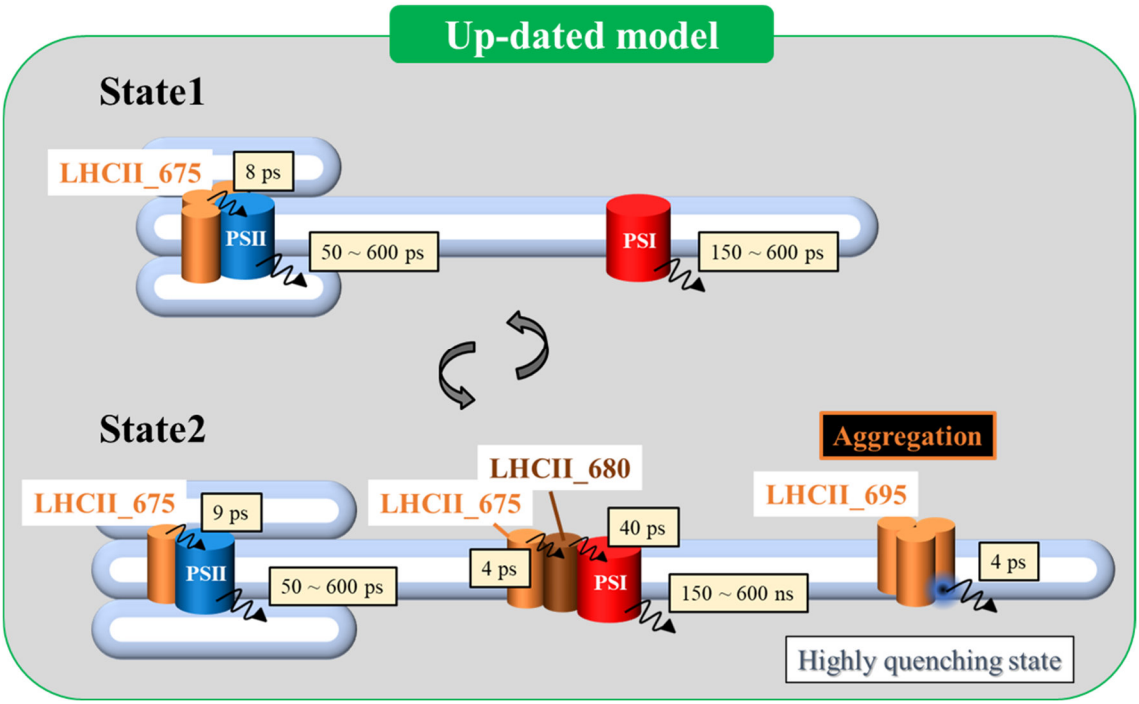

Fig. 4-9 Updated state-transition model. The apparent time constants of the excittaion energy transfers from LHCII to PSs and fluorescnece emission from PSs are represented. In this model, a part of LHCII moves from PSII to PSI upon state transitons. In addition, LHCII aggregations with red-emitting and highly quenching states are formed near PSI.

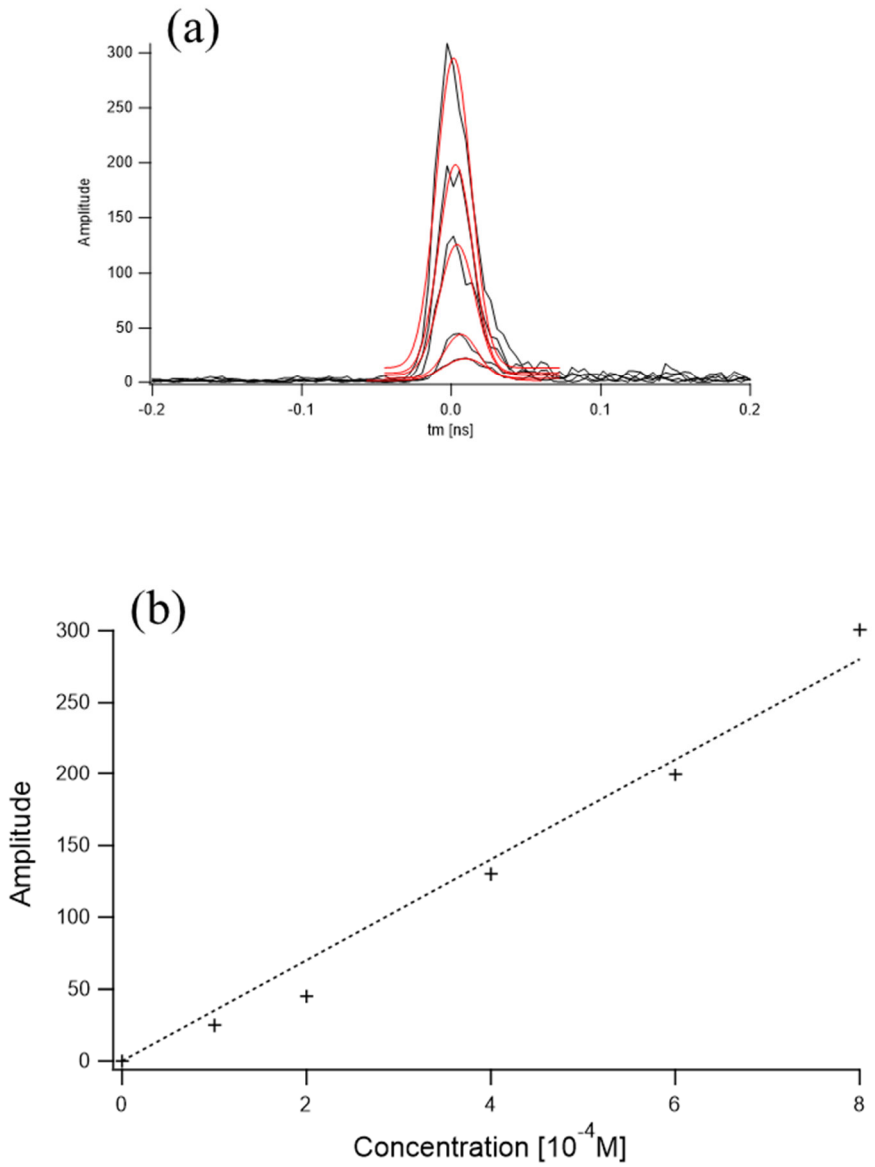

Figure 4-10 (a) Fluorescence decay curves of a malachite green aqueous solutions with several concentrations (black solid lines) and fitting curves to single Gaussian function (red solid lines). These curves were measured with the cryogenic streak camera optical system. (b) Amplitude of the fluorescence decay of a malachite green aqueous solution estimated by the fitting is plotted against its concentration. The cross points show the measured data, and the dashed line indicates the linear approximation.

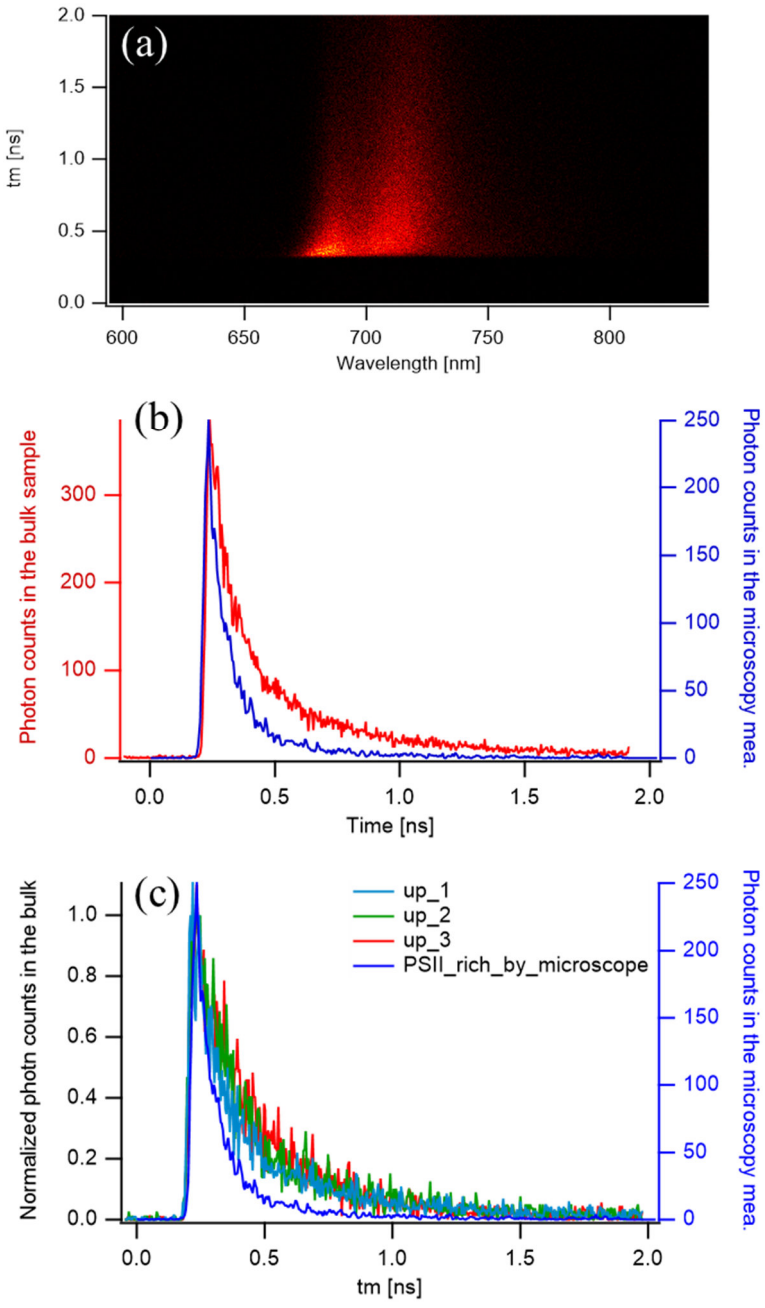

Figure 4-11 (a) Streak image measured for a bulk-*Chlamydomonas* suspension at 80-K. (b) Red slod line show the fluorescence decay curve integrated from 675 to 685 nm of the streak image in (a). Decay curves integrated over the same range of the streak image in Fig. 4-5 (c) is represented as blue lines in (b) and (c). (c) Fluorescence decay curves extracted from the streak images acquired for the bulk-*Chlamydomonas* suspension with gradually increased temperature (from up_1 to up_3).

Chapter V Development Cryogenic STED Microscope System

5-1 Purpose of This Experiment

As I mentioned in section 2-10, our cryogenic optical microscope system has a spatial resolution with accuracy close to the theoretical value. The effective spatial resolution in the lateral axis was estimated to be 0.37 μm that is equivalent to the size of the stacked membrane region in a chloroplast. On the other hand, the effective spatial resolution in the optical axis was estimated to be ca. 1.3 μm. This insufficient resolution especially in the optical axis direction has prevented us to observe clear segregations of intracellular PSII-rich and PSI-rich regions. STED, one of the super resolution fluorescence microscopy techniques, involves the process of laser scanning over a sample and seems to have a good compatibility with our current microscope. The implementation of STED to our system drastically enhances the resolution without degradation of its ability to obtain information on both the fluorescence spectra and lifetimes of the intracellular specific regions. Recently, we have been developing the cryogenic STED microscope system (Fig. 2-14) and attempting to improve the spatial resolution of our system. I evaluate its performance in this Chapter.

5-2 Optimization of the Delay Stage

A STED microscope employs two light beams, the excitation (Ex.) beam and STED beam that induces stimulated emission as described in section 2-8. To achieve effective stimulated emission, it is essential to synchronize the two laser pulses in time on the sample position. The delay stage (Fig. 2-14) installed on the STED optical path allows us to manually change the optical path length of the STED beam in the range of $\pm$ 30 cm, resulting in the shift of its arrival time in the range of $\pm$ 1 ns.

We estimated the relative time between Ex. and STED pulses by observing the scattering of the two lasers on the paper placed in front of the cryostat (Fig. 5-1 (a)) with the TCSPC module. We observed the signal of the two pulses, and adjusted the arrival time of the STED pulse by moving the delay stage back and forth. The mobile and immobile pulses upon the delay-stage movement were assigned to STED and Ex. beams, respectively. The blue and red solid lines in Fig. 5-1 (b) show the observed two-pulse signals when the delay stage was fixed at two different positions. The annotations of 23 cm and 10 cm in the inset represent the rough distances of the

stage from the position which gave the shortest optical path length of the STED beam. The delay stage was moved 13 cm in the second measurement, resulting in a ca. 0.87 ns shift in arrival time of the STED-beam pulse. As you see, the peak assigned to the STED beam is shifted 0.87 ns as expected.

This method allows us to roughly estimate the relative time between the two pulses of Ex. and STED beams. Note that the FWHM of the measured pulse, which represents the time resolution, is ca. 45 ps, and it is not possible to specify the arrival time of the pulse with higher accuracy than this. The optimum delay stage position for realization of an effective stimulated emission should be determined by the actual depletion efficiency for a standard dye while adjusting the delay stage.

5-3 Effective Donut Shape of the STED Beam

The vortex phase plate (VPP), a diffractive optical element, was implemented to convert the STED beam with a Gaussian profile to the donut-shaped one. A shape of the STED beam was measured at the place marked with a green cross in Fig. 2-14 by a C-MOS camera with and without the VPP put after the optical fiber. As shown in Fig. 5-2, the donut-shaped beam was significantly distorted. In addition, at present, we have not succeeded in observing donut-shaped STED beam on the sample surface where the beam is focused. The previously reported study has achieved to improve the spatial resolution beyond the diffraction limit even with the slightly distorted STED beam [67]. In this study, the ratio of central intensity to maximum intensity ($I_{\mathrm{center}}/I_{\mathrm{max}}$) of the STED beam was estimated to be ca. 0.16. Our donut shaped STED beam exhibited a close value (0.154 and 0.156 for x and y axes, respectively) of the effective $I_{\mathrm{center}}/I_{\mathrm{max}}$ to the above value. The effective $I_{\mathrm{center}}/I_{\mathrm{max}}$ was estimated from the average of those estimated from the cross-sectional intensity distributions (red and yellow solid lines in Fig. 5-2) along x and y axes of the obtained donut-profile image. This suggests that even the current STED beam is expected to improve the spatial resolution to some extent.

5-4 Evaluation of the Laser Power Dependence

Figure 5-3 (a) shows the fluorescence decay curve of the ATTO647N thin film detected by TCSPC at room temperature. The blue, red, and green solid lines were obtained with the irradiation of only Ex pulse, only STED pulse, and both two pulses, respectively. In this

experiment, the STED pulse was irradiated 0.2 ns after the arrival of the Ex. pulse. The laser powers of the Ex. and STED light were 0.12 uW and 2.0 mW, respectively. Although the decay curve obtained with the irradiations of both light (green solid line in Fig. 5-3 (a)) was expected to drop just after the arrival of the STED pulse by the induced stimulated emission, unexpected ascent of the fluorescence signals was observed at the incidence of the STED pulse. In addition, the nonnegligible signal was detected even when only the STED pulse was irradiated (red solid line in Fig. 5-3 (c)). This suggested that the STED light electronically excited molecules rather than deexcited them via the stimulated emission. There are two possible excitation mechanisms: one-photon excitation from vibronic bands in the electronic ground state (anti-stokes excitation) and two-photon excitation to higher two-photon-allowed levels.

Note that the transition rate of a two-photon excitation is proportional to the square of the excitation light intensity. To elucidate the contribution of the two-photon excitation, we measured the excitation-intensity-dependence of the STED-light-induced fluorescence decay curve of the ATTO647N thin film (Fig. 5-3 (b)). The intensities of the STED light are indicated in Fig. 5-3(b). The linear relationship in Fig. 5-3(c) ruled out the occurrence of the two-photon excitation.

Figure 5-3 (d) shows the fluorescence decay curves obtained under the same conditions as in Fig. 5-3 (a), except that the power of the Ex. light was multiplied by 100. The decay curve with both light irradiation (green solid line in Fig. 5-3 (d)) exhibits ca. 50 % drop of the fluorescence signals just after the arrival of the STED pulse, indicating the depletion by the stimulated emission. The occurrence of the stimulated emission can be interpreted based on the Jablonski *diagram consisting of the four levels*; the electronic ground (ν_0) and excited (ν_0^*) states and their vibronic states (ν_1, and ν_1^*). In general, the stimulated emission from ν_1 to ν_0^* compete with anti-stokes excitation from ν_0^* to ν_1. The transition rates of the stimulated emission and anti-stokes excitation are proportional to the occupation number of ν_0^* (N_0^*) and ν_1 (N_1), respectively. Therefore, an occupancy inversion ($N_0^* > N_1$) is required to achieve the effective stimulated emission. In a typical STED microscope, Ex. laser with a sufficient power ensures N_0^* to exceed N_1 which is a relatively small according to the Boltzmann distribution. When we obtained the decay curve in Fig. 5-3 (a), the power of Ex. light was not enough to realize the above occupancy inversion, resulting in a significant increase, instead of a drop, of the fluorescence signal by the STED pulse. Actually, Ex. light power used for the measurement in Fig. 5-3 (a) was almost 100

times weaker than that applied to the previously reported system which achieved the effective fluorescence depletion [65].

Note that green solid line in Fig. 5-3 (d) exhibit decrease of fluorescence signal as compared with the blue line even in the time region before the STED pulse arrival. The measurement with Ex. + STED light irradiation was performed after that with only the Ex. beam irradiation. We assume that photobleaching occurred during the measurement due to the increased Ex. beam power. Accumulation of excited state due to the longer lifetime than the pulse interval may be another cause for the decrease in fluorescence before the STED pulse arrival. In general, placing the sample in a vacuum inhibit the generation of reactive oxygen species (ROS). In fact, as described in the next section, this fluorescence dissipation was not observed in the measurements where the sample was imposed in the vacuum condition in conjunction with the cryogenic manipulation.

5-5 Temperature Dependence of the STED Efficiency

In the previous section, we mentioned that the Ex. light intensity plays a significant role to achieve the occupancy inversion ($N_0^* > N_1$), which is essential for the effective stimulated emission. According to the Boltzmann distribution, the occupancy of the vibronic band decreases at low temperatures, ensuring the above occupancy inversion [82]. We have demonstrated the inhibition of the un-desired anti-stokes excitation upon the cryogenic treatment.

Figure 5-4 (a, b) shows the fluorescence decay curves of ATTO647N thin film measured at 84 K and room temperature. Powers of Ex. and STED beams were 2.0 μW and 5.0 mW at sample position, respectively. Here, we did not apply a sufficiently high power of the Ex. beam assuring the occupancy inversion in order to highlight the effect of sample temperature. The exposure time of each decay curve was 1 s. Although, the irradiation of the STED light at room temperature caused the significant increase of the signal due to the anti-stokes excitation as in Fig. 5-3 (a), the depletion of the fluorescence was observed at low temperature. In this measurement, the series of measurements of the three decay curves with Ex. light only, STED light only, and both was performed several times while decreasing the temperature (not all data not shown). Figure 5-4 (c) shows the relative amplitudes of the decay curves only with the STED pulse against those only with the Ex. pulse plotted vs. the temperature, highlighting the reduction of the anti-stokes excitation at low temperatures. This result clearly indicated that the low-temperature

treatment promotes the effective stimulated emission by suppressing the occupancy of the vibronic band.

Although the data in Fig. 5-3 and 5-4 were obtained with the same samples, the behaviors of the decay curves are clearly different from each other. Since the sample was prepared by the spin coating, the concentration of the dye may be non-uniform on the sample surface. We assumed that the inhomogeneous lifetime was caused by the site-dependent self-quenching due to the local formation of aggregates.

5-6 Trials with Fluorescent Beads – Non-Donut Shaped STED Beam

The depletion of fluorescence due to induced emission was observed by increasing the Ex. power and lowering temperature. However, only ca. 50 % of the fluorescence was dissipated at this time whereas, ca. 70 % of that has been achieved in a previously reported study [ref]. One possible factor is that the focal spots of the Ex. and STED beams were not spatially overlapped. To confirm this, we identified the focal positions of the two lasers through scanning the fluorescent beads.

Images in Figure 5-5 (a, b) represent the fluorescence images of fluorescent beads F8807 measured at room temperature and 80 K. One bead was scanned three times with irradiation of Ex. light only, STED light only, and both. The powers of Ex. and STED light which was not donut shaped were 8.0 μW and 6.8 mW at the sample position, respectively. The images in Fig. 5-5 (a) and (b) are depicted in the same color scales. Although the scanning ranges of the three images obtained in the series of measurements are common, the positions of the bright spots under irradiation of Ex. light only and STED light only are slightly shifted, indicating that the two beams do not overlap finely. Since the TCSPC module was applied as the detector, a fluorescence decay curve was obtained for every pixel of the image. The decay curves on the right of the images in Fig. 5-5 show those obtained at the center of the bright spot for the three irradiation conditions. At room temperature, the effective fluorescence depletion was not observed due to the insufficient population inversion as discussed in the previous section (green solid line in Fig. 5-5 (a)). Surprisingly, nearly 80% of the fluorescence depletion was achieved in the center of the bright spot at 80 K (green solid line in Fig. 5-5 (b)). On the contrary, only ca. 40 % of the fluorescence reduction was obtained at a pixel located at the edge of the bright spot (black solid line in Fig. 5-5 (b)). Note that, in the measurement of the thin film sample described in the previous section, it

is suspected that the fluorescence from the peripheral region of the Ex. beam spot was not sufficiently depleted due to the deficient STED beam intensity. We assumed that the ineffective stimulated emission in the outer region resulted in the observation of the less pronounced fluorescence drop in the measurement for the thin film sample.

5-7 Trials with Fluorescent Beads – Donut Shaped STED Beam

When STED effect is operating, irradiation of the STED light with the donut shape suppresses the fluorescence emission from the peripheral region of the excitation volume, resulting in the improvement of the spatial resolution. To confirm the STED effect, the STED beam was transformed into the donut shape by installing the VPP after the acquirement of images of the bead shown in Fig. 5-5 (b), and the bead was rescanned three times with Ex. light only, STED light only, and both (images in Fig. 5-5 (c)). The image with both irradiations does not exhibit the reduction of the bright spot size. Despite the expectation, the fluorescence depletion was observed even in the center of the bright spot where the STED beam should have no power in the ideal condition. This was probably because the STED beam did not form a symmetric donut shape on the sample position and/or because the focus positions of STED and Ex. beams did not match to each other. As I described in section 5-3, the STED beam had a distorted donut shape before the cryostat, and besides we have not yet succeeded in capturing a donut-shaped STED beam at the sample position. F8807 is not a suitable fluorescent bead for evaluating the shape of the STED beam due to their tiny absorbance at the wavelength of the STED light, resulting in the faint bright spot even at room temperature (images only with the STED beam irradiation in Fig. 5-5). Previously reported studies have used gold nanoparticles or beads with sufficient absorption at the STED-light wavelength for visualization of the shape of the STED beam [65, 67]. Our next challenge is to establish a method to evaluate the shape of the STED beam on the sample surface by employing these or other methods.

5-8 Advantages and Disadvantages of Operating STED at Low Temperature

The effectiveness of performing STED at low temperature is as follows.

1) Reduction of the photobleaching.
2) Enhanced versatility.
3) Improvement of spatial resolution by arbitrarily increasing the STED intensity.

In this experiment, we have realized the population inversion even at low Ex. light power by lowering temperatures. This means that the intensity of the Ex. light can be suppressed in the cryo-STED [82, 83] and the flexibility of the selection of the Ex. wavelength is increased. Furthermore, the decrease in the population of the vibronic band in the ground-state leads to the inhibition of the anti-stokes excitation, allowing the use of higher intensity of the STED beam. As shown in Eq 2-3, the spatial resolution of the STED is determined by the intensity of the STED beam, which indicates the enhancement of the spatial resolution by the increased STED power.

Previously reported study has suggested that low sample temperature induce an increase in the occupancy of the triplet state due to a deceleration of non-radiative deactivation of that state. It reduces a conventional fluorescence and the S/N ratios of the bright spots, resulting in a poor spatial resolution. This problem was solved by introducing a third laser inducing the triplet depopulation thorough a direct stimulation of a transition from the triplet to higher excited states [82].

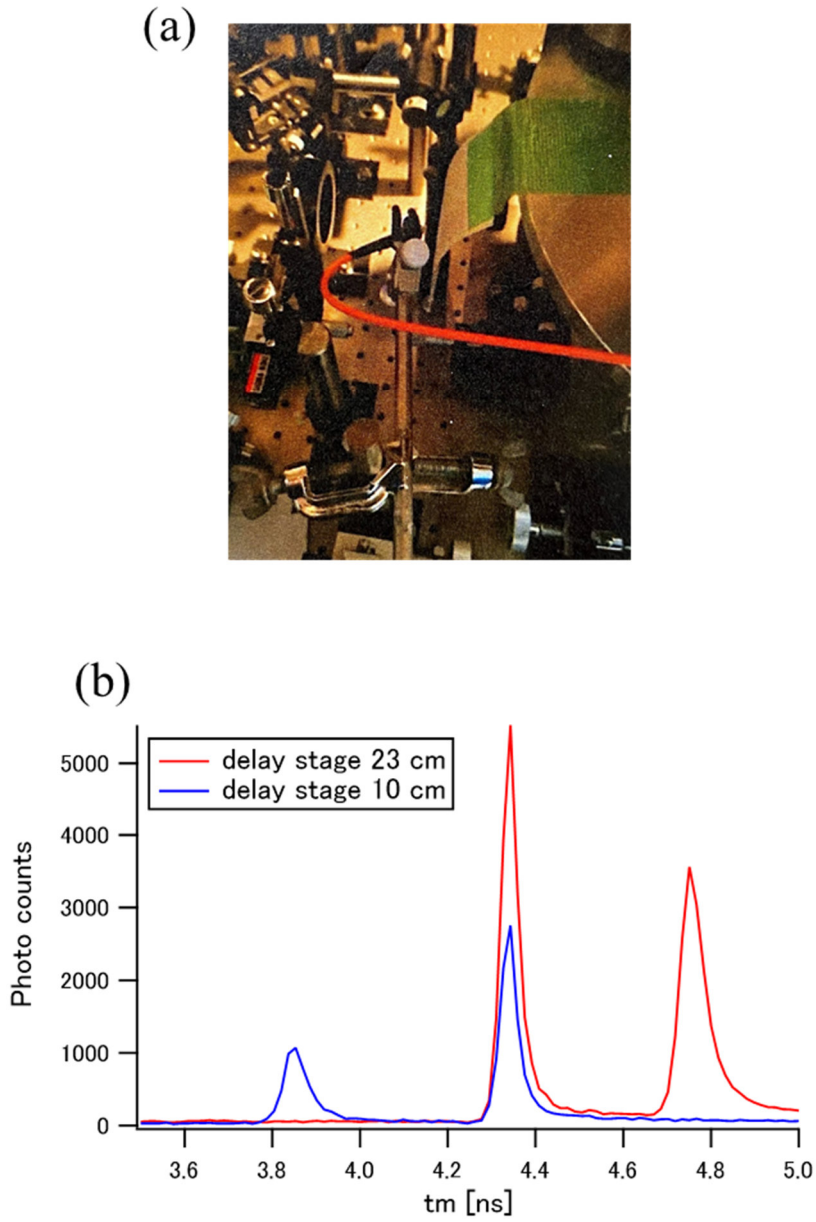

Figure 5-1 (a) A picture of the setup of the optical fiber connected to the APD for the measurements of the pulse timings of Ex. and STED light. Scattered light from a sheet of paper placed in front of the cryostat was detected by the APD which fed photon signals to the TCSPC module. (b) The obtained two pulse sequences measured with changing the position of the delay stage. The position of the delay stages measured from the edge are indicated.

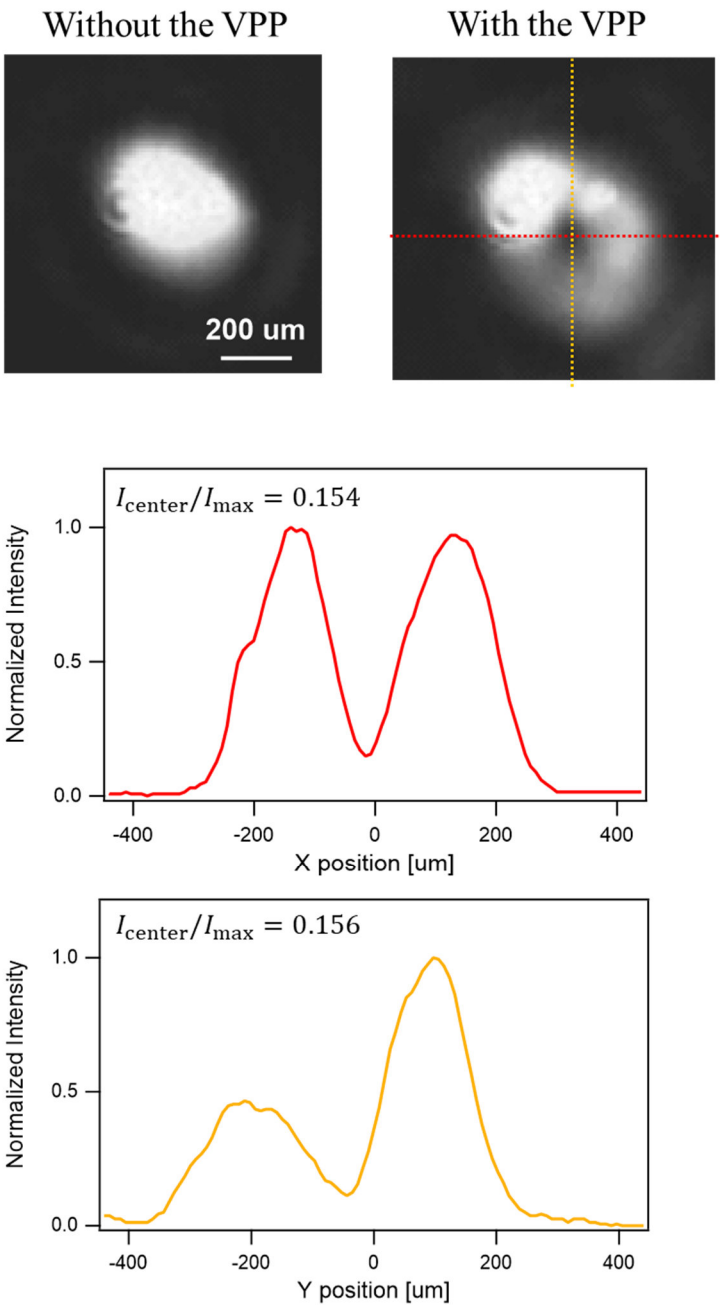

Figure 5-2 Upper images show the intensity distributions of the STED beam measured by the C-MOS camera at the place marked with green cross in Fig. 2-10 with (right) and without (left) the VPP. Middle and bottom panels show cross-sectional intensity distributions cut along the red and yellow dotted lines in the image of "with the VPP", respectively. The estimated I_{center}/I_{max} values are given on the graphs. In this estimation, we took the I_{max} of the curve in the bottom panel for the calculations of I_{center}/I_{max} for both traces.

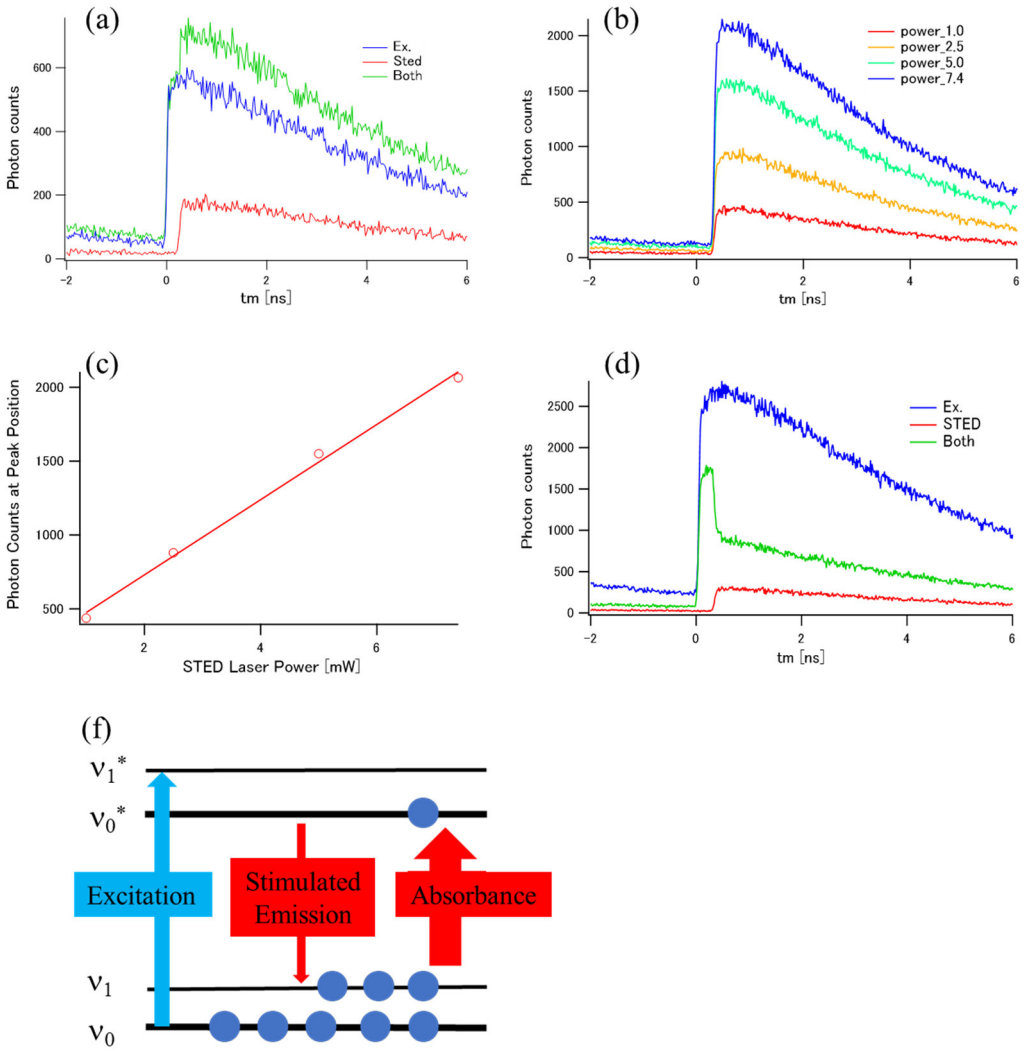

Figure 5-3 (a) Fluorescence decay curves of the ATTO647N thin film detected by the TCSPC module of the cryogenic STED microscope system. Green, red, and red curves were obtained when the sample was irradiated with Ex. light, STED light, and both, respectively. (b) Fluorescence decay curves of the ATTO647N solution obtained with the STED light irradiation. The data were taken with various powers of the STED light. (c) The peak intensities of decay curves in (b) plotted vs. the STED power. (d) Fluorescence decay curves of the ATTO647N solution measured under the same conditions as (a) except for the 100-times increased Ex. light power. (e) A schematic illustration showing the competition between the stimulated emission and the anti-Stokes excitation depending on the occupancy of the excited and ground states.

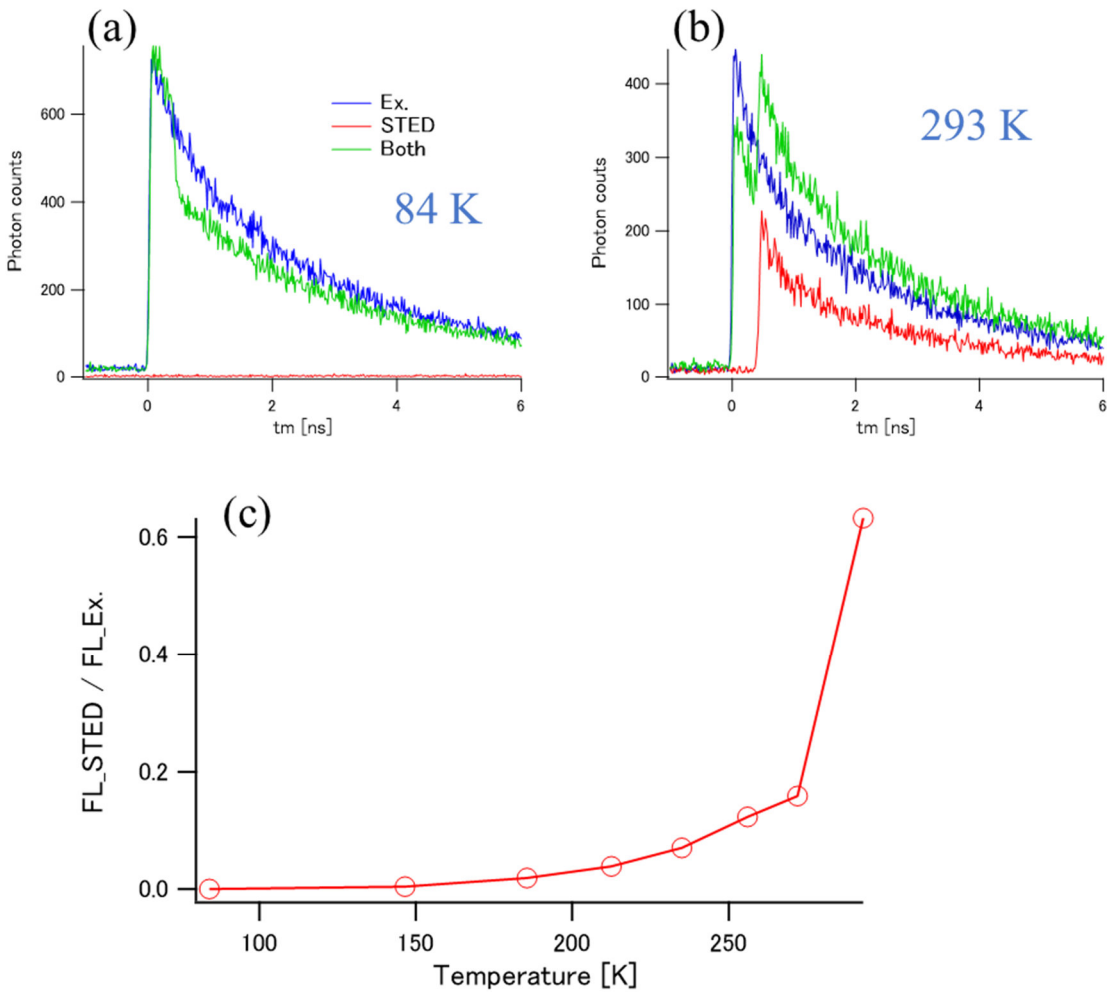

Figure 5-4 Fluorescence decay curves of the ATTO647N thin film at 84 K (a) and 293 K (b). (c) The relative amplitudes of the decay curves only with the STED pulse with respect to those only with Ex. pulse are plotted against the temperature.

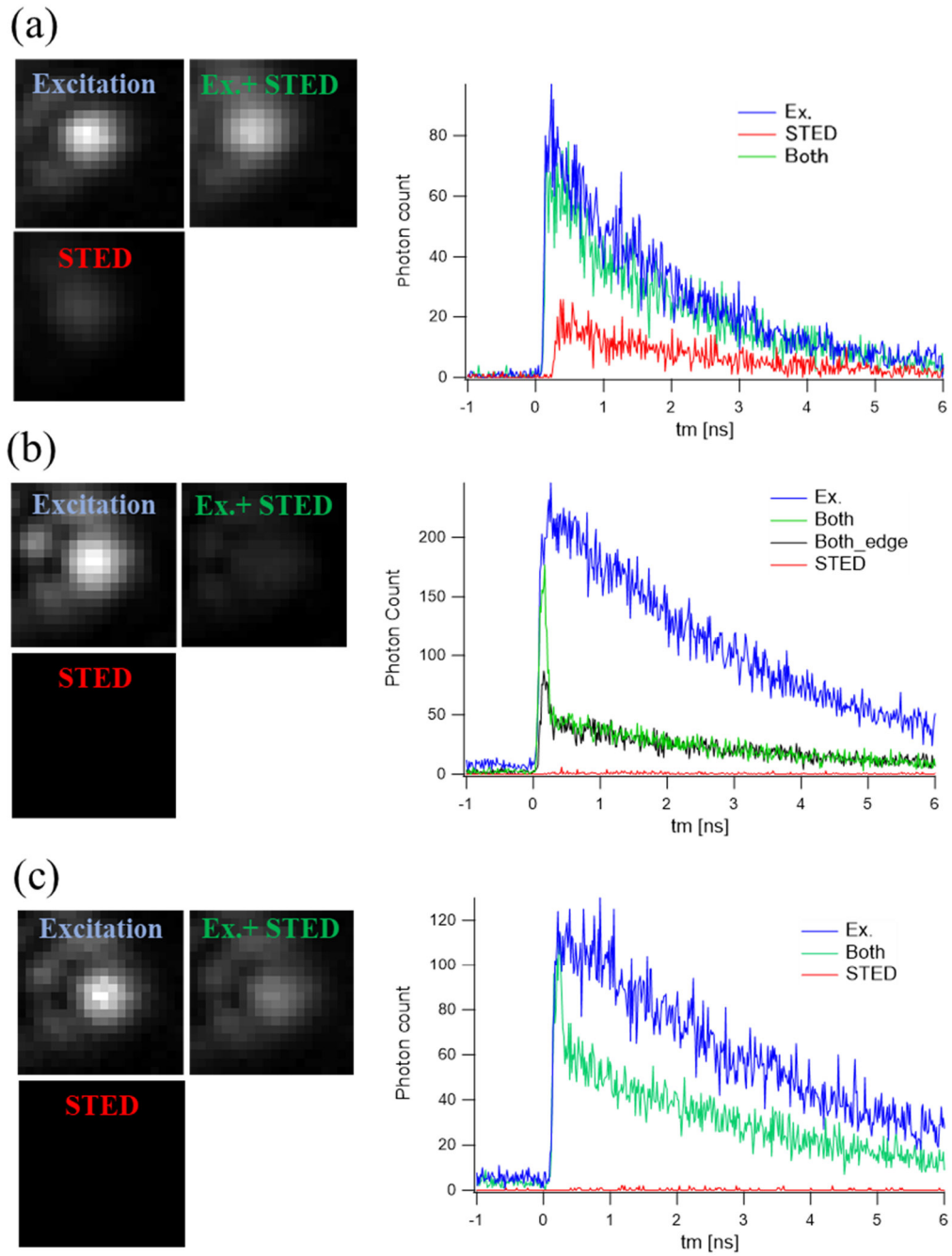

Figure 5-5 Fluorescence images and decay curves of fluorescent beads F8807 obtained at room temperature (a) and 80 K (b, c). Data in (a, b) were measured with the non-donut-shaped STED beam, whereas those in (c) were measured with the donut-shaped STED beam. Each decay curve was obtained with the laser spots fixed at the center pixel of the bright spot. The decay curve represented as black solid line in (b) was obtained at a pixel located at an edge of the bright spot.

Chapter VI Photosynthetic Artificial Membrane

6-1 Purpose of This Experiment

I have started the collaborated research with Assoc. Prof. Morigaki group at Kobe university where they are trying to establish an artificial photosynthetic membrane. Very recently, Morigaki and co-workers have developed a new type of “hybrid membrane” by incorporating thylakoid components into supported lipid bilayers within array-patterned template (patterned membrane) [69, 70]. Although they succeeded in observing a homogeneous and colocalized distribution of the Chl fluorescence within the patterned membrane, there is a lack of evaluation for the activity of the reconstructed photosynthetic components in the hybrid membrane in terms of photophysics and photochemistry such as the energy transfer and the NPQ. By measuring the hybrid membrane with our cryogenic optical microscope system, we have attempted to evaluate the function of the incorporated photosynthetic proteins. In the future, we plan to investigate the fluidity of mobile-LHCII within the thylakoid membrane and perform a single molecule spectroscopy of a photosynthetic protein within the artificial thylakoid membrane providing a controlled environment.

6-2 Observation of Patterned Membrane

Figure 6-1 (a, b) show typical fluorescence images of the patterned polymeric bilayer (Diyne-PC) formed on a quartz substrate. The image was obtained by the standard confocal cryogenic optical microscope system as shown in section 2-5 at room temperature. The power of excitation light (445 nm, CW) was 80 μW before the cryostat, and the exposure time was 0.05 s. The images represent the lattice-like patterned polymeric bilayers, termed as “frame region”, serving as a framework of an array of 20 μm × 20 μm square-shaped empty spaces. Since the CCD camera was used as a detector, a fluorescence spectrum was acquired at every pixel of the image. Figure 6-1 (c) shows the fluorescence spectra averaged over pixels surrounded by the green (empty region) and blue squares (frame region) in Fig. 6-1 (b). Slight fluorescence signals from the polymer was observed even in the empty region where the polymer was not expected to exist. It indicates that the non-polymerized Diyne-PC was not fully removed during the rinse process described in section 2-3.

Figure 6-1 (d) shows the normalized fluorescence spectra obtained from the frame

region while varying the sample temperature from room temperature to 80 K. While the spectrum of the polymer shifted to longer wavelengths by lowering the temperature to 207 K, the spectral appearance remained constant upon further cooling below this temperature. Although the origin of fluorescence from the polymer has not been fully clarified, the most plausible idea is the π-π* transition within a π-conjugated system (established by the covalent bonds between the neighboring lipid molecules) spread over a polymer domain of a certain size. Since the membrane was immersed in the buffer solution, we assume that the freezing of the solution forces a change in the arrangement of the solvent molecules around the lipids, resulting in the spectral shift. In addition to this shift, the fluorescence intensity also increased about 30-fold by the low-temperature treatment (data not shown). The mechanism for this fluorescence enhancement upon cooling is not clear at present.

6-3 Observation of Patterned Hybrid Membrane

Figure 6-2 (a, i) show typical fluorescence images of the hybrid membrane composed of the mixture of the thylakoid membrane + DOPC incorporated within the empty region of the patterned polymeric bilayers. The data was measured with the standard confocal cryogenic optical microscope system at 80 K. The incorporating process was done in our laboratory following the procedure described in section 2-3. The power of the excitation light and the exposure time were the same as those in section 6-2. The green solid lines in Fig. 6-2 (g, o) represent the fluorescence spectra averaged over the regions specified by the green squares in Fig. 6-2 (a, i). There is a remarkable peak around 680 nm in addition to the polymer fluorescence as in Fig. 6-1 (c). If a natural photosynthetic system was successfully incorporated, the membrane formed within the empty spaces of the polymer should include the following pigment components: LHCII, PSII, PSI, and NBD-PE (labeling dye for the DOPC). To decompose the fluorescence signal in each pixel into these components, we conducted a global Gaussian decomposition. To do this , we calculated the fluorescence spectra averaged over all regions within the spaces between the frames, termed as “surrounded region”, roughly specified by the green squares in Fig. 6-2 (a, i), of the measured five hybrid-membrane images. They were globally fitted to sum of four Gaussian functions (orange, blue, red, and gray fills in Fig. 6-2 (g, o)) and the model spectrum for the Diyne-PC (spectra filled with black hatched lines in (g, o)). In this fitting, the parameters of the model for the Diyne-PC were fixed to those determined by the fitting in Fig. 6-1 (b) except for

the amplitude set free to vary. The obtained peak wavelength and FWHM of each Gaussian component are listed in Table 6-1.

We conducted the fitting of the spectra at all the pixels in the fluorescence image of the hybrid membrane to the model described above, in which only the amplitudes of the Gaussian components were allowed to vary whereas the peak positions and widths were fixed to the values determined by the above global fitting. Then, fluorescence images were reconstructed with the areas of the obtained Gaussian functions and the spectrum at every pixel of the image (Fig. 6-2 (b-f and j-n)). Each Gaussian component was assigned as indicated in Fig. 6-2 (h).

As expected, the fluorescence signals assigned to the DOPC and the polymer occupied the space surrounded by the frame and the frame region, respectively. This indicates that the DOPC was uniformly incorporated into the empty region of the polymer.

The Gaussian function named G1 exhibits relatively high amplitude (orange fills in Fig. 6-2 (g, o) and its intensity distribution map allow us to estimate its localization to the surrounded region and several bright spots that emerged only in Fig. 6-2 (b, c, d). At present, we assume that these bright spots are versicles of thylakoid membrane adsorbed on the hybrid membrane due to insufficient rinse. The previously reported study demonstrated that the fluorescence lifetime around 680 nm band was ca. 4 ns [69]. We assumed that G1 component with relatively high fluorescence intensity was mainly contributed from free-LHCII or isolated Chl, which was formed via the influx into the different membrane environment, DOPC. They lost the photochemical quenching channel via the energy-transfer to the reaction center.

The G2 component assigned to PSII fluorescence was rarely detected in the fluorescence spectrum and its intensity distribution map generated from the hybrid membrane where no bright spots are seen (Fig. 6-2 (o, k), respectively). Comparing images (c) and (k) in Fig. 6-2, we found that this component was mainly localized in the bright spot areas, suggesting the inefficient incorporation of PSII into the system. The G3 component was assigned to PSI. The distribution of this component indicated that PSI was uniformly populated within the inside of the polymer frame not only in the bright spots.

Based on the above results and discussions, we propose an extended kinetic model for the incorporation of thylakoid components into the pattered polymeric lipids (Fig. 6-3). We extend the previously reported model: during the incorporation process, the DOPC bilayers is rapidly formed within the empty region of the polymer membrane. The thylakoid membrane associates

with the defective site of the DOPC bilayers, then the photosynthetic proteins flow into those bilayers [69]. Our result suggested that PSI rather effectively enters into the DOPC, whereas PSII incorporation is inefficient. We assume that exposure of the thylakoid components to a different membrane environment will promote chlorophyll dissociation or LHCII disaggregation. In addition, we suppose that the multi-stacked structure of grana makes it difficult to access the defective site of the DOPC bilayers due to its three-dimensional obstacles, resulting in the inability of PSII to flow into those bilayers.

6-4 Current Challenges and Future Works

The polymeric lipids showed an unexpected increase in fluorescence at low temperatures even in the empty region of the polymer membrane where they should be absent. This extremely broad spectrum and strong emission mask the wavelength band where photosynthetic proteins mainly contribute. This degrades the reliability of the quantitative determinations of the components of PSII and PSI by the fitting. To solve this problem, we plan to use an excitation laser at 633 nm that selectively excites the photosynthetic proteins.

G2 and G3, which are respectively assigned to PSII and PSI components, have relatively poor signals. In addition, the latter may contain the signals from a vibronic band of the G1 and G2 component. In addition to the selection of excitation laser wavelengths as described above, time-resolved fluorescence spectroscopy using the streak camera allows us to identify each component from the viewpoint of the energy transfer pathways. We plan to use the cryogenic optical microscope system coupled with the streak camera, which was described in Chapter 4, to evaluate the function and localization of photosynthetic proteins within the hybrid membrane platform.

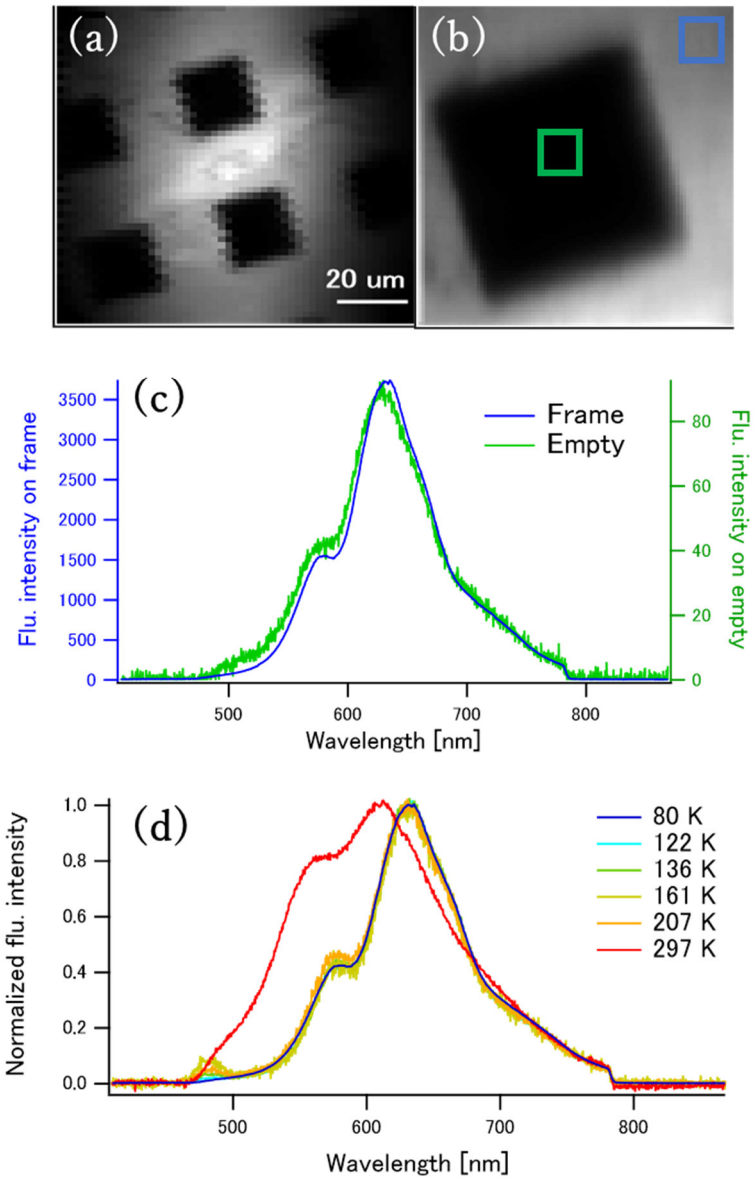

Figure 6-1 Fluorescence images of the patterned polymeric lipids formed on the quartz substrate (a) and that taken by the magnified scan (b). Fluorescence spectra averaged over the regions specified by the green and blue squares in (b) are shown by the same-colored solid lines in (c). (d) Temperature dependence of the fluorescence spectra of the patterned polymeric lipids from 80 K to room temperature. The excitation was made by the 445-nm CW laser.

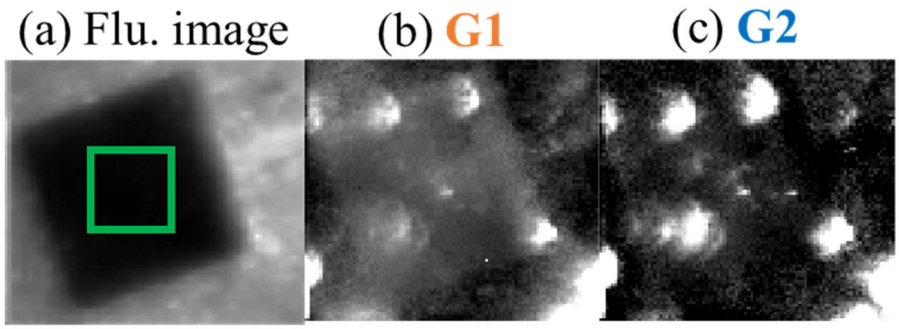

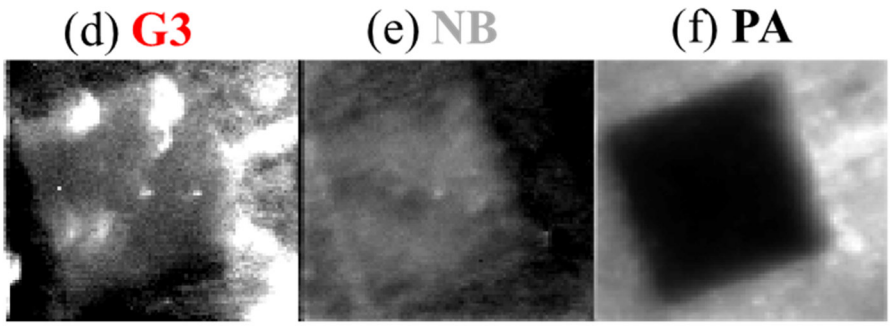

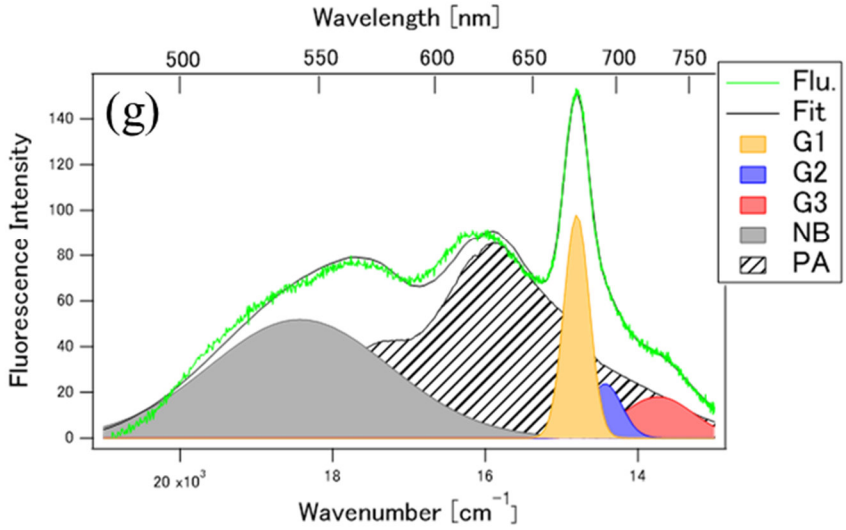

(h)

G1 : LHCII or isolated chlorophyll
G2 : PSII
G3 : PSI
NB : DOPC (NBD-PE)
PA : Patterned membrane (Diyne-PC)

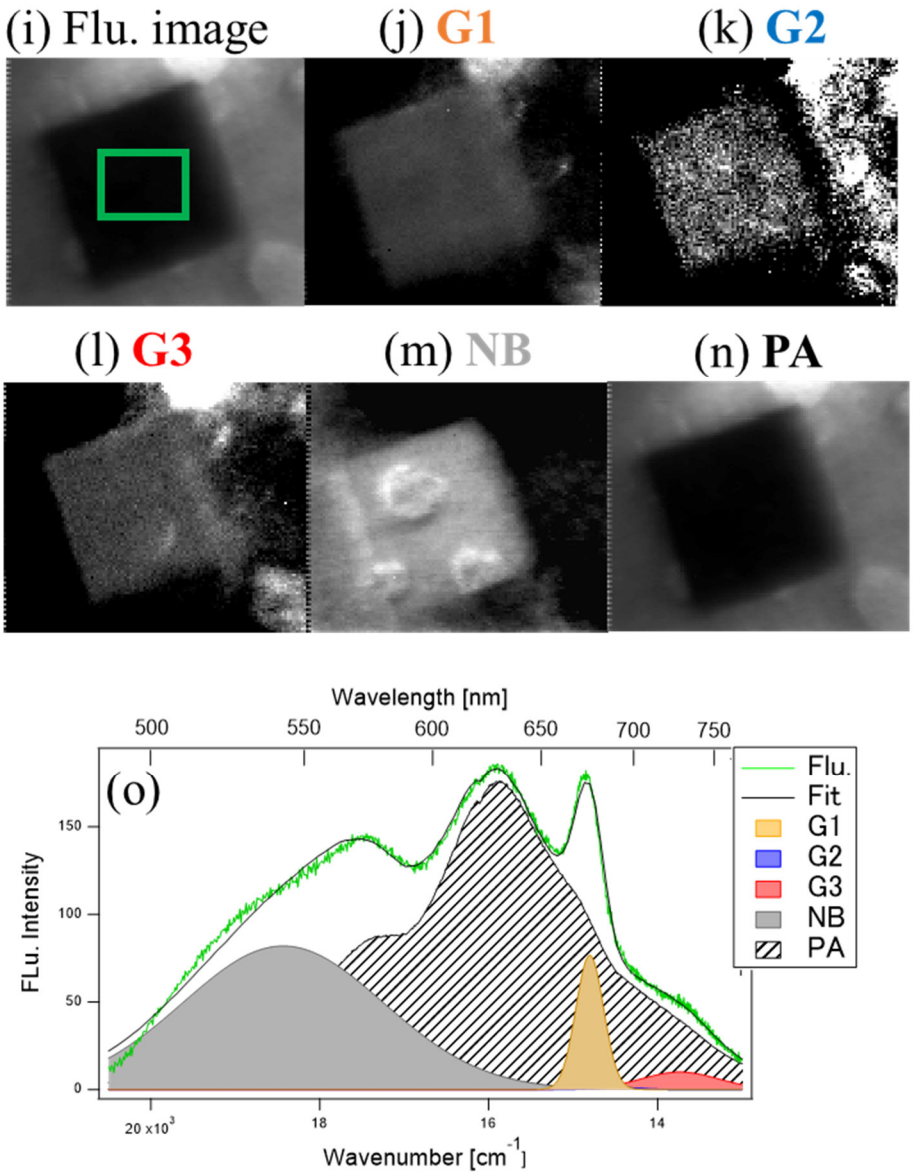

Figure 6-2 Total fluorescence images of the incorporated thylakoid components into the patterned polymeric lipids detected by the polychromator + CCD camera are shown in (a) and (i). From (b) to (f) and from (j) to (n) represent the fluorescence image reconstructed with the G1, G2, G3, NB, and PA components, respectively. (h) List of the assignments for the components identified in the fitting. Green solid lines in (g) and (o) represent fluorescence spectra averaged over the pixels specified by the green squares in (a) and (i), respectively. Black solid lines in (g) and (o) are the fitting curve. The Gaussian functions filled with orange, blue, red, and gray are the component spectra of G1, G2, G3, and NB, respectively.

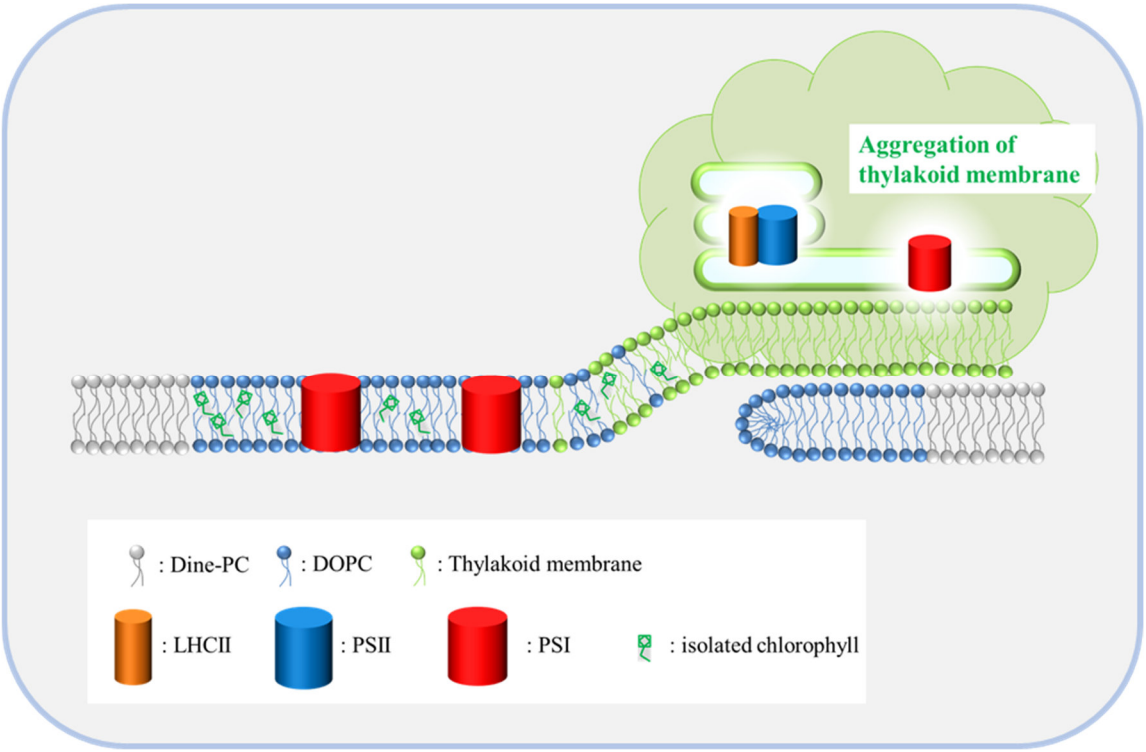

Figure 6-3 A schematic illustration of the proposed model for the incorporations of the thylakoid components into the pattered polymeric lipids. We assumed that PSII has less accessibility to the DOPC bilayer membrane due to the stacked structure of the thylakoid membranes in the grana region.

Table 6-1 The parameters obtained by the global fitting of the spectra averaged over the pixels corresponding the hole regions in each fluorescence image of the incorporated thylakoid components into the patterned polymeric lipids.

	Peak position [nm]	FWHM [nm]
G1	674.8	9.93
G2	690.1	10.4
G3	711.8	78.1
NB	540.1	50.2

Summary

My doctoral research focused on the development of a new optical microscopy system that enables us to observe changes in the distribution and related functions of LHC changing during the state transitions with in vivo experiment. In Chapters III and IV, I described the performance of the novel cryogenic optical microscope system that explores the distribution and function of the LHC in terms of both spectra and lifetime. One of the major research achievements was the identification of the presence of the highly quenched and red shifted LHCII aggregates which colocalized in PSI-rich region upon state2 induction. In addition, we have challenged to develop a STED microscope system that operates at low temperatures to more clearly resolve segregations of intracellular PSII-rich and PSI-rich regions. Although we have confirmed that the low-temperature environment is beneficial to efficient stimulated emission, we could not succeed in improving the spatial resolution, probably due to the low-quality formation of the donut-shaped STED beam at the focal plane. In parallel with the development of the system, we also began collaborative research on the development of a novel model sample with thylakoid membrane arranged on the substrate for easy microscopic observation (Chapter VI).

Improvement in the efficiency of photosynthesis is being focused on as a new revolution to increase crop production to overcome the food crisis that will occur in 2050. Photosynthesis is driven by a multi-step photophysical and biochemical processes starting from the solar-energy absorption and leading to the sugar synthesis. Efforts to improve the various rate-limiting steps are underway around the world [92]. In these efforts, my research is very important to find potential keys to improve the excitation energy supply from the LHC to the PSs. The recent establishment of the Cryo-EM method has had a great impact not only in identifying the structure of photosynthetic proteins with high spatial resolution, but also as a powerful tool to infer the kinetics of the excitation-energy transfer within the photosynthetic supercomplexes [41]. However, the behavior of the LHC in response to the external stimulation, such as state transitions and NPQ, can only be reproduced in an intact chloroplast. I believe that our developed optical microscope system including the model sample will provide a novel in-vivo platform to understand the photophysical and biochemical processes in photosynthesis and to inspire the design of genetically modified crops for improvement of crop production.

References

1. Taiz, L., et al., *Plant physiology and development*. 2015: Sinauer Associates Incorporated.
2. Mullineaux, C.W., *Function and evolution of grana.* Trends in plant science, 2005. **10**(11): p. 521-525.
3. Kirchhoff, H., *Chloroplast ultrastructure in plants.* New Phytologist, 2019. **223**(2): p. 565-574.
4. Gobets, B. and R. van Grondelle, *Energy transfer and trapping in photosystem I.* Biochimica et Biophysica Acta (BBA)-Bioenergetics, 2001. **1507**(1-3): p. 80-99.
5. Van Oort, B., et al., *Effect of antenna-depletion in Photosystem II on excitation energy transfer in Arabidopsis thaliana.* Biophysical journal, 2010. **98**(5): p. 922-931.
6. Dekker, J.P. and E.J. Boekema, *Supramolecular organization of thylakoid membrane proteins in green plants.* Biochimica et Biophysica Acta (BBA)-Bioenergetics, 2005. **1706**(1-2): p. 12-39.
7. Pan, X., et al., *Structural analysis and comparison of light-harvesting complexes I and II.* Biochimica et Biophysica Acta (BBA)-Bioenergetics, 2020. **1861**(4): p. 148038.
8. Stauber, E.J., et al., *Proteomics of Chlamydomonas reinhardtii light-harvesting proteins.* Eukaryotic cell, 2003. **2**(5): p. 978-994.
9. Kubota-Kawai, H., et al., *Ten antenna proteins are associated with the core in the supramolecular organization of the photosystem I supercomplex in Chlamydomonas reinhardtii.* Journal of Biological Chemistry, 2019. **294**(12): p. 4304-4314.
10. Ozawa, S.-I., et al., *Configuration of ten light-harvesting chlorophyll a/b complex I subunits in Chlamydomonas reinhardtii photosystem I.* Plant physiology, 2018. **178**(2): p. 583-595.
11. Minagawa, J. and Y. Takahashi, *Structure, function and assembly of Photosystem II and its light-harvesting proteins.* Photosynthesis research, 2004. **82**(3): p. 241-263.
12. Natali, A. and R. Croce, *Characterization of the major light-harvesting complexes (LHCBM) of the green alga Chlamydomonas reinhardtii.* PLoS One, 2015. **10**(2): p. e0119211.
13. Suga, M., et al., *Structure of the green algal photosystem I supercomplex with a decameric light-harvesting complex I.* Nature plants, 2019. **5**(6): p. 626-636.
14. Shen, L., et al., *Structure of a C2S2M2N2-type PSII–LHCII supercomplex from the green alga Chlamydomonas reinhardtii.* Proceedings of the National Academy of Sciences, 2019. **116**(42): p. 21246-21255.
15. Watanabe, A., et al., *Amphipol‐assisted purification method for the highly active and*

stable photosystem II supercomplex of Chlamydomonas reinhardtii. FEBS letters, 2019. **593**(10): p. 1072-1079.

16. Pinnola, A. and R. Bassi, *Molecular mechanisms involved in plant photoprotection.* Biochemical Society Transactions, 2018. **46**(2): p. 467-482.
17. Goss, R. and B. Lepetit, *Biodiversity of NPQ.* Journal of plant physiology, 2015. **172**: p. 13-32.
18. Allen, J.F., *Protein phosphorylation in regulation of photosynthesis.* Biochimica et Biophysica Acta (BBA)-Bioenergetics, 1992. **1098**(3): p. 275-335.
19. Minagawa, J. and R. Tokutsu, *Dynamic regulation of photosynthesis in Chlamydomonas reinhardtii.* The Plant Journal, 2015. **82**(3): p. 413-428.
20. Minagawa, J., *State transitions—the molecular remodeling of photosynthetic supercomplexes that controls energy flow in the chloroplast.* Biochimica et Biophysica Acta (BBA)-Bioenergetics, 2011. **1807**(8): p. 897-905.
21. Wollman, F.-A. and C. Lemaire, *Studies on kinase-controlled state transitions in photosystem II and b6f mutants from Chlamydomonas reinhardtii which lack quinone-binding proteins.* Biochimica et Biophysica Acta (BBA)-Bioenergetics, 1988. **933**(1): p. 85-94.
22. Dumas, L., et al., *A stromal region of cytochrome b6f subunit IV is involved in the activation of the Stt7 kinase in Chlamydomonas.* Proceedings of the National Academy of Sciences, 2017. **114**(45): p. 12063-12068.
23. Rochaix, J.-D., *Role of thylakoid protein kinases in photosynthetic acclimation.* Febs Letters, 2007. **581**(15): p. 2768-2775.
24. Bressan, M., et al., *LHCII can substitute for LHCI as an antenna for photosystem I but with reduced light-harvesting capacity.* Nature Plants, 2016. **2**(9): p. 1-10.
25. Bonaventura, C. and J. Myers, *Fluorescence and oxygen evolution from Chlorella pyrenoidosa.* Biochimica et Biophysica Acta (BBA)-Bioenergetics, 1969. **189**(3): p. 366-383.
26. Murata, N., *Control of excitation transfer in photosynthesis I. Light-induced change of chlorophyll a fluoresence in Porphyridium cruentum.* Biochimica et Biophysica Acta (BBA)-Bioenergetics, 1969. **172**(2): p. 242-251.
27. Delepelaire, P. and F.-A. Wollman, *Correlations between fluorescence and phosphorylation changes in thylakoid membranes of Chlamydomonas reinhardtii in vivo: a kinetic analysis.* Biochimica et Biophysica Acta (BBA)-Bioenergetics, 1985. **809**(2): p. 277-283.
28. Takahashi, H., et al., *Identification of the mobile light-harvesting complex II polypeptides for state transitions in Chlamydomonas reinhardtii.* Proceedings of the National Academy

of Sciences, 2006. **103**(2): p. 477-482.

29. Tokutsu, R., M. Iwai, and J. Minagawa, *CP29, a monomeric light-harvesting complex II protein, is essential for state transitions in Chlamydomonas reinhardtii.* Journal of Biological Chemistry, 2009. **284**(12): p. 7777-7782.
30. Nagy, G., et al., *Chloroplast remodeling during state transitions in Chlamydomonas reinhardtii as revealed by noninvasive techniques in vivo.* Proceedings of the National Academy of Sciences, 2014. **111**(13): p. 5042-5047.
31. Wlodarczyk, L.M., et al., *Functional rearrangement of the light-harvesting antenna upon state transitions in a green alga.* Biophysical journal, 2015. **108**(2): p. 261-271.
32. Snellenburg, J.J., et al., *A model for the 77 K excited state dynamics in Chlamydomonas reinhardtii in state 1 and state 2.* Biochimica et Biophysica Acta (BBA)-Bioenergetics, 2017. **1858**(1): p. 64-72.
33. Ünlü, C., et al., *State transitions in Chlamydomonas reinhardtii strongly modulate the functional size of photosystem II but not of photosystem I.* Proceedings of the National Academy of Sciences, 2014. **111**(9): p. 3460-3465.
34. Iwai, M., et al., *Live-cell imaging of photosystem II antenna dissociation during state transitions.* Proceedings of the National Academy of Sciences, 2010. **107**(5): p. 2337-2342.
35. Nozue, S., et al., *Characterization of thylakoid membrane in a heterocystous cyanobacterium and green alga with dual-detector fluorescence lifetime imaging microscopy with a systematic change of incident laser power.* Biochimica et Biophysica Acta (BBA)-Bioenergetics, 2016. **1857**(1): p. 46-59.
36. Iermak, I., et al., *Visualizing heterogeneity of photosynthetic properties of plant leaves with two-photon fluorescence lifetime imaging microscopy.* Biochimica et Biophysica Acta (BBA)-Bioenergetics, 2016. **1857**(9): p. 1473-1478.
37. Lei, R., et al., *Chlorophyll fluorescence lifetime imaging provides new insight into the chlorosis induced by plant virus infection.* Plant cell reports, 2017. **36**(2): p. 327-341.
38. Nawrocki, W.J., et al., *State transitions redistribute rather than dissipate energy between the two photosystems in Chlamydomonas.* Nature plants, 2016. **2**(4): p. 1-7.
39. Huang, Z., et al., *Structure of photosystem I-LHCI-LHCII from the green alga Chlamydomonas reinhardtii in State 2.* Nature communications, 2021. **12**(1): p. 1-14.
40. Pan, X., et al., *Structural basis of LhcbM5-mediated state transitions in green algae.* bioRxiv, 2021.
41. Croce, R. and H. van Amerongen, *Light harvesting in oxygenic photosynthesis: Structural biology meets spectroscopy.* Science, 2020. **369**(6506).
42. Sheng, X., et al., *Plant and Algal PSII–LHCII Supercomplexes: Structure, Evolution and Energy Transfer.* Plant and Cell Physiology, 2021.

43. Wientjes, E., H. van Amerongen, and R. Croce, *Quantum yield of charge separation in photosystem II: functional effect of changes in the antenna size upon light acclimation.* The Journal of Physical Chemistry B, 2013. **117**(38): p. 11200-11208.
44. Wietrzynski, W., et al., *Charting the native architecture of thylakoid membranes with single-molecule precision.* bioRxiv, 2019: p. 759001.
45. Johnson, M.P., et al., *Nanodomains of Cytochrome b6f and Photosystem II Complexes in Spinach Grana.* Photosynth. Res. **29**: p. 45-54.
46. Papageorgiou, G.C. and R. Govindjee, *Chlorophyll a fluorescence: a signature of photosynthesis*. Vol. 19. 2004: Springer.
47. Mohamed, A., et al., *Structure-based modeling of fluorescence kinetics of photosystem II: relation between Its dimeric form and photoregulation.* The Journal of Physical Chemistry B, 2016. **120**(3): p. 365-376.
48. Shibata, Y., et al., *Red shift in the spectrum of a chlorophyll species is essential for the drought-induced dissipation of excess light energy in a poikilohydric moss, Bryum argenteum.* Photosynthesis research, 2018. **136**(2): p. 229-243.
49. Lamb, J.J., G. Røkke, and M.F. Hohmann-Marriott, *Chlorophyll fluorescence emission spectroscopy of oxygenic organisms at 77 K.* Photosynthetica, 2018. **56**(1): p. 105-124.
50. Fujita, Y., et al., *Imaging of intracellular rearrangement of photosynthetic proteins in Chlamydomonas cells upon state transition.* Journal of Photochemistry and Photobiology B: Biology, 2018. **185**: p. 111-116.
51. Van Spronsen, E., et al., *Three-dimensional structure of living chloroplasts as visualized by confocal scanning laser microscopy.* Protoplasma, 1989. **148**(1): p. 8-14.
52. Hasegawa, M., et al., *Selective excitation of photosystems in chloroplasts inside plant leaves observed by near-infrared laser-based fluorescence spectral microscopy.* Plant and cell physiology, 2010. **51**(2): p. 225-238.
53. Herbstová, M., et al., *Architectural switch in plant photosynthetic membranes induced by light stress.* Proceedings of the National Academy of Sciences, 2012. **109**(49): p. 20130-20135.
54. Kim, E., T.K. Ahn, and S. Kumazaki, *Changes in antenna sizes of photosystems during state transitions in granal and stroma-exposed thylakoid membrane of intact chloroplasts in Arabidopsis mesophyll protoplasts.* Plant and Cell Physiology, 2015. **56**(4): p. 759-768.
55. Schottkowski, M., et al., *Biogenic membranes of the chloroplast in Chlamydomonas reinhardtii.* Proceedings of the National Academy of Sciences, 2012. **109**(47): p. 19286-19291.
56. Mackinder, L.C.M., et al., *A Spatial Interactome Reveals the Protein Organization of the Algal CO2-Concentrating Mechanism.* Cell, 2017. **171**(1): p. 133-+.

57. Chmeliov, J., et al., *The nature of self-regulation in photosynthetic light-harvesting antenna.* Nature plants, 2016. **2**(5): p. 1-7.
58. Holzwarth, A.R., et al., *Identification of two quenching sites active in the regulation of photosynthetic light-harvesting studied by time-resolved fluorescence.* Chemical Physics Letters, 2009. **483**(4-6): p. 262-267.
59. Adams, P.G., et al., *Correlated fluorescence quenching and topographic mapping of Light-Harvesting Complex II within surface-assembled aggregates and lipid bilayers.* Biochimica et Biophysica Acta (BBA)-Bioenergetics, 2018. **1859**(10): p. 1075-1085.
60. Vallon, O., F. Wollman, and J. Olive, *Distribution of intrinsic and extrinsic subunits of the PS II protein complex between appressed and non‐appressed regions of the thylakoid membrane: an immunocytochemical study.* FEBS letters, 1985. **183**(2): p. 245-250.
61. Bertos, N.R. and S.P. Gibbs, *Evidence for a lack of photosystem segregation in Chlamydomonas reinhardtii (Chlorophyceae).* Journal of phycology, 1998. **34**(6): p. 1009-1016.
62. Engel, B.D., et al., *Native architecture of the Chlamydomonas chloroplast revealed by in situ cryo-electron tomography.* Elife, 2015. **4**: p. e04889.
63. Hell, S.W. and J. Wichmann, *Breaking the diffraction resolution limit by stimulated emission: stimulated-emission-depletion fluorescence microscopy.* Optics letters, 1994. **19**(11): p. 780-782.
64. Hell, S.W., *Far-field optical nanoscopy.* science, 2007. **316**(5828): p. 1153-1158.
65. Oracz, J., et al., *Photobleaching in STED nanoscopy and its dependence on the photon flux applied for reversible silencing of the fluorophore.* Scientific reports, 2017. **7**(1): p. 1-14.
66. Westphal, V. and S.W. Hell, *Nanoscale resolution in the focal plane of an optical microscope.* Physical review letters, 2005. **94**(14): p. 143903.
67. Otomo, K., et al., *Two-photon excitation STED microscopy by utilizing transmissive liquid crystal devices.* Optics express, 2014. **22**(23): p. 28215-28221.
68. Yang, B., et al., *Optical nanoscopy with excited state saturation at liquid helium temperatures.* Nature Photonics, 2015. **9**(10): p. 658-662.
69. Meredith, S.A., et al., *Model Lipid Membranes Assembled from Natural Plant Thylakoids into 2D Microarray Patterns as a Platform to Assess the Organization and Photophysics of Light‐Harvesting Proteins.* Small, 2021. **17**(14): p. 2006608.
70. Yoneda, T., et al., *Photosynthetic model membranes of natural plant thylakoid embedded in a patterned polymeric lipid bilayer.* Langmuir, 2020. **36**(21): p. 5863-5871.
71. Shibata, Y., et al., *Development of a novel cryogenic microscope with numerical aperture of 0.9 and its application to photosynthesis research.* Biochimica et Biophysica Acta

(BBA)-Bioenergetics, 2014. **1837**(6): p. 880-887.

72. Turkowyd, B., D. Virant, and U. Endesfelder, *From single molecules to life: microscopy at the nanoscale.* Analytical and bioanalytical chemistry, 2016. **408**(25): p. 6885-6911.
73. Gustafsson, M.G., *Surpassing the lateral resolution limit by a factor of two using structured illumination microscopy.* Journal of microscopy, 2000. **198**(2): p. 82-87.
74. Iwai, M., M.S. Roth, and K.K. Niyogi, *Subdiffraction - resolution live - cell imaging for visualizing thylakoid membranes.* The Plant Journal, 2018. **96**(1): p. 233-243.
75. Betzig, E., et al., *Imaging intracellular fluorescent proteins at nanometer resolution.* Science, 2006. **313**(5793): p. 1642-1645.
76. Weisenburger, S., et al., *Cryogenic optical localization provides 3D protein structure data with Angstrom resolution.* Nature methods, 2017. **14**(2): p. 141-144.
77. Rust, M.J., M. Bates, and X. Zhuang, *Sub-diffraction-limit imaging by stochastic optical reconstruction microscopy (STORM).* Nature methods, 2006. **3**(10): p. 793-796.
78. Ye, J.Y., et al., *Glass transition of associated solvents studied by fluorescence measurement of doped chromophores.* Physical Review B, 1996. **53**(13): p. 8349.
79. Yoshizawa, M., et al., *Femtosecond study of S2 fluorescence in malachite green in solutions.* Chemical physics letters, 1998. **290**(1-3): p. 43-48.
80. Wood, W.H., et al., *Dynamic thylakoid stacking is regulated by LHCII phosphorylation but not its interaction with PSI.* Plant physiology, 2019. **180**(4): p. 2152-2166.
81. Wood, W.H., et al., *Dynamic thylakoid stacking regulates the balance between linear and cyclic photosynthetic electron transfer.* Nature Plants, 2018. **4**(2): p. 116-127.
82. Amold, G., *CryoSTED microscopy - a new spectroscopic approach for improving the resolution of STED microscopy using low temperature.* 2007. PhD thesis. University of Heidelberg.
83. Huebinger, J., et al., *Ultrarapid cryo-arrest of living cells on a microscope enables multiscale imaging of out-of-equilibrium molecular patterns.* Science Advances, 2021. **7**(50): p. eabk0882.
84. Kellenberger, E., et al., *Artefacts and morphological changes during chemical fixation.* Journal of microscopy, 1992. **168**(2): p. 181-201.
85. Wang, L., et al., *Solid immersion microscopy images cells under cryogenic conditions with 12 nm resolution.* Communications biology, 2019. **2**(1): p. 1-11.
86. Ray, D.K., et al., *Yield trends are insufficient to double global crop production by 2050.* PloS one, 2013. **8**(6): p. e66428.
87. Foyer, C.H., A.V. Ruban, and P.J. Nixon, *Photosynthesis solutions to enhance productivity*. 2017, The Royal Society. p. 20160374.
88. Keyzer, M.A., et al., *Diet shifts towards meat and the effects on cereal use: can we feed*

the animals in 2030? Ecological Economics, 2005. **55**(2): p. 187-202.

89. Smil, V., *Nitrogen and food production: proteins for human diets.* AMBIO: A Journal of the Human Environment, 2002. **31**(2): p. 126-131.
90. Schmidhuber, J. and F.N. Tubiello, *Global food security under climate change.* Proceedings of the National Academy of Sciences, 2007. **104**(50): p. 19703-19708.
91. Kromdijk, J. and S.P. Long, *One crop breeding cycle from starvation? How engineering crop photosynthesis for rising CO2 and temperature could be one important route to alleviation.* Proceedings of the Royal Society B: Biological Sciences, 2016. **283**(1826): p. 20152578.
92. Ort, D.R., et al., *Redesigning photosynthesis to sustainably meet global food and bioenergy demand.* Proceedings of the national academy of sciences, 2015. **112**(28): p. 8529-8536.
93. Blankenship, R.E., et al., *Comparing photosynthetic and photovoltaic efficiencies and recognizing the potential for improvement.* science, 2011. **332**(6031): p. 805-809.
94. von Caemmerer, S., W.P. Quick, and R.T. Furbank, *The development of C4 rice: current progress and future challenges.* science, 2012. **336**(6089): p. 1671-1672.
95. Lin, H., et al., *A partial C4 photosynthetic biochemical pathway in rice.* Frontiers in plant science, 2020: p. 1581.
96. Kromdijk, J., et al., *Improving photosynthesis and crop productivity by accelerating recovery from photoprotection.* Science, 2016. **354**(6314): p. 857-861.
97. Ruban, A.V., *Nonphotochemical chlorophyll fluorescence quenching: mechanism and effectiveness in protecting plants from photodamage.* Plant physiology, 2016. **170**(4): p. 1903-1916.
98. Neupane, B., et al., *Insight into the electronic structure of the CP47 antenna protein complex of photosystem II: hole burning and fluorescence study.* Journal of the American Chemical Society, 2010. **132**(12): p. 4214-4229.
99. Andrizhiyevskaya, E.G., et al., *Origin of the F685 and F695 fluorescence in photosystem II.* Photosynthesis Research, 2005. **84**(1): p. 173-180.
100. Wientjes, E., et al., *The role of the individual Lhcas in photosystem I excitation energy trapping.* Biophysical Journal, 2011. **101**(3): p. 745-754.
101. Caffarri, S., et al., *Excitation energy transfer and trapping in higher plant photosystem II complexes with different antenna sizes.* Biophysical journal, 2011. **100**(9): p. 2094-2103.
102. Zhang, X.J., et al., *High-Speed Excitation-Spectral Microscopy Uncovers In Situ Rearrangement of Light-Harvesting Apparatus in Chlamydomonas during State Transitions at Submicron Precision.* Plant and Cell Physiology, 2021. **62**(5): p. 872-882.
103. Forester V. T. *Ein Beitrag zur Theorie der Photosynthese.* 1947. Z. Naturforschg. **2b**, 174-

182.

104. Santabarbara, S., et al., *Kinetics and heterogeneity of energy transfer from light harvesting complex II to photosystem I in the supercomplex isolated from Arabidopsis.* Physical Chemistry Chemical Physics, 2017. **19**(13): p. 9210-9222.

105. Jajoo, A., et al., *Low pH-induced regulation of excitation energy between the two photosystems.* Febs Letters, 2014. **588**(6): p. 970-974.

106. Groot, M.L., et al., *Initial electron donor and acceptor in isolated photosystem II reaction centers identified with femtosecond mid-IR spectroscopy.* Proceedings of the National Academy of Sciences, 2005. **102**(37): p. 13087-13092.

Acknowledgements

The guidance and cooperation of many people were indispensable in carrying out this research. I would like to express my gratitude to those who have helped me.

I would like to thank Assoc. Prof. Y. Shibata, Prof. S. Ye and Assis. Prof. K. Inoue in the laboratory for suitable guidance and fruitful discission. I apologize for the many inconveniences due to my insufficient motivation for research at some times. Even so, I am very grateful to them for taking care of me until I finish the doctoral course.

I would like to express my sincere gratitude to Prof. J. Minagawa and his co-workers in National Institute for Basic Biology and Prof. K Morigaki and Ms. Kusunoki in Kobe University for kindly gift their precious samples and guidance on the sample preparations.

I am very grateful to Mr. X. Zhang, Mr. R. Taniguchi and Mr. N. Kaneda for helping me with the sample culture and the measurements and providing precious opinions on my research.

I am very grateful to all students in the laboratory for providing precious feedbacks on my research and made the environment in the laboratory lively. Thanks to them, I was able to spend a very enjoyable time in the laboratory.

最後に、故郷を離れ大学での 9 年間を支えてくれた家族に心より感謝致します。